# Design and Experimental Evaluation of a Shape-Adaptive Track-Based Robotic Colonoscope

**Jiayang Du**

A thesis submitted in partial fulfilment of the requirements for the degree of
Doctor of Philosophy

The University of Sheffield
Faculty of Engineering
School of Electrical & Electronic Engineering

07/11/2025

# Abstract

Conventional colonoscopy remains the standard method for colorectal examination and intervention, but it is associated with patient discomfort, a risk of complications, and a strong dependence on operator skill. Although alternative techniques, such as CT-based virtual colonoscopy, have been developed, none has yet provided a comprehensive replacement. This thesis presents an experimentally validated track-based robotic colonoscope featuring an externally actuated, shape- and size-conforming expandable head. A review of current robotic colonoscopy technologies is first conducted to identify key challenges and opportunities for improvement. Based on this analysis, a robotic system with four independently controlled tracks was developed. The initial prototype employed soft bellows to actuate the expandable head, and benchtop experiments confirmed the feasibility and effectiveness of the design. Building on these findings, an optimized second-generation prototype was developed using an improved actuation mechanism. The new design achieved a propulsion speed of 14.5 mm/s, representing a 36.8% improvement over the first prototype (10.6 mm/s), while the maximum traction force increased from 3.0 N to 3.7 N. In addition, a force differential steering method was proposed and experimentally validated, demonstrating the robot's ability to actively navigate curved ducts. The results show that the proposed robotic colonoscope offers enhanced propulsion, traction, and steering capabilities, highlighting its potential to improve manoeuvrability and safety during navigation through the tortuous anatomy of the colon.

# Acknowledgements

People often begin to reflect when a journey is coming to an end.

Looking back on the past four years, I have had an unforgettable experience in Sheffield. This period not only shaped my academic growth and broadened my horizons, but also allowed me to meet many wonderful people who made this journey truly special.

First and foremost, I would like to express my sincere gratitude to Professor Sanja Dogramadzi and Dr. Lin Cao. Their invaluable guidance and support have helped me progress step by step along my academic path. Thank you, Sanja, for your generosity and encouragement. Every time you offered help and advance, it gave me the courage to try again and do better. “Do it first, then optimize” has become not only my motto in research but also a philosophy I apply to life. Thank you, Lin, for your insightful discussions and thoughtful suggestions that constantly inspired new ideas and deepened my understanding of academic inquiry.

I would also like to thank all the members of the Medical Robotics Laboratory. Your presence made my PhD life full of laughter and friendship. Special thanks to Bhoomika Gandhi, who is also about to graduate, thanks for your help in my PhD journey, as well as Zeyu Song, Baslin A James, and Michael A Evans for their kind help and companionship.

My gratitude also goes to all the staff at the Sheffield Robotics Laboratory for their generous technical and administrative assistance. I am especially grateful to Gerry Turner, now retired, for helping me during my experimental work, to Dominic Fella-Glanville for his valuable advice on robot optimization, and to Keria Sweet for continuous support throughout my PhD journey. I would like to express my sincere gratitude to everyone who has supported me throughout my doctoral journey. My heartfelt thanks go to all the staff members of the University of Sheffield.

Finally, I wish to express my heartfelt thanks to my parents for their unwavering support and encouragement, which gave me the strength to pursue my dreams far from home. I am deeply thankful to my girlfriend for being with me through countless anxious moments and for her thoughtful advice on my research. Last but not least, I want to thank my three cats, whose warmth and cuteness have healed every bit of my exhaustion and sadness.

Without the help and dedication of each and every one of you, this thesis would not have been possible.

# Declaration

*I, the author, confirm that the Thesis is my own work. I am aware of the University's Guidance on the Use of Unfair Means (https://www.sheffield.ac.uk/study-skills/assessment/academic-integrity/academic-integrity). This work has not previously been presented for an award at this, or any other, university.*

*Jiayang Du*

*05/11/2025*

# Contents

1 Introduction ..... 15
1.1 Background ..... 15
1.2 Research motivation and objectives ..... 16
1.3 Research contributions ..... 17
1.4 Thesis structure ..... 19
1.5 Research publications ..... 20
2 literature review ..... 21
2.1 Colon anatomy ..... 21
2.2 Current Approaches for Colonic Inspection and Their Limitations ..... 22
2.3 Robotic Colonoscopy: Opportunities and Challenges ..... 24
2.4 locomotion strategies ..... 25
2.4.1 Electromechanical locomotion ..... 26
2.4.2 Fluid-driven locomotion ..... 33
2.4.3 Smart material actuation ..... 41
2.4.4 Magnetic actuation (wireless) ..... 44
2.4.5 Everting (growing) locomotion ..... 46
2.5 Discussion and summary ..... 50
3 Development and characterization of the first Robotic colonoscope ..... 55
3.1 Design rationale and key design elements ..... 55
3.2 Overall design of the first prototype ..... 56
3.2.1 Design objectives and overall concept ..... 56
3.2.2 Design of the locomotion system ..... 57
3.2.3 Design of the bellow-based expansion mechanism. ..... 58
3.3 Fabrication and assembly ..... 59
3.3.1 Materials and fabrication methods ..... 60
3.3.2 Assembly procedure ..... 62

3.4 Control system ..... 65
3.5 Modelling ..... 66
3.6 Experiment tests and results ..... 69
3.6.1 Force and displacement measurements of bellows. ..... 70
3.6.2 Prototype testing ..... 72
3.6.3 Summary of experiment results ..... 77
3.7 Limitations and future improvements ..... 77
3.7.1 Limitations ..... 77
3.7.2 Future improvement ..... 78
3.8 Summary ..... 81
4 Design and evaluation of the prototype with hydraulic actuated expansion ..... 82
4.1 Introduction ..... 82
4.2 Overall design concept ..... 82
4.3 Structural and functional improvements ..... 85
4.3.1 Hydraulic expansion mechanism ..... 85
4.3.2 TPU-Based Tracks ..... 87
4.3.3 Structural reinforcement and transmission optimisation ..... 89
4.4 Mathematical modelling of the hydraulic expansion system ..... 91
4.4.1 Location of Syringe-actuator ..... 91
4.4.2 Displacement and force amplification in the hydraulic system ..... 93
4.4.3 Theoretical modelling of force transmission in hydraulic expansion ..... 94
4.5 Experimental evaluation and comparative analysis ..... 98
4.5.1 Characterisation of the hydraulic system ..... 98
4.5.2 Comparative tests of locomotion performance ..... 105
4.6 Discussion and summary ..... 108
5 Evaluation of force differential steering ..... 110
5.1 Introduction ..... 110

5.2 Principle of steering mechanism ..... 113
5.3 Mathematical modelling of steering ..... 114
5.3.1 Geometric Constraint Analysis ..... 114
5.3.2 Establish a curved pipe model ..... 115
5.3.3 Track's normal force and traction ..... 116
5.3.4 Steering analysis ..... 117
5.4 Experiment setup and results ..... 122
5.4.1 Experiment setup ..... 122
5.4.2 Force characterization experiments ..... 124
5.4.3 Steering experiments ..... 127
5.4.4 Dynamic response analysis based on IMU measurements ..... 132
5.5 Discussion ..... 133
5.6 Summary ..... 136
6 Discussion ..... 137
6.1 Discussion on expansion mechanisms: from pneumatic bellows to hydraulic syringes ..... 137
6.2 Structural optimization and stability enhancement ..... 138
6.3 Discussion on steering performance and force differential steering ..... 140
6.4 Hydraulic response and limitation ..... 141
6.5 Discussion on current open-loop control system ..... 142
6.6 Discussion on geometric and experimental constraints ..... 143
6.7 Chapter summary ..... 145
7 Conclusion and future work ..... 146
7.1 Conclusion ..... 146
7.2 Summary of contributions ..... 147
7.3 Future work ..... 148
Reference ..... 151

# List of Figure

Figure 2.1. Colon anatomy (structure of the Colon) [4]. .....22

Figure 2.2. Illustration showing common looping configurations of the insertion tube during colonoscopy, including: A sigmoid alpha loop, B reverse sigmoid alpha loop, C inverted sigmoid alpha loop, D inverted reverse sigmoid alpha loop, E sigmoid N-loop, and F spiral loop of the transverse colon [17]. .....23

Figure 2.3. Robotic Colonoscope with micro-patterned treads [29].....27

Figure 2.4. Tethered robotic capsule with micropillared treads and CMOS camera [28]. .....28

Figure 2.5. Track-based colon endoscopic robot [24]. .....28

Figure 2.6. The SoftSCREEN capsule robotic endoscope [23]. .....29

Figure 2.7. A. *RollerBall* robot system [31], B. The OdoCapsule equipped with miniature wheels [32].....30

Figure 2.8. Self-propelled paddles for robotic colonoscope system. A [33], B [35], C [36]...31

Figure 2.9. Pill-sized multi-legged robot [34]. .....32

Figure 2.10. A, the fibre-optic colonoscope [46], B, the *Aer-O-Scope* pneumatic colonoscope [44], C, the SPID (*Soft Pneumatic Inchworm Double-balloon*) colonoscope [43]. .....34

Figure 2.11. Double-Balloon robotic endoscope with independent control of expansion and bending [47].....35

Figure 2.12. Pneumatically driven colonoscopy robot with active steering and multi-chamber actuation [50]. .....35

Figure 2.13. (a) Bending mode of the first segment during one motion cycle; (b) Posture of the robot during one motion cycle in horizontal locomotion [51].....36

Figure 2.14. Schematic illustration of the peristaltic cyclic locomotion principle [62]. The robot consists of multiple serially connected units (Unit 1 - 3), each undergoing sequential expansion and contraction. Panels (a - e) represent the phases of one complete motion cycle, while (f)

indicates a single stroke. The anterior unit anchors through inflation, the posterior unit contracts to generate propulsion, and the phase shift between adjacent units enables continuous forward locomotion. ..... 38

Figure 2.15. Artificial rubber muscle appearance [53] [59]. ..... 39

Figure 2.16. Inchworm-inspired soft robotic colonoscope with rubber bellows and dual-balloon actuation [55]. ..... 39

Figure 2.17. Earthworm-inspired soft robotic system with hydraulically actuated segmented chambers [57]..... 40

Figure 2.18. The hydro-jet propelled colonoscope [65]. ..... 41

Figure 2.19. SMA-driven microrobot [68]. ..... 42

Figure 2.20. Earthworm-like locomotive mechanism for capsule endoscopes [77]..... 43

Figure 2.21. A, the *Active Locomotive Intestinal Capsule Endoscope (ALICE)* system [85], B, a micro-hydraulic capsule with actively biopsy [84], C, the magnetic-actuated robot composition [86]. ..... 45

Figure 2.22. Capsule endoscope with integrated permanent magnet [87]. ..... 46

Figure 2.23. Implementation and working principle of the soft growing robot [91]. ..... 48

Figure 2.24. Design and working principle of the FiloBot system. ..... 50

Figure 2.25. Basic in-pipe robotic locomotion types. [38] ..... 53

Figure 3.1. **(a)** A conceptual diagram of the robotic endoscope. The endoscope tip is driven using a worm couple **(B)** actuated by an external motor **(D)** through a flexible shaft. The tip also features four independently controlled expansion mechanisms enabled by a pneumatic bellow **(C)** and strut mechanisms **(E)**, **(b)** The expandable tip. The external motor is connected to a Arduino UNO to realize locomotion of the device (not equipped with camera lens). ..... 57

Figure 3.2. Schematic diagram of track-based locomotion. The motor rotation is transmitted through a worm gear to drive the track in the forward or backward direction, enabling linear motion along the colon wall. ..... 58

Figure 3.3. Schematic diagram of bellow. ..... 59

Figure 3.4. Different kind of flexible shaft. .....60

Figure 3.5. Fabrication of the soft-bodied bellows. .....61

Figure 3.6. Assembly process and prototype overview. A is the front view, B is the side view, and C is the side section. D is the physical diagram. ..... 错误!未定义书签。

Figure 3.7. Integration of the ball bearings with the worm-gear housing. The CAD model (left) illustrates the position of the ball bearings supporting the worm shaft at both ends. The photographs (bottom) show the corresponding fabricated components, while the right image presents the bearing dimensions (8 mm inner diameter, 22 mm outer diameter, and 7 mm thickness). .....63

Figure 3.8. Connection between the bellows and supporting arm. The CAD model shows the hinge joint between the bellows and the supporting arm, which converts the axial deformation of the bellows into radial motion of the track module. The inset image illustrates the corresponding fabricated component after assembly. .....64

Figure 3.9. Shaft coupler. .....65

Figure 3.10. Open loop control of four independent bellows using Arduino microcontroller. .....66

Figure 3.11. Diagram of the kinematic mechanism of the expansion tip. .....67

Figure 3.12. Force sensor experimental platform of the bellow with strut (insert shows the direction and position of the force measured in the experiment); b) Laser sensor platform for detecting the deformation of bellows. .....70

Figure 3.13. The relationship between the air volume inside the bellows and the internal pressure; b) $FA$, $FB$ and $FC$ as a function of pressure change in one bellow; c) Displacements of the bellow along width, height and length pressure in the bellow; d) Bellow rendering. ...71

Figure 3.14. Schematic diagram of working principle of expansion mechanism. Left - bellows are subjected to negative pressure; Middle - bellows are at atmospheric pressure, Right - bellows are subjected to positive pressure. .....72

Figure 3.15. Locomotion experiment of the prototype. The motor angular velocity was set to 75, 120, 150, 200 and 300 rpm to explore corresponding linear velocity of the prototype;

Different friction coefficients of the tube surface were emulated using foam, artificial tissue (made of silicone, with mucus) and smooth surface. ..... 73

Figure 3.16. (a) Propelling force experiment schematic diagram; (b) Comparison of different propelling forces as a function of motor speed measured on three different surfaces with varying friction coefficients and surface hardness. ..... 74

Fig. 3.17. Effect of pipe diameter on bellows pressure and propelling force in a prototype expansion mechanism. (a) Expansion mechanism in nominal state; (b) Conditioned maintenance of stable traction force. ..... 76

Figure 4.1. Block diagram of the control and actuation architecture of the robotic colonoscope. The system integrates a syringe-driven hydraulic expansion mechanism and an external motor transmission mechanism for track propulsion. Detailed views of each subsystem are presented in Figures X)–X ..... 83

Figure 4.2. Detail of robotic colonoscope head. ..... 84

Figure 4.3. Actual setup of syringe-driven hydraulic expansion system. ..... 85

Figure 4.4. Syringe-based hydraulic expansion module. ..... 86

Fig. 4.5. Comparison of track materials and cross-sectional tooth profiles between the first prototype (silicone, upper) and improved (TPU, lower) designs. The black and white TPU samples differ only in colour and are used to highlight the details. ..... 88

Figure 4.6. Quick-release mechanism for track replacement in the improved robotic colonoscope. (A) Quick-release interface of the track module, allowing rapid removal and replacement without disassembling the transmission system, (B) Quick-release mount of the hydraulic expansion mechanism, enabling convenient installation and adjustment of the syringe holder during experiments. ..... 89

Figure 4.7. Bearing-based sliding and support structures integrated in the improved prototype. ..... 90

Figure 4.8. The analysis diagram of syringe's location. ..... 92

Figure 4.9. Finite element analysis (FEA) of the TPU track deformation under different expansion states. (a) Initial state before expansion; (b) Moderate expansion under partial

hydraulic actuation; (c) Maximum expansion corresponding to the full stroke of the small syringe. ..... 99

Figure 4.10. Relationship between axial syringe displacement, radial expansion of the track, and generated radial force. ..... 100

Figure 4.11. Experimental setup and comparative results of hydraulic force amplification using different syringe combinations. ..... 101

Fig. 4.12. Theoretical relationship between syringe diameter ratio and output amplification of force and displacement. ..... 102

Fig. 4.13. Schematic diagram of small syringe response experiment. ..... 102

Figure 4.14. Relationship between hydraulic pipeline length and system response delay time. ..... 103

Figure 4.15. Comparison between experimental and theoretical displacement of the small syringe as a function of large syringe displacement. ..... 104

Figure 4.16. Effect of motor speed on propelling force: theory vs. two contact surfaces (smooth surface and bowel tissue). ..... 106

Figure 4.17. Comparison of Propulsion Speed: Current prototype vs. Prior prototype (with smooth surface and silicone -based colon skin) ..... 107

Figure 4.18. Comparison of the propelling force with previous and updated prototype in different tube size. ..... 108

Figure 5.1. Schematic of the system showing the InchIGRAB module integrated between the body and tail sections of the vine robot [101]. ..... 112

Figure 5.2. Geometric Model of the Robot in a Curved Section. ..... 114

Figure 5.3. Geometric representation of a curved tube. ..... 115

Figure 5.4. Geometric relationship of the robot navigating through a colon bend. ..... 118

Figure 5.5. Corrugated aluminium duct (D = 152mm). ..... 123

Figure 5.6. Coordinate definition and experimental setup of the robotic colonoscope. (A) The fixture designed for mounting the IMU sensor on the robot head. (B) The robot during locomotion inside the test duct, with the X, Y, and Z axes indicating the IMU coordinate directions (X: forward, Y: lateral, Z: vertical). ..... 124

Figure 5.7. Experimental configurations for traction measurement under different track retraction conditions. (A) Left track retracted, (B) Top track retracted, and (C) Right track retracted. ..... 125

Figure 5.8. Comparison of measured traction forces under different track configurations. .. 125

Figure 5.9. Measured and theoretical normal forces of a single track under different hydraulic inputs. ..... 126

Figure 5.10. Corrugated aluminium duct with 90° and 120° bending angles used for steering experiments. ..... 127

Figure 5.11. Comparison of yaw angle evolution between active and inactive steering during a 120° bend. ..... 128

Figure 5.12. Yaw angle under different wall friction conditions in a 90° bend. duct surface (medium friction, red), lubricated surface (low friction, blue), and artificial tissue (high friction, green). ..... 129

Figure 5.13. Configuration of the continuous S-shaped flexible duct used for steering experiments. ..... 130

Figure 5.14. Yaw angle evolution during navigation through a continuous S-shaped duct. . 131

Figure 5.15. Correlation between yaw angle and three-axis free acceleration during S-shaped bend navigation. ..... 132

Figure 6.1. Layered surface texture of the 3D-printed (FDM) part. ..... 140

# List of Table

Table 2-1 Average diameter of colon segments. .....21

Table 2-2 Comparison of colonic inspection methods. .....24

Table 2-3 Comparison of the principal actuation mechanisms used in robotic colonoscope and intraluminal robotic systems, summarizing their characteristic advantages, limitations, and representative studies. .....50

Table 2-4 Locomotion mechanisms for robotic colonoscope. .....51

Table 3-1 Geometric and transmission parameters of the prototype. .....69

Table 3-2 Comparison of the main limitations of the first-generation prototype and the corresponding improvement strategies .....80

Table 4-1 Definition of symbols related to the location of syringe. .....93

Table 4-2 Symbols and meanings related to force transmission in hydraulic expansion. .....97

Table 5-1 Definition of symbols related to force differential steering. .....120

# 1 Introduction

## 1.1 Background

The colon is an essential component of the human digestive system, and common diseases include inflammatory bowel disease, polyps, and colorectal cancer [1]. Among these, colorectal cancer ranks among the leading causes of cancer-related morbidity and mortality worldwide [1] [2]. Because its early symptoms are often subtle, such as changes in faecal colour, abdominal pain, or alterations in bowel habits, many patients fail to recognize the warning signs until the disease has progressed to an advanced stage [3] [4]. Studies have shown that early diagnosis is critical for improving the survival rate of colorectal cancer, and colonoscopy remains the most effective screening and diagnostic method currently available.

Although colonoscopy has become the "gold standard" for colorectal disease detection, the conventional procedure has several inherent limitations [5] [6]. The human colon is approximately 1.8 meters long, flexible, and tortuous, containing multiple sharp bends [7-10]. A traditional colonoscope is a long, semi-flexible endoscope in which only the distal tip is actively controllable, while propulsion relies primarily on external pushing by the operator. When the distal end encounters resistance, looping and buckling of the insertion tube may occur, increasing procedural difficulty and causing excessive traction on the intestinal wall [5]. These issues can result in patient discomfort, pain, or even early termination of the examination [6]. Consequently, the invasiveness and discomfort associated with the procedure remain major barriers to public acceptance of colonoscopy, especially among asymptomatic individuals.

Widespread colonoscopy detection has been shown to significantly reduce the incidence and mortality of colorectal cancer, alleviating the burden on healthcare systems and improving patient outcomes [10-14]. Therefore, improving the safety, efficiency, and tolerability of colonoscopy has become an important research focus [15] [16]. To achieve this goal, the concept of robotic colonoscopy has been proposed. Unlike conventional systems that rely on external pushing, robotic colonoscopes employ self-propelled or front-pulling mechanisms, allowing for autonomous advancement through the complex and flexible colon. These designs can reduce excessive force and looping, thereby improving procedural safety and patient comfort while enhancing detection compliance.

Over the past three decades, various research groups have developed multiple types of robotic colonoscopes, including magnetically actuated, inchworm-like, legged, track-based, and soft robotic systems, etc. [17]. These approaches aim to achieve stable propulsion, adaptability to

curvature and diameter variations, and safe contact pressure with the colonic wall. Although no fully commercialized system has yet been widely adopted, robotic colonoscopy continues to advance rapidly and demonstrates significant potential for future clinical application. The development of robotic colonoscopy not only represents a major step forward in medical endoscopy but also contributes to the broader evolution of intelligent medical robotics [10].

### 1.2 Research motivation and objectives

The limitations of conventional colonoscopy have motivated the development of robotic systems designed to improve safety, controllability, and patient comfort. Over the past decades, several robotic colonoscopes have been developed, incorporating magnetic actuation, inchworm-like peristaltic motion, legged structures, and track-based propulsion [17]. While these designs have shown potential in enhancing propulsion efficiency and reducing patient discomfort, they still face multiple challenges. Most systems lack adaptability to the varying geometry of the colon, which includes large changes in curvature and diameter. Many prototypes also suffer from limited traction or structural complexity, restricting their miniaturization and clinical feasibility.

To overcome these limitations, this research proposes a track-based robotic colonoscope that integrates a hydraulically driven expansion mechanism and a flexible rotating shaft, enabling the robot to adapt to varying intestinal diameters, maintain continuous traction on the colon walls, and achieve stable propulsion and steering control.

This research carries significance in both medical and engineering domains. From a medical perspective, colorectal cancer remains one of the leading causes of mortality worldwide, and early screening is essential for reducing death rates. Robotic colonoscopy has the potential to enhance patient tolerance, minimize risk, and improve examination efficiency. From an engineering standpoint, this study represents an intersection of mechanical design, miniaturized actuation, soft materials, and control systems in confined biological environments, offering broader implications for in vivo and in-pipe robotic applications.

The overall aim of this PhD project is to design, develop, and experimentally evaluate a robotic system capable of efficient locomotion within a colon. The main research objectives are as follows:

1. Review and analyse existing colonoscopy technologies and identify their clinical and technical limitations.

2. Evaluate prior robotic colonoscope designs and propose an improved structure addressing key challenges.
3. Complete the mechanical design and fabrication of a functional prototype.
4. Investigate and validate traction and expansion mechanisms through theoretical and experimental studies.
5. Develop an expansion system that enables adaptive diameter adjustment and active steering.
6. Characterize subsystem performance through modelling, analysis, and bench-top testing.
7. Build an electronic control platform integrating hardware and software components.
8. Validate the propulsion and steering performance of the prototype through structured experiments in a simulated colon model.

### 1.3 Research contributions

This thesis presents a track-based robotic colonoscope featuring an integrated hydraulic expansion mechanism, developed to address several key limitations in both conventional and existing robotic colonoscopy systems, including insufficient traction, limited adaptability to variations in lumen diameter, and restricted steering capability in tortuous environments. A further contribution of this work is the systematic integration of commonly used components, including flexible shaft transmission and track-based locomotion, into a unified framework that enables controllable force generation, adaptive wall interaction, and active steering in confined and compliant biological environments.

The main contributions of this research can be summarized as follows:

1. Force-differential steering via selective track disengagement.

A central contribution of this research is the introduction of a locomotion and steering strategy based on force differential generated through selective track disengagement. Unlike conventional approaches that rely on differential speed control or distal tip articulation, the proposed method achieves yaw motion by actively regulating the normal contact forces between individual tracks and the surrounding wall. By hydraulically reducing the normal force of selected tracks, a traction imbalance is created, producing a controllable steering torque while maintaining overall system stability. This approach enables the decoupling of propulsion

and steering functions and provides a new framework for navigation in low-friction and deformable environments.

2. A hydraulic expansion system for controllable radial force generation.

To enable this mechanism, a syringe-driven hydraulic expansion system is developed, allowing continuous and controllable adjustment of the radial contact force. In contrast to passive compliance or purely soft structures, the proposed system actively regulates the magnitude and distribution of contact forces, thereby enhancing traction performance and adaptability to varying diameters. The novelty of this contribution lies not merely in the use of hydraulic actuation, but in its integration as a unified mechanism that simultaneously supports anchoring, propulsion, and steering.

3. A hybrid actuation system that achieves independent liner motion, steering and radial size adaptation.

From a system-level perspective, this work combines motor-driven propulsion with hydraulically controlled contact modulation to realise multiple navigation functions within a unified framework. The proposed system achieves three primary functional degrees of freedom, namely axial locomotion, yaw steering, and radial expansion, through coordinated control of a motor-driven transmission and multiple hydraulic actuation channels. By explicitly establishing the relationship between actuator configuration and functional requirements, this approach enables the decoupling of propulsion, steering, and contact adaptation, allowing each function to be regulated independently while maintaining overall system coordination, without requiring separate mechanisms for these three locomotion modes. This framework provides a structured basis for understanding how hybrid actuation can be used to generate controlled motion in confined and compliant biological environments, and highlights the trade-offs between actuation complexity and functional capability.

4. A unified framework for quantitative performance evaluation of robotic colonoscope systems.

Finally, this research defines a set of measurable performance criteria for evaluating robotic colonoscope systems, including traction force, propulsion speed, steering capability, and stability of wall contact. By establishing these quantitative benchmarks, the work not only demonstrates the effectiveness of the proposed design but also provides a basis for comparison with future developments in the field.

It should be noted that the current prototype focuses primarily on the mechanical validation of locomotion, steering, and adaptive wall interaction. In a fully realized clinical system, additional functionalities, such as onboard imaging, sensing, and end-effector modules (e.g. biopsy tools), would be required. These functionalities would likely introduce additional actuation and control requirements, leading to a more complex system architecture.

In particular, future developments will involve the integration of miniature camera systems for real-time visual feedback, as well as image-based perception and recognition algorithms to assist robot navigation and motion control within complex intestinal environments. The present work therefore represents a foundational platform upon which further integration of sensing, control, and clinical functionalities can be developed. The envisioned final system would combine propulsion, steering, adaptive contact control, visual perception, and medical operation capabilities within a compact and fully integrated robotic platform.

### 1.4 Thesis structure

This thesis is organized into seven chapters, which together describe the conceptual development, design, fabrication, and evaluation of a track-based robotic colonoscope featuring a hydraulically expansion mechanism. The overall structure follows a logical sequence from research motivation and theoretical foundation to system design, experimental validation, discussion, and future perspectives.

Chapter 1 introduces the background, motivation, and objectives of the research. It highlights the clinical importance of early colorectal cancer screening, identifies the limitations of traditional colonoscopy, and presents the research aims and contributions. This chapter establishes the conceptual foundation and overall framework of the thesis.

Chapter 2 provides a comprehensive literature review of robotic colonoscopy and related robotic locomotion mechanisms. It begins with the anatomical and physiological characteristics of the colon and proceeds to analyse existing robotic designs, including magnetic, inchworm-like, legged, and track-based systems. The advantages and limitations of these approaches are compared to identify the technological gaps that motivate the proposed research.

Chapter 3 describes the design and development of the first robotic colonoscope. The chapter details the structural layout, locomotion mechanism, propulsion method, and testing platform used for validation. Experimental results and performance analyses are presented to identify

the key limitations of the initial prototype, including limited adaptability, insufficient propulsion, and control challenges.

Chapter 4 focuses on the improved second robotic colonoscope featuring a syringe-based hydraulic expansion mechanism and structure optimisation. This chapter presents the design rationale, fabrication methods, and validation experiments. The results demonstrate that the upgraded system achieves faster response, greater adaptability to varying diameters, and improved traction performance.

Chapter 5 investigates the active steering capability and motion behaviour of the robotic system in curved environments. It introduces the theoretical model of differential hydraulic actuation and describes the experimental procedures used to measure yaw response, acceleration changes. The results confirm that the hydraulic steering mechanism effectively enables controllable navigation through curved colon-like sections.

Chapter 6 presents an integrated discussion. It analyses the experimental results in depth, connecting theoretical predictions with observed behaviours to provide a comprehensive interpretation of the robot's performance. The chapter also summarizes the main findings and technological contributions of the research, emphasizing its significance in advancing adaptive robotic colonoscopy and its potential impact on clinical practice.

Chapter 7 outlines the conclusion and future work derived from this study. It discusses potential directions for improvement, including system miniaturization, integration of sensing and feedback for closed-loop control, optimization of hydraulic efficiency, and in vivo validation. The chapter also highlights how the presented design framework and experimental methodologies can be extended to other forms of in-pipe and medical robotic systems.

### 1.5 Research publications

The research presented in this thesis has been either accepted by peer-reviewed conferences and journals or is still in the process of review/revision, as detailed below:

**Journal articles**

- **Du, J.,** Cao, L., & Dogramadzi, S. (2025). Design and preliminary evaluation of a track-based robotic colonoscope with a shape-adaptable tip for propulsion. *Frontiers in Robotics and AI*, *12*, 1580692.

# 2 literature review

This chapter reviews the literature on robotic colonoscope, including the anatomy of the colon, the clinical motivations and existing diagnostic procedures, the potential of robotic approaches, and a range of locomotion strategies. Its purpose is to clarify the clinical and patient-centred requirements for effective intraluminal access, which include improved comfort and safety, reduction of pain and sedation, lower complication risks, higher completion rates, and timely diagnosis and therapy. The chapter further outlines the associated technical challenges and evaluates which locomotion methods are most appropriate for the colonic environment.

## 2.1 Colon anatomy

The human colon is an elastic, muscular tube that plays an important role in transporting and processing food residues during digestion [7]. It is composed of multiple concentric tissue layers, including the inner mucosa, muscular layer, and outer serosa, which collectively provide the strength and flexibility required for expansion and contraction under pressure [8]. Anatomical studies reveal that the human colon is a continuous hollow tube approximately 1.5 meters in length and 7.5 cm in diameter when inflated, although slight variations can occur due to individual factors such as age and sex [8] [9]. It is commonly divided into six segments: the rectum, sigmoid colon, descending colon, transverse colon, ascending colon, and cecum. The average diameters of these segments range from 26 to 45 mm, as detailed in Table I [9] [10].

Table 2-1 Average diameter of colon segments.

| Colon sections | Average Diameter (mm) |
|---|---|
| Rectum | 36 |
| Sigmoid colon | 26 |
| Descending colon | 33 |
| Transverse colon | 37 |
| Ascending colon | 45 |
| Cecum | 44 |

In addition to variations in diameter, the colon exhibits a tortuous geometry with multiple flexures. Among the colonic bends, the hepatic and splenic flexures are acute, whereas many

others have more moderate angles, together giving the colon a highly variable and complex geometry [9] [11]. The colon is sacculated, particularly evident when the lumen is insufflated, and is partially mobile as it is suspended by flexible mesocolons attached to the peritoneum. The wall thickness varies between 0.7 and 1.5 mm [11] and consists of distinct histological layers, including the mucosa, muscularis mucosae, submucosa, and muscle layers.

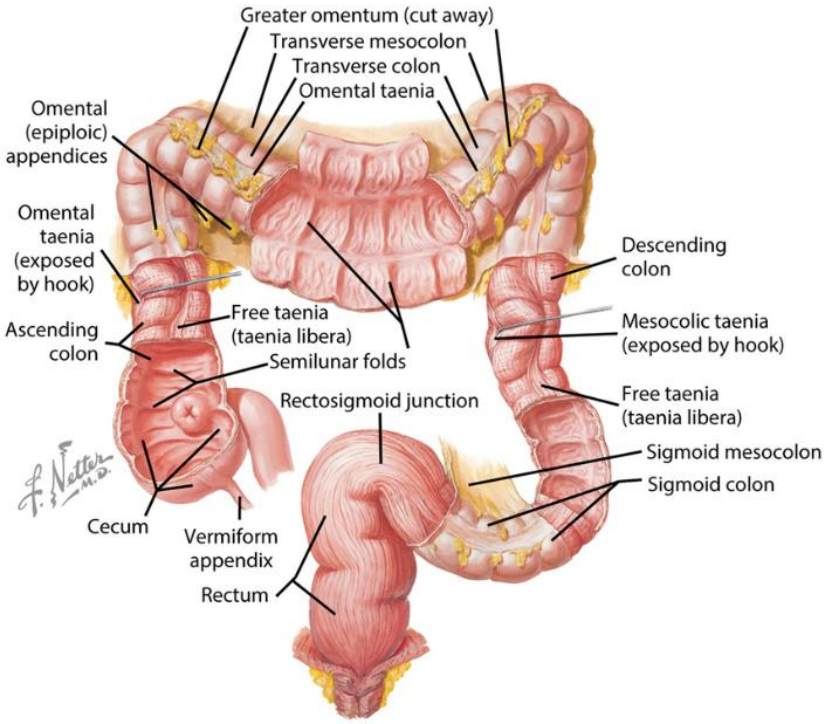


Figure 2.1. Colon anatomy (structure of the Colon) [4].

From a biomechanical perspective, the lubricated surface of the colon, covered with shear-thinning mucus, introduces complex frictional characteristics that are not yet fully understood. These properties are highly relevant to the design of robotic colonoscope employing contact-based locomotion, since they determine the required stroke length for propulsion, the methods of safely engaging with the tissue, and the control strategies needed under varying loads and speeds [12].

### 2.2 Current approaches for colonic inspection and their limitations

Over the past decades, significant changes in human lifestyle have been observed, including monotonous dietary patterns, reduced intake of dietary fibre, increased psychological stress, and sedentary work habits [13] [14]. These factors have contributed to a sharp rise in the incidence of colonic diseases. Such diseases include both inflammatory disorders and neoplastic conditions, with colorectal cancer imposing a substantial burden of morbidity and mortality worldwide.

Effective population-level management generally involves three essential stages: precise screening, timely diagnosis, and appropriate intervention.

Current strategies can be broadly divided into three levels. First, non-invasive screening methods such as faecal immunochemical testing (FIT), stool DNA testing, and quantitative occult blood testing are suitable for large-scale risk stratification but cannot provide therapy. Second, imaging approaches such as computed tomographic colonography offer comprehensive structural assessment but lack intraluminal therapeutic capability, and any suspicious findings still require confirmatory endoscopy. Third, flexible endoscopy remains the reference standard for diagnosis and treatment, as it enables biopsy, polypectomy, and haemostasis within a single inspection.

Colonoscopy, recognized as the "gold standard" for intestinal inspection and intervention, continues to be the mainstream clinical approach for managing colonic diseases. Nevertheless, factors such as the colon's length, tortuosity, and compliance, together with operator skill, influence both procedural success and patient experience [8] [15]. These challenges manifest as pain, the need for sedation, looping of the scope, incomplete examinations, and procedure-related complications [16].

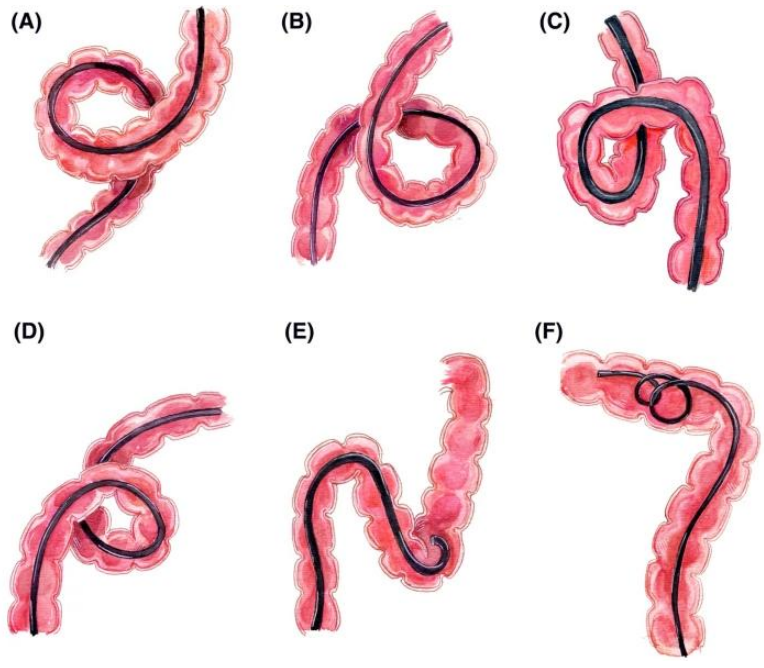


Figure 2.2. Illustration showing common looping configurations of the insertion tube during colonoscopy, including: A sigmoid alpha loop, B reverse sigmoid alpha loop, C inverted sigmoid alpha loop, D inverted reverse sigmoid alpha loop, E sigmoid N-loop, and F spiral loop of the transverse colon [17].

Table 2-2 Comparison of colonic inspection methods.

| Category | Methods | Advantages | Limitations |
|---|---|---|---|
| Non-invasive | Faecal immunochemical test (FIT), stool DNA test, faecal occult blood test | Simple, low cost, suitable for population-wide screening | No therapeutic function; limited sensitivity for early lesions; positives require colonoscopy |
| Minimally invasive (imaging) | Computed tomographic colonography (virtual colonoscopy) | Provides full-colon structural assessment; less invasive than endoscopy | No therapeutic capacity; radiation exposure; suspicious findings need colonoscopy |
| Invasive | Conventional colonoscopy (flexible endoscopy) | Gold standard for diagnosis and treatment; enables biopsy and therapy in one session | Painful, requires sedation, looping, secondary damage |

### 2.3 Robotic Colonoscopy: Opportunities and Challenges

Robotic colonoscopy has emerged as a promising alternative to overcome the limitations of conventional approaches [17] [18]. Unlike standard colonoscopes, robotic systems aim to achieve autonomous or semi-autonomous navigation within the tortuous colonic lumen while reducing operator dependence and patient discomfort. Potential advantages include improved completion rates, more stable visualization, reduced procedural pain and sedation requirements, and the integration of diagnostic and therapeutic capabilities into a single platform [19].

Nevertheless, the development of robotic colonoscopy faces substantial challenges. The colon presents a highly variable and compliant anatomy, with sharp flexures, diameter changes [8], and lubricated mucosal surfaces that complicate reliable propulsion and steering [17]. Safety remains a central concern, as any excessive force or uncontrolled motion may damage fragile tissue [20]. In addition, constraints on size, energy efficiency, and biocompatible materials

impose further design limitations. As such, robotic colonoscopy represents both an opportunity to transform clinical practice and a technical challenge that demands innovative solutions in locomotion, control, and patient safety.

Although incremental modifications to conventional colonoscopy have provided partial improvements, they do not fundamentally address the challenges posed by the colonic environment. This has motivated the development of robotic colonoscopy systems, which aim to achieve controlled navigation, reliable propulsion, and enhanced patient safety. A wide range of locomotion strategies have been proposed for such robots, and these can be broadly classified according to their actuation principles, including electromechanical, fluid-driven, smart material, and magnetic approaches, as well as hybrid systems that combine multiple mechanisms. The following section reviews these strategies in detail.

### 2.4 locomotion strategies

Locomotion is a fundamental consideration in the design of robotic colonoscopy systems. The ability to generate sufficient propulsion, maintain stable contact with the colonic wall, and achieve controlled steering is critical for safe and effective navigation [17] [18] [21]. Various strategies have been proposed in the literature to address these requirements, each based on different actuation principles and design concept [22]. In general, locomotion mechanisms can be classified into several categories, including electromechanical approaches that rely on wheels or tracks, fluid-driven systems based on pneumatic or hydraulic expansion, smart material actuators such as shape-memory alloys and ionic polymers, and magnetically actuated devices controlled by external fields. In addition, hybrid solutions that combine multiple mechanisms have been explored to leverage the advantages of different modalities [23]. The following sections review these strategies, highlighting their underlying principles, benefits, and inherent limitations.

To avoid ambiguity, this review adopts a two level taxonomy. Level 1 is the actuation source, namely how energy is generated and converted into actuation, for example electromechanical actuation using motors and transmissions, fluidic actuation using pneumatics or hydraulics, magnetic actuation where external fields apply forces or torques to internal magnets, and smart material actuation where materials deform in response to thermal, electrical, magnetic and other sources of energy . Level 2 is the locomotion architecture, namely the mechanical mode that transforms actuation into displacement and traction, for example wheeled, legged, tracked, wall press or double balloon, continuous multi chamber peristalsis, helical screw propulsion, water jet propulsion, and magnetic towing or steering. Each category at one level can be

associated with several categories at the other, forming an interlinked structure. A given locomotion mode can be realized by different actuation sources, for instance peristalsis can be implemented with pneumatic chambers, hydraulic bladders, or smart materials, and a given actuation source can drive different locomotion modes, for instance motor based systems can power wheels or tracks, or produce stepwise motion through leadscrews and linkages.

Following this framework, the review first organizes the literature by actuation source, then within each category it groups representative locomotion architectures and compares them, and finally a cross category summary table is provided. This organization exposes both the energy supply, transmission path, the kinematic and dynamic interaction with the colonic wall, which facilitates fair comparison.

### 2.4.1 Electromechanical locomotion

Electromechanical locomotion represents one of the most widely explored strategies for robotic colonoscopy. In these systems, propulsion is typically generated through the mechanical interaction of tracks [23- 30], wheels [31] [32], or alternative robot effector (such as: leg, paddle and fin, etc.) [33-39]driven by miniature motors and transmission elements. Such designs benefit from the maturity of electromechanical actuation, which allows precise control of speed, direction, and force output. Moreover, wheel and track-based solutions can provide consistent traction against the colonic wall, enabling forward advancement even in low-friction conditions.

Similar concepts have been extensively investigated in the field of in-pipe robots, where wheels, tracks, and wall-pressing mechanisms are employed to generate traction in confined tubular environments [38]. Such designs demonstrate the feasibility of electromechanical actuation for propulsion in narrow lumens. However, compared with industrial pipelines, the human colon presents additional challenges, including variable diameter, compliant walls, and the need to minimize mucosal trauma, which impose stricter requirements on system miniaturization and safety.

#### 2.4.1.1 Track-based

Track-based motion mode has been widely explored in robotic colonoscope. In track-based robotic colonoscope, propulsion is typically generated by miniature electric motors coupled with gears or worm drives that rotate rollers and drive the continuous track. This kind of system relies on a continuous track that keeps a large area of contact with the colon wall to achieve propulsion. Track can provide more stable traction under low friction and lubrication

environment, so it has certain advantages when passing through tortuous colon cavity [40]. At the same time, the increased contact area of the track helps to disperse the normal force, thus theoretically reducing the local pressure on the mucosa.

Several representative designs illustrate both the promise and challenges of this approach. Elastic and flexible caterpillar mechanisms demonstrated the ability to adapt to variations in lumen diameter. Lee et al. [25] reported an elastic caterpillar-based colonoscope capable of traversing tortuous paths while maintaining safety; their ex-vivo evaluations showed successful navigation without tissue damage such as bleeding or perforation, highlighting the importance of compliance. Similarly, Kim et al. [29] developed a flexible caterpillar actuated by an external motor through a flexible shaft. The system achieved stable propulsion in a colon-mimicking environment, though the reliance on external actuation limited portability.

Figure 2.3. Robotic Colonoscope with micro-patterned treads [29].

Capsule-type treaded robots represent another direction. Sliker et al. [30] evaluated a tethered robotic capsule with micro-patterned treads in a surgical setting, demonstrating sufficient traction to advance through the colon while maintaining visualization. However, their study also noted challenges with tether management and mucosal irritation. Building on this, Formosa et al. [28] applied optimization-based tread design and conducted surgical evaluations, showing improved locomotion efficiency and manoeuvrability compared to earlier tread geometries. These results confirm that tread morphology directly influences both propulsion performance and safety.

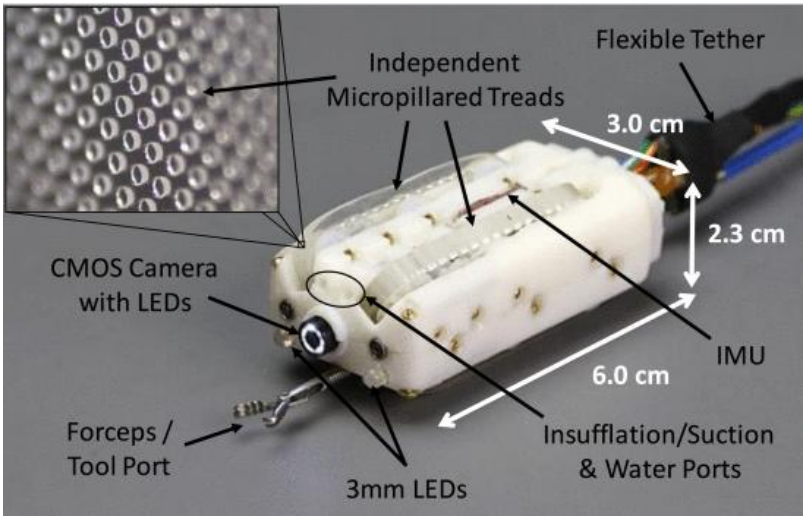


Figure 2.4. Tethered robotic capsule with micropillared treads and CMOS camera [28].

More recently, integration with perception has emerged as a new trend. He et al. [24] presented a track-based colon endoscopic robot equipped with stereo vision for haustral fold detection. This integration demonstrated that track-based systems can provide stable navigation platforms to support advanced perception tasks, potentially reducing missed lesions during navigation.

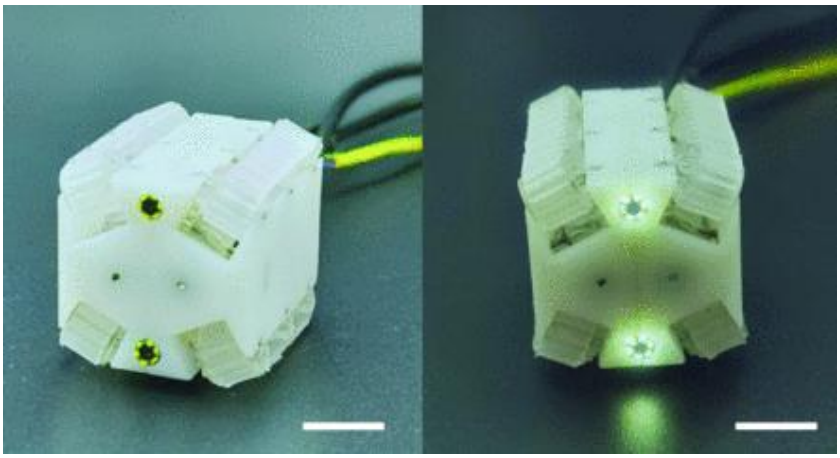

Figure 2.5. Track-based colon endoscopic robot [24].

Finally, soft robotic concepts have sought to improve adaptability and safety. The SoftSCREEN capsule robotic endoscope [23] introduced compliant track structures integrated into a capsule endoscope. The robot realizes the control of the robot diameter though two pneumatic balloons, thereby maintaining its central position within the colon as the lumen diameter changes. Bench-top experiments demonstrated effective locomotion in artificial colons, with the compliant tracks improving conformity and reducing localized wall stress. Complementary to this, Nagase and Fukunaga [26, 27] explored amoeba-inspired crawler mechanisms. Their cylindrical elastic and funicular crawlers demonstrated adaptability to

lumen variability, although their propulsion efficiency was relatively low compared with that of conventional treaded systems.

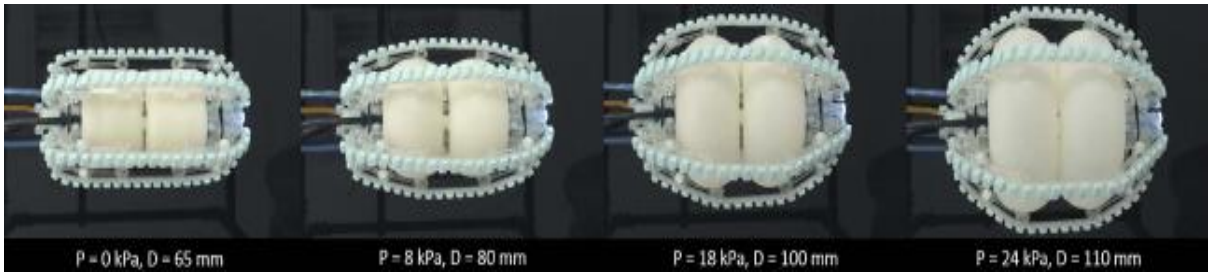


Figure 2.6. The SoftSCREEN capsule robotic endoscope [23].

In summary, track-based locomotion offers strong and consistent propulsion and has been validated across multiple prototypes in both bench-top and surgical evaluations. Experimental results confirm its capacity to traverse tortuous and lubricated environments, though limitations remain in terms of miniaturization [23] and system complexity [28]. Regarding tissue safety, previous biomechanical measurements reported that the tensile strength of human colonic tissue ranges from approximately 0.96 to 1.02 MPa across different regions of the colon [25]. In contrast, the contact pressure generated by the robot during wall interaction is substantially lower, indicating that the applied force remains within a physiologically safe range [29]. In recent studies, increasing attention has been directed toward enhancing traction forces, with wall-press contact mechanisms receiving growing interest among researchers [23]. Wahed and Arshad [41] introduced a wall-press type pipe inspection robot that actively regulates normal contact force to increase traction in smooth conduits. Similarly, Kim et al. [42] designed an in-pipe robot capable of adjusting its outer diameter to maintain stable contact across pipes of varying sizes. These approaches are considered promising for improving propulsion reliability in intraluminal environments, and they will be discussed in detail in the following sections. Besides, recent innovations in soft materials and perception-enabled designs suggest promising pathways to overcome these barriers, but further refinement is required before widespread clinical adoption.

#### 2.4.1.2 Wheel based

Wheel-based locomotion has been explored as one of the earliest electromechanical strategies for robotic colonoscopy. By employing independent rolling elements in contact with the lumen wall, these systems aim to achieve efficient propulsion with relatively simple mechanisms [17]. Compared with track-based robots, wheel-driven designs are mechanically less complex and can reduce frictional resistance, which makes them attractive for capsule-scale applications.

Norton et al. [31] proposed the *RollerBall* system, a tethered mobile robot designed for intraluminal locomotion. The device utilized spherical rolling elements to generate traction while minimizing shear forces on the mucosa. Its experiments demonstrated its ability to advance reliably in lubricated environments, highlighting the potential of wheel-driven concepts for reducing patient discomfort. However, the study also emphasized limitations in stability and steering, as discrete wheels provided less conformity to the lumen compared with continuous tracks.

In parallel, Karargyris and Koulaouzidis [32] introduced the OdoCapsule, a wireless capsule endoscope equipped with miniature wheels integrated with odometry sensors. This system not only improved locomotion control but also enabled accurate lesion localization and video stabilization, addressing two major challenges of conventional capsule endoscopy. Compared with other wheel-based designs, the OdoCapsule offers more precise motion tracking and position estimation due to its embedded odometry; however, its wheel-driven mechanism may still suffer from limited traction in mucus-covered regions, restricting its effectiveness in highly slippery environments. Preliminary evaluations confirmed enhanced navigation and diagnostic capability, though the integration of active wheels increased device complexity and power requirements, which remain critical barriers for untethered operation.

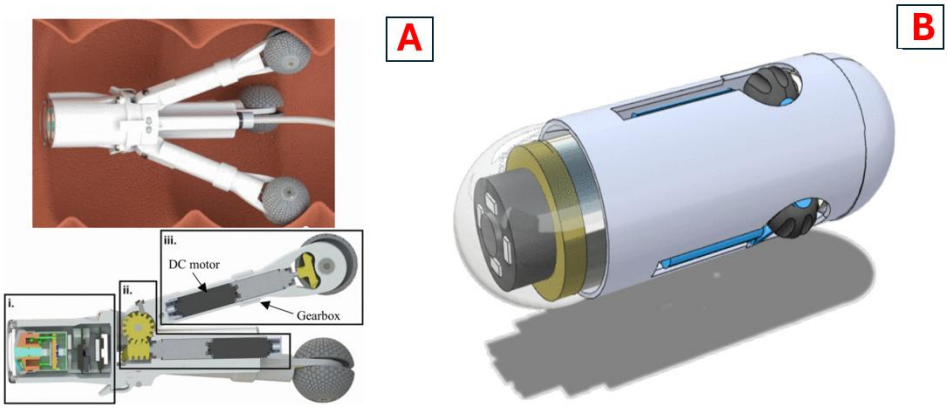


Figure 2.7. A. *RollerBall* robot system [31], B. The OdoCapsule equipped with miniature wheels [32].

Overall, wheel-based robots provide a mechanically efficient and scalable solution, particularly for capsule-type devices. Yet their limited adaptability to lumen diameter changes and reduced locomotion and contact stability in tortuous colonic segments restrict their standalone applicability, as slippage and loss of wall contact frequently occur during motion.

2.4.1.3 Alternative robot effectors

Legged and paddling mechanisms represent alternative electromechanical strategies that seek to improve traction and lumen adaptability without relying on continuous tracks. Paddling designs use flexible or rigid blades that periodically interact with the mucosal surface or intraluminal fluid to generate thrust, whereas legged capsules deploy multiple retractable legs that alternately grip and release the wall to advance.

Recent prototypes have integrated self-propelled paddles with feeding and steering subsystems to create endoscopes capable of forward progression and directional control in settings [33]. Flexible paddle arrays can conform to the colonic wall and generate propulsion under low normal loads, thereby minimizing localized mechanical stress on the mucosal surface and reducing the risk of tissue irritation caused by shear forces [35]. Earlier designs demonstrated the feasibility of paddling at capsule scale and clarified key parameters such as paddle stiffness, stroke amplitude, and beat frequency for efficient propulsion in lubricated environments [36]. Helical fin variants extend the paddling concept by providing continuous contact along a spiral geometry, which assists in centring and stabilizing the device within the lumen [37]. Reported evaluations indicate reliable advancement in artificial or ex vivo models and improved stability in tortuous segments, although net thrust remains modest compared with treaded systems. Energy efficiency and long-duration durability of compliant paddles also remain open challenges.

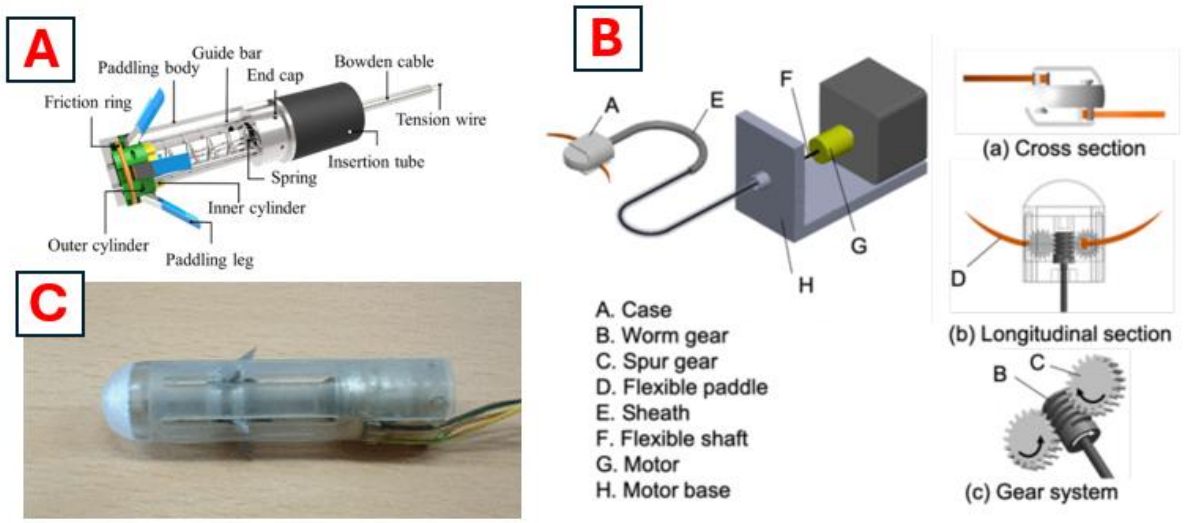


Figure 2.8. Self-propelled paddles for robotic colonoscope system. A [33], B [35], C [36].

Capsules employ multiple deployable legs to achieve wall anchoring and inchworm-like progression [39]. This approach provides controllable traction and intrinsic adaptability to

diameter changes because leg extension can be modulated to regulate normal force. Pill-sized legged robots with 12 legs could generating 0.66 N of force at each leg tip at the same time [34], as shown in Figure 2.9. In practice, leg coordination and contact timing are critical for smooth motion; improper synchronization can induce slip or excessive wall loading. While legged designs can deliver high peak traction and precise stepwise motion, they introduce mechanical complexity, raise miniaturization demands for reliable actuation and sensing, and require careful control to avoid mucosal indentation.

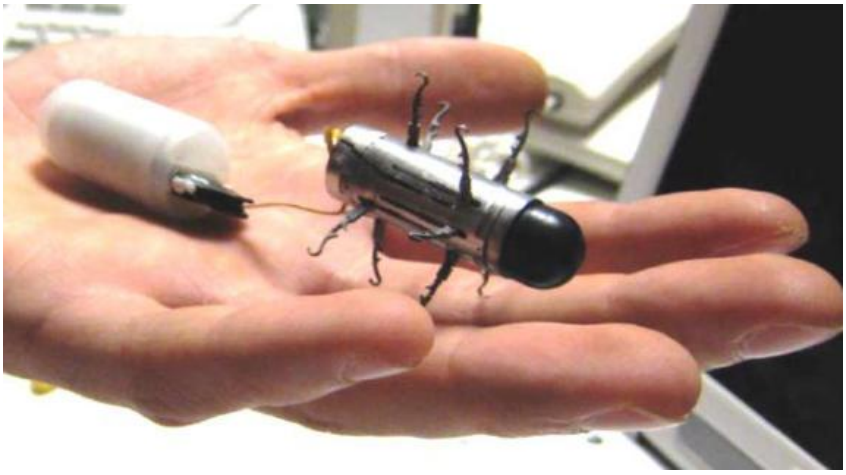

Figure 2.9. Pill-sized multi-legged robot [34].

Work on miniature in-pipe robots provides useful guidance for both paddling and legged concepts, including strategies for force regulation, modular actuation, and compact transmissions that operate in confined tubular environments [38]. Across studies, legged and paddling systems demonstrate feasibility for intraluminal propulsion. Nevertheless, common limitations persist. Typical issues include modest average speed, sensitivity of thrust to lubrication conditions, elevated control complexity, and uncertain long-term safety under repeated surface interactions. These observations motivate hybrid architectures that couple leg or paddle elements with auxiliary feeding, magnetic guidance, or fluidic assistance to balance traction, safety, and energy efficiency.

#### 2.4.1.4 summary

In summary, electromechanical locomotion has provided some of the most mature and widely tested strategies for robotic colonoscopy, ranging from wheel-based and track-based systems to less common legged and paddling designs. These mechanisms offer reliable traction, controllable motion, and straightforward integration with existing actuation technologies. Nevertheless, their adaptation to the colonic environment is constrained by issues of miniaturization, structural rigidity, and potential mucosal irritation arising from continuous

wall contact or high normal forces. Although electromechanical approaches remain attractive for their precision and robustness, further advances are required to balance propulsion efficiency with safety and compliance.

These limitations have motivated the exploration of alternative or hybrid solutions, such as fluid-driven and magnetic actuation, which will be discussed in the following sections.

### 2.4.2 Fluid-driven locomotion

Fluid-driven locomotion represents an alternative strategy that takes advantage of pneumatic or hydraulic actuation to achieve propulsion in confined luminal environments. Unlike electromechanical systems, which rely on continuous mechanical contact through wheels or tracks, fluid-driven mechanisms generate motion by inflating, contracting, or oscillating compliant structures. This approach offers several inherent advantages: the use of soft, expandable elements allows adaptation to variable lumen diameters, while the distributed contact reduces the risk of localized mucosal trauma. Moreover, fluidic actuation can achieve peristaltic or wall-press motion patterns that more closely mimic biological locomotion, potentially improving propulsion efficiency in tortuous pathways.

#### 2.4.2.1 Wall-press locomotion

The anchoring mechanism of wall-press is an important development direction in the research of robotic colonoscope based on fluid drive. Its fundamental principle is to contact, anchor and advance the colon wall through the filling and discharging of gas or liquid within chambers, so as to complete the self-driven movement along the cavity [43- 51]. This type of drive is usually pneumatic, which can provide compliant contact characteristics and better safety, and avoid the damage to the mucosal trauma caused by the mechanically driven designs.

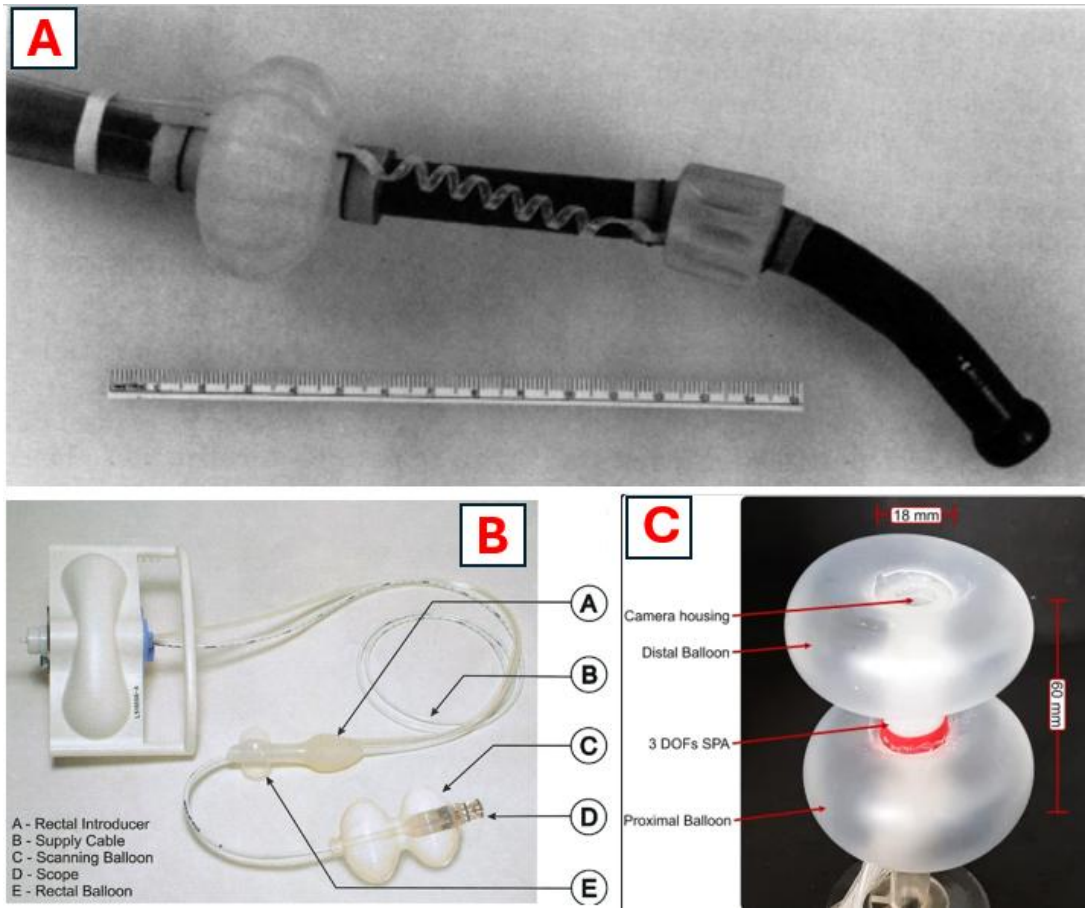


Figure 2.10. A, the fibre-optic colonoscope [46], B, the *Aer-O-Scope* pneumatic colonoscope [44], C, the SPID (*Soft Pneumatic Inchworm Double-balloon*) colonoscope [43].

The earliest exploration dates back to the 1980s, when Sugarbaker et al. [46] proposed a pneumatically driven fibre-optic colonoscope capable of automated advancement using periodic air pulses-representing the first attempt to employ pneumatic force for colonoscope propulsion. Later, Vucelic et al. [44] introduced the *Aer-O-Scope*, a skill-independent, self-propelling, and self-navigating pneumatic colonoscope that demonstrated the feasibility of automatic endoscope insertion through closed-loop airflow and balloon expansion. Clinical validation confirmed its safety and controllability, establishing a foundation for subsequent fluidic designs.

In the 2010s, researchers shifted toward biomimetic and soft-structured robots to improve adaptability and patient safety. Manfredi et al. [43] developed the SPID (*Soft Pneumatic Inchworm Double-balloon*) colonoscope, employing two alternately inflated balloons to anchor and advance within a transparent colon phantom. The balloon exhibits a dimensional variation from 0 to 30 mm and provides a maximum longitudinal force of 4.8 N. The same group later proposed a compact pneumatic control unit [49]. The author continues to improve the stability

of the components, and realizes the higher precision control of the most robots through Bluetooth and Simulink, the enhancing system integration and portability.

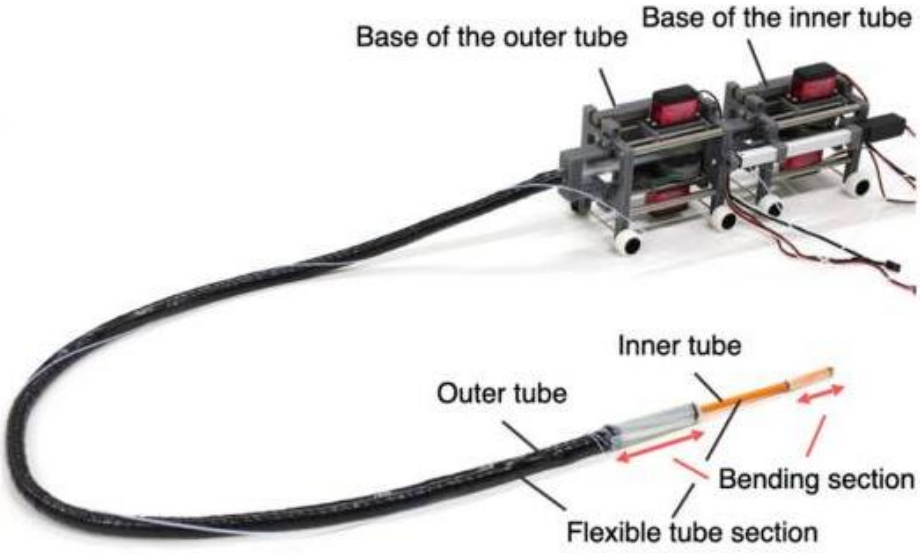


Figure 2.11. Double-Balloon robotic endoscope with independent control of expansion and bending [47].

Dehghani et al. [50] developed a pneumatically driven colonoscopy robot with active steering capability, employing a multi-chamber distributed actuation scheme that allows coordinated bending and propulsion. The system advanced 1.5 m through an ex vivo curved porcine colon at an average speed of 28 mm/s and was able to navigate bends of up to 150°.

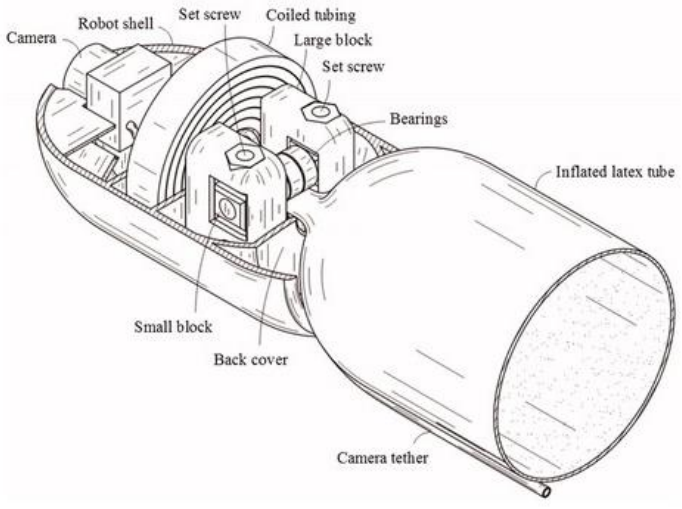


Figure 2.12. Pneumatically driven colonoscopy robot with active steering and multi-chamber actuation [50].

Takamatsu et al. [47] proposed a similar structure as [43]: a double-balloon, double-bend robotic endoscope that independently controls the expansion of front and rear balloons and the

bending posture of the tube, enabling precise steering and stable advancement, as shown in Figure 2.11. Huan et al. [45] introduced a soft-tethered, over-the-tube pneumatic propulsion system that integrates multiple balloon actuators within a flexible sheath, designed for clinical compatibility with conventional colonoscopes. The system achieved a propulsion speed of 1.9-2.2 mm/s in a colon simulator, demonstrating its ability to navigate complex bends while reducing the manual insertion load on clinicians. However, the dependence on external pneumatic supply and the relatively bulky sheath limited its autonomy and miniaturization potential, indicating the need for more compact, self-contained actuation solutions for future designs.

By independently adjusting the pressure in each chamber, the multi-chamber configuration enables distributed actuation and fine force control [51], allowing adaptive deformation [49] and wall-contact modulation during propulsion [43] [45] [52]. This architecture substantially enhances the robot's compliance, controllability, and safety within complex and tortuous luminal environments, while providing a structural foundation for multi-modal locomotion such as peristaltic and differential steering [51].

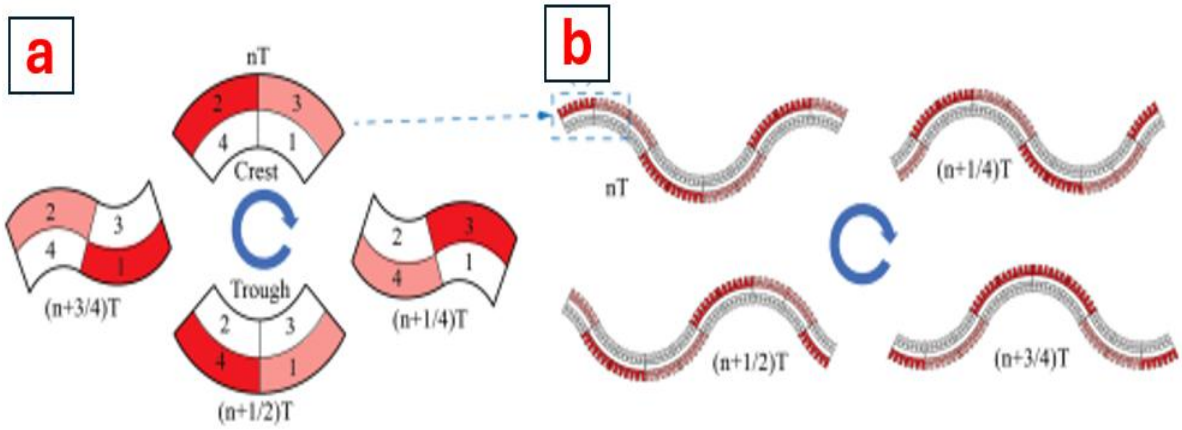


Figure 2.13. (a) Bending mode of the first segment during one motion cycle; (b) Posture of the robot during one motion cycle in horizontal locomotion [51].

Nguyen et al. [51] proposed a soft robotic architecture employing a series of pneumatic actuators combined with distributed balloon modules. The design enables both axial and radial deformation through independently controlled chambers, and a comprehensive modelling and control framework was established to describe its pneumatic dynamics. The authors analysed the pressure-displacement behaviour, force response, and system dynamics, demonstrating that the robot achieved continuous and controllable motion within a pressure range of 0-200 kPa, with an average propulsion speed of 17.94 mm/s and the ability to perform a 90° turn in a colon

simulator. While this work presents an important step toward fully controllable soft endoluminal robots, its reliance on multiple pneumatic control channels and an external air supply increases system complexity and hinders real-time clinical deployment. These challenges highlight the need for more integrated and compact actuation strategies in future developments.

Glozman et al. [48] presented an inflatable, earthworm-like endoscope actuated by a single air-supply line, achieving continuous peristaltic locomotion through sequential chamber inflation. A propulsion mechanism composed of two or serially connected pneumatic chambers can achieve forward motion of the colonoscope through repeated inflation–deflation cycles. This design concept, based on sequential chamber expansion and contraction, is commonly adopted in bio-inspired robots that mimic the peristaltic motion of inchworms or earthworms, representing a typical example of periodic fluid-driven locomotion. The following subsection will provide a more detailed discussion and systematic summary of this class of cyclic actuation mechanisms

#### 2.4.2.2 Periodic locomotion

Periodic or peristaltic locomotion represents a biologically inspired propulsion strategy derived from the natural peristalsis, such as : earthworms and inchworm, where alternating expansion and contraction of body segments or chambers generate anchoring and forward motion cycles [53-62]. This mechanism provides high compliance and environmental adaptability, making it suitable for intraluminal and pipeline robotic applications.

Liu, et al. [54] presented a comprehensive review on actuation and design innovations in earthworm-inspired soft robots, summarizing the structural evolution and control methodologies of peristaltic propulsion mechanisms in recent soft robotic research. The review classified existing systems by actuation type, material selection, segment architecture, friction control, and system integration, highlighting the transition from single-chamber rigid actuators to multi-chamber, distributed, and fully soft-bodied designs.

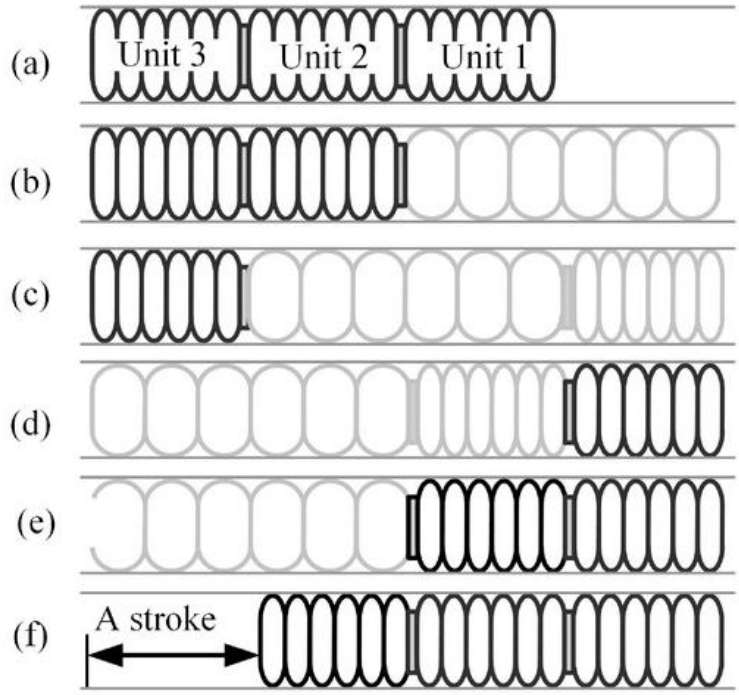


Figure 2.14. Schematic illustration of the peristaltic cyclic locomotion principle [62].

As illustrated in Figure 2.14, the robot consists of multiple serially connected units (Unit 1 - 3) that achieve periodic locomotion through sequential expansion and contraction, forming a propagating peristaltic wave. Panels (a - e) represent the phases of one complete motion cycle, while (f) indicates a single stroke. During operation, the anterior unit inflates and anchors to the wall via friction, while the posterior unit contracts to generate forward thrust; subsequently, the anterior unit releases as the next segment anchors. The phase shift between adjacent units enables continuous forward locomotion.

Early developments focused on replicating peristaltic motion using pneumatic artificial muscles and bellows-based structures. Kim et al. [56] first proposed the Smart Colonoscope system, employing pneumatic artificial muscles to produce extension-contraction cycles for segmental advancement inside the colon. Saga [58] subsequently introduced a prototype peristaltic robot actuated by pneumatic artificial muscles under a single air-supply line, demonstrating the feasibility of sequential multi-segment actuation. Then, the researchers tried to realize periodic movement by connecting more artificial muscles, so as to improve the robot's sports ability. Nakamura and Yanagida et al. [53] [59] extended this concept by integrating bellows-type rubber muscles along the axis of a colonoscope, achieving peristaltic motion through cyclic pressurization and deflation, as shown in Figure 2.15.

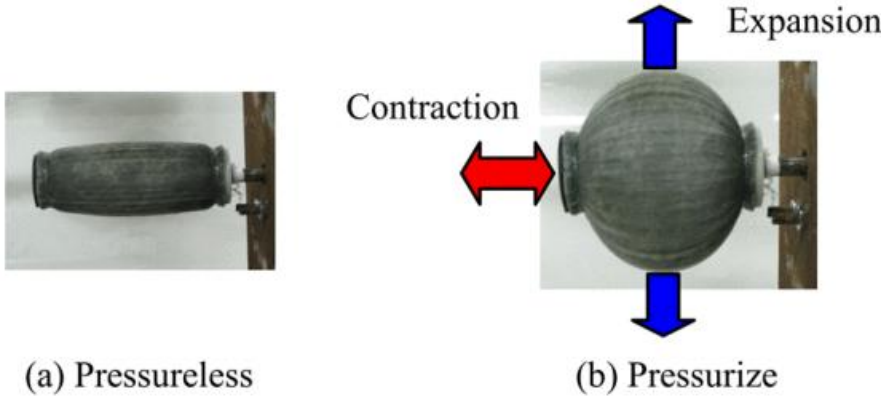


Figure 2.15. Artificial rubber muscle appearance [53] [59].

With advances in soft robotics, more compliant multi-chamber and distributed pneumatic systems emerged. Chen et al. [55] developed an inchworm-inspired soft robotic colonoscope using rubber bellows, where alternating inflation of front and rear chambers generated an anchor-propel cycle, verified through controlled propulsion experiments in colon phantoms. The robot can achieve a compression ratio of 0.5, and has a flexible head that can rotate 180 degrees. Wang et al. [62] presented a fully actuated soft colonoscope that combined pneumatic chambers and flexible sheaths, enabling continuous peristaltic advancement while reducing wall stress.

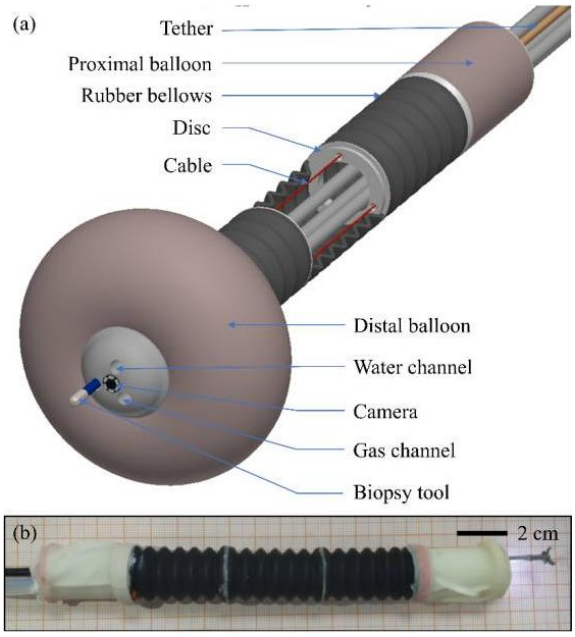


Figure 2.16. Inchworm-inspired soft robotic colonoscope with rubber bellows and dual-balloon actuation [55].

Li et al. [57] designed an earthworm-inspired soft robot for intestinal sampling, featuring hydraulically actuated segmented chambers that achieved smooth elongation and directional

motion within a pressure range of 1.2-2.7 kPa. There are two independent cavities as axial and radial actuators, respectively, as shown in Figure 2.17. This device is tested in an environment containing simulated human intestinal mucus, and can reach a running speed of 9 cm/min (1.5 mm/s ) in a flexible pipeline.

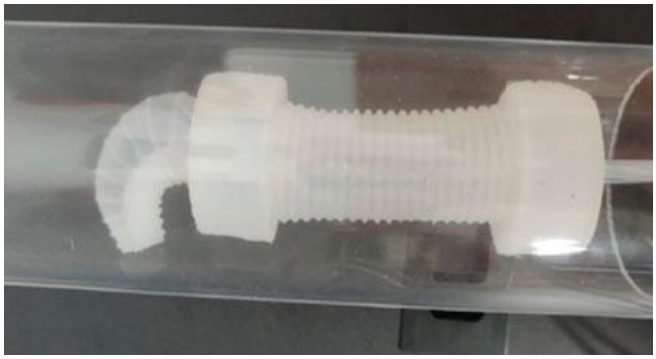

Figure 2.17. Earthworm-inspired soft robotic system with hydraulically actuated segmented chambers [57].

Das et al. [61] developed a modular earthworm-like soft robot capable of motion across various terrains by generating overlapped peristaltic waves between adjacent segments, achieving 9.19 N of maximum radial force in 50-ml module. Liu et al. [60] proposed a multimodal continuous soft robot employing a pneumatic-cable hybrid winding transmission mechanism that allows switching between motion modes, significantly improving propulsion efficiency.

In summary, peristaltic locomotion has evolved from early rigid pneumatic prototypes to highly compliant multi-chamber soft systems, driving the advancement of robotic colonoscope toward greater flexibility, adaptability, and controllable propulsion. By controlling chamber pressurization sequences and phase differentials, these systems achieve continuous wave-like motion and high-angle bend navigation. Nevertheless, challenges remain in actuation synchronization, response delay, and miniaturization.

#### 2.4.2.3 Water-jet

Water-jet (or hydro-jet) propulsion is a non-contact actuation method that generates thrust through high-pressure fluid ejection, reducing wall friction and minimizing tissue stress [63].

Coleman et al. (2016) developed a fully hydraulically driven colonoscope prototype [64]. The system utilized controlled liquid pressurization within chambers to generate forward propulsion and steering motion. In a subsequent study, Coleman et al. introduced a hydro-jet propelled colonoscope based on water-jet ejection [65]. By employing multiple controllable nozzles, the system generated jet-induced thrust to autonomously advance within a water-filled

colon phantom. Experiments showed successful insertion of colon configurations with force from 11-27 N while maintaining wall forces and fluid temperatures within safe limits. This work validated the feasibility of jet-based propulsion for colonoscope navigation but noted its operational limitations in air-filled or semi-dry lumens.

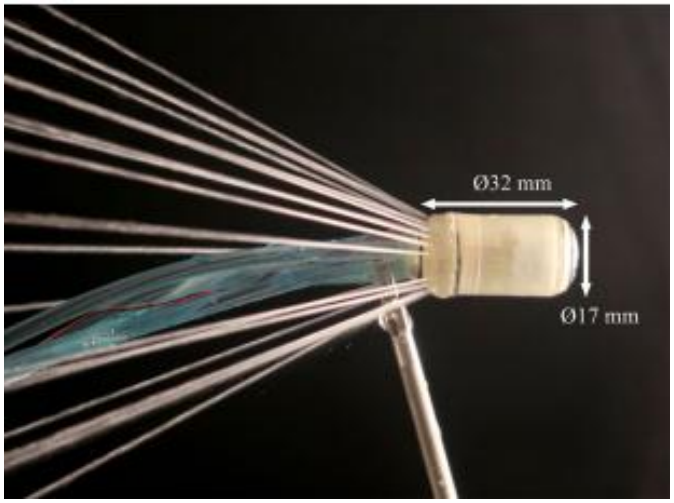


Figure 2.18. The hydro-jet propelled colonoscope [65].

Overall, water-jet propulsion offers advantages of simplicity, speed, and non-contact motion, but its dependence on liquid media, complex pressure regulation. It is also widely used in pipeline robots, where continuous liquid presence enables efficient jet-based thrust generation and navigation through narrow or curved conduits. But, due to limited integration potential currently restrict its broader application, making it more suitable as an auxiliary propulsion strategy in fluid environments.

### 2.4.3 Smart material actuation

Although smart material actuators have achieved remarkable progress in soft robotics, their use in colonoscopy systems is still largely exploratory. For brevity, this section provides only a concise overview of related studies to ensure completeness of the actuation taxonomy.

Smart material actuation has emerged as a rapidly developing field in soft and biomedical robotics. Unlike conventional electromechanical or fluidic systems, these actuators exploit the intrinsic responsiveness of materials to external stimuli such as heat, electricity, magnetic fields, or light, to induce reversible deformation or stiffness modulation, thereby reducing mechanical complexity and enhancing compliance [66] [67].

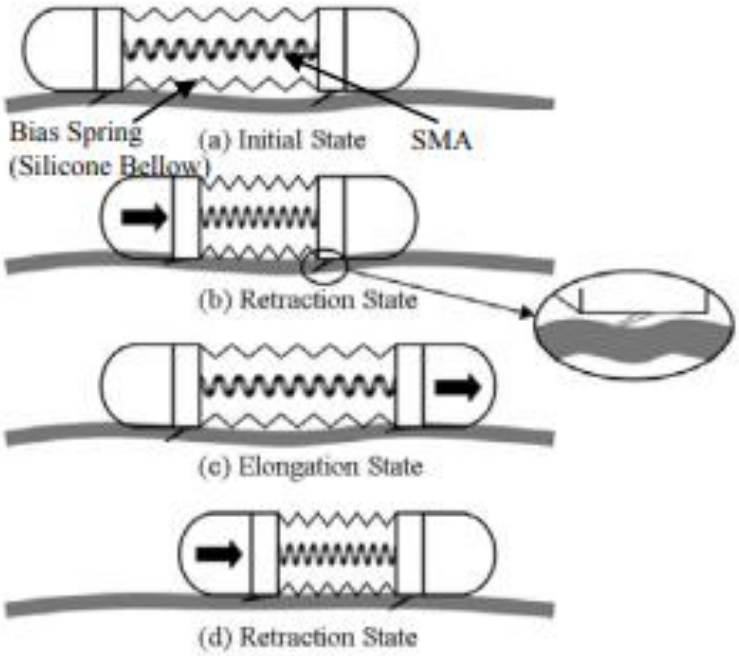


Figure 2.19. SMA-driven microrobot [68].

Representative smart materials include Shape Memory Alloys (SMA) [68-71], Shape Memory Polymers (SMP) [72-74], Dielectric Elastomers (DE) [75] [76], piezo-actuated [77], etc. These materials can be activated thermally, electrically, or pneumatically to achieve contraction, bending, or stiffness tuning.

Among them, Kim et al. [68] developed a microrobot for capsule endoscopy employing an SMA-driven telescopic actuator that achieved axial propulsion and directional control, offering a novel concept for active capsule locomotion, as shown in Figure 2.19. This model can pass through the small intestine with a maximum inclination angle of 78 degrees and obtain a speed of 3.29-6.26 mm/s.

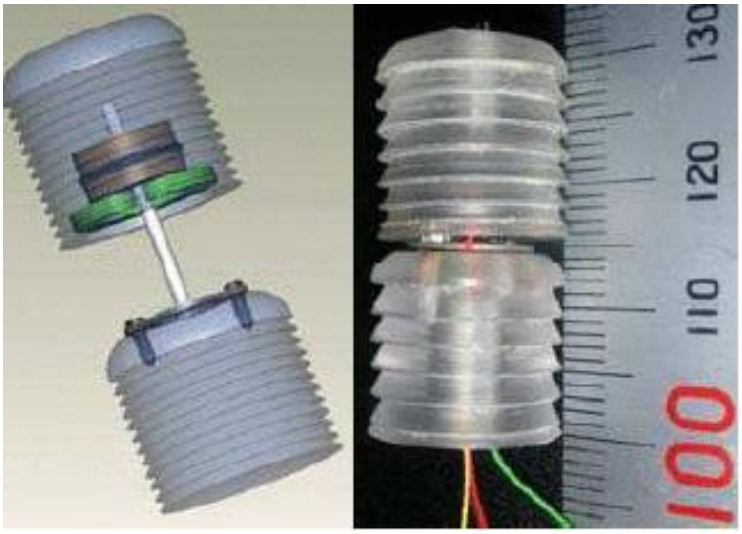


Figure 2.20. Earthworm-like locomotive mechanism for capsule endoscopes [77].

It is noteworthy that although the actuation principles differ among electromechanical, pneumatic, hydraulic, and smart material based systems, their locomotion patterns are fundamentally similar. Most robots still employ an earthworm or inchworm inspired periodic motion, in which alternating anchoring and propulsion phases generate net displacement. The difference mainly in the actuation mechanism, where motor driven units are replaced by pneumatic chambers, hydraulic bladders, or shape memory alloy segments. In essence, these systems share the same bio inspired kinematic concept, while differing in the mode of energy transmission and structural implementation.

Kim et al. proposed an earthworm-like locomotive mechanism for capsule endoscopes with almost 11 mm stroke, as shown in Figure 2.20 [77]. The system achieves forward motion through sequential inflation and deflation of front and rear chambers, generating periodic anchoring and propulsion similar to the peristaltic motion of an earthworm. The robot consists of multiple modular segments, each incorporating paired inflatable balloons connected by elastic elements to reproduce axial elongation and contraction. Experimental results demonstrated unsuccessful propulsion inside a dead porcine small intestine, achieving an average speed of 2.23 mm/s.

Overall, smart material-based actuation offers advantages of compactness, silent operation, and adaptive compliance, but remains limited by dependence on external stimuli, modest output forces, and complex control requirements. These mechanisms are therefore more suitable as auxiliary or hybrid actuation strategies, yet they represent a promising pathway toward fully soft and safe robotic colonoscope.

### 2.4.4 Magnetic actuation (wireless)

Magnetic actuation has been widely explored in capsule and intraluminal robotic systems as a non-contact propulsion and control method [79-81]. By applying external magnetic fields to embedded permanent magnets or magnetically responsive materials, magnetic actuation enables remote manipulation without internal power transmission. Owing to its wireless operation, intrinsic safety, and excellent biocompatibility, magnetic actuation has been extensively investigated for capsule endoscopy, intraluminal robots, and other medical microrobots [81] [82]. Compared with electromechanical or fluidic actuation, magnetic systems eliminate mechanical transmission or tethers and achieve motion through magnetic torque and field-gradient forces, offering advantages in compactness and miniaturization.

According to the mode of magnetic interaction, magnetic actuation can be classified into three main types [83]:

- permanent magnetic coupling,
- magnetic field gradient propulsion,
- hybrid magnetic control .

The first approach typically uses an external rotating magnet to generate torque for helical propulsion or orientation control, while the second relies on field gradients to induce translational motion. Hybrid systems combine both effects, allowing simultaneous control of position, propulsion, and steering.

In the field of magnetically actuated colonoscope and capsule robotic systems, several studies have demonstrated the feasibility of remote manipulation and precise navigation [84-87].

Leon-Rodriguez et al. [84] presented a conceptual design of a micro-hydraulic capsule for active biopsy, in which hydraulic actuation was used for biopsy tool deployment and retraction, and the mechanism was compatible with magnetic navigation. Wang et al. [86] developed a wireless robotic endoscope that integrated internal permanent magnets with external electromagnetic fields for attitude and position control, validating the potential of magnetic propulsion within gastrointestinal environments. This robot can achieve only 40 mm movement in the intestine, and the power consumption can reach 0.4 W, and the calculated driving force is about 0.87 N. Subsequently, Lee et al. [85] introduced the *Active Locomotive Intestinal Capsule Endoscope (ALICE)* system, which combined magnetic coupling with segmented

actuation to enable forward, backward, and directional motion under external magnetic guidance. In ex vivo and in vivo tests, the capsule achieved an average propulsion speed of 3 mm/s in a 30-40 mm lumen. At the same time, when the maximum input current is 10A, the maximum propulsion force is about 0.7 N.

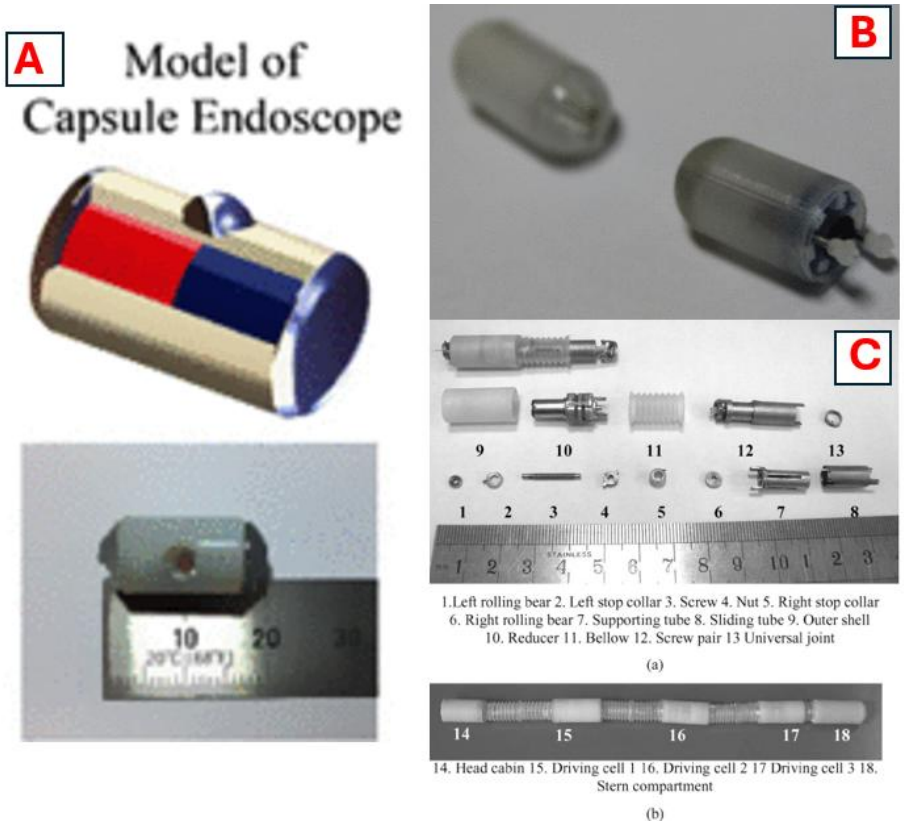


Figure 2.21. A, the *Active Locomotive Intestinal Capsule Endoscope (ALICE)* system [85], B, a micro-hydraulic capsule with actively biopsy [84], C, the magnetic-actuated robot composition [86].

Building on these concepts, Verra et al. [87] proposed a magnetically actuated soft-tethered colonoscopy platform, where an external magnetic field controlled the orientation and position of a tethered capsule, see in Figure 2.22. The capsule is connected to the external platform via a flexible tether and is equipped with an internal camera, lighting, and sensing modules for real-time imaging and navigation feedback. A dedicated localization system tracks the capsule's position and orientation, enabling closed-loop magnetic field control. The graphical user interface displays both the endoscopic view and system parameters, while pedal and touchscreen inputs allow the operator to adjust movement modes and propulsion commands. The entire setup is mounted on a movable platform for flexible laboratory or clinical deployment.

The experimental results show that under the condition of meeting the requirements of conventional colonoscopy, the interaction force can be smaller (1.17 N vs 4.12 N), which has great clinical potential.

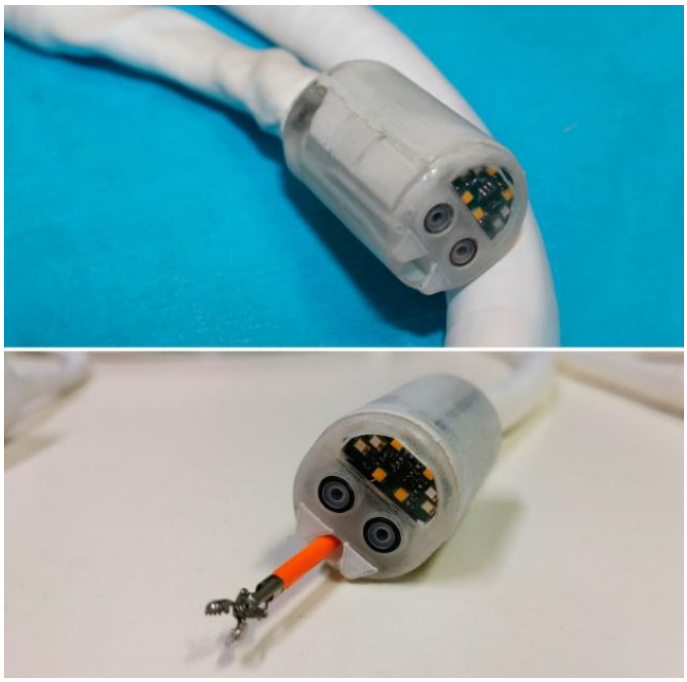

Figure 2.22. Capsule endoscope with integrated permanent magnet [87].

In summary, magnetic actuation offers a non-contact control strategy for robotic colonoscope, enabling remote navigation and orientation adjustment while maintaining high compliance and minimally invasive characteristics. By precisely modulating external magnetic fields, such systems can steer and propel capsules or flexible endoscopes within complex luminal environments, improving both procedural safety and patient comfort.

Nevertheless, the propulsion capability of magnetic systems remains constrained by field strength decay with distance, and the external magnetic setup is often bulky and requires complex feedback control. As a result, magnetic actuation is currently better suited for navigation and orientation assistance rather than primary propulsion.

### 2.4.5 Everting (growing) locomotion

In recent years, a new class of robotic systems has emerged based on the everting or “growing” locomotion principle [88]. Unlike conventional wheel, track, or pneumatically driven mechanisms that rely on frictional traction against the intestinal wall, everting robots advance by continuously turning a flexible membrane inside out from the distal tip, effectively extending the body forward within the lumen.

Although most of these systems are pneumatically actuated, their locomotion principle fundamentally differs from traditional pneumatic propulsion, which typically depends on cyclic pressurization to generate friction-based traction. The everting mechanism, by contrast, produces forward motion through the inversion of a thin membrane, leading to uniform pressure distribution and inherently smooth, self-anchoring progression. This unique actuation geometry greatly reduces shear forces and localized wall stress, making everting or growing endoscopes an attractive direction for minimally invasive and tissue-safe endoscope navigation. Consequently, everting locomotion has been recognized as a distinct research category and is discussed separately in this review.

The robot advances by extending from its distal tip rather than pushing its entire body forward [89-94]. At present, two main actuation strategies have been explored: one relies on pressure-driven eversion of stored material, while the other achieves growth through additive material deposition at the tip [88].

Hawkes et al. [91] demonstrated a novel robot capable of continuous body extension from the distal tip, thereby minimising sliding friction against the environment and distributing contact pressure uniformly along the surface, as shown in Figure 2.23. This work established the fundamental principle of low-friction motion in confined spaces. The prototype, with an initial length of 28 cm, could extend up to approximately 72 m through pressure-driven eversion, with the maximum length limited by the amount of plastic film stored on the reel. This remarkable extension ratio highlights the potential of everting locomotion for long-distance deployment in constrained environments. However, the trajectory remained largely linear, and the motion relied on open-loop control guided by environmental constraints rather than active steering, revealing a trade-off between structural simplicity and directional controllability in purely pneumatic designs.

Figure 2.23(A) illustrates the pressure-driven tip eversion mechanism, where an internal pump inflates the robot body, causing the stored tubular membrane to unfold and evert from the distal tip. The flexible membrane, wound on a reel at the base, passes through the centre of the body during operation, with the reel rotation regulating the robot length. Figure 2.23(B) shows sequential images of the elongation process for a robot with an external diameter of approximately 2.5 cm.

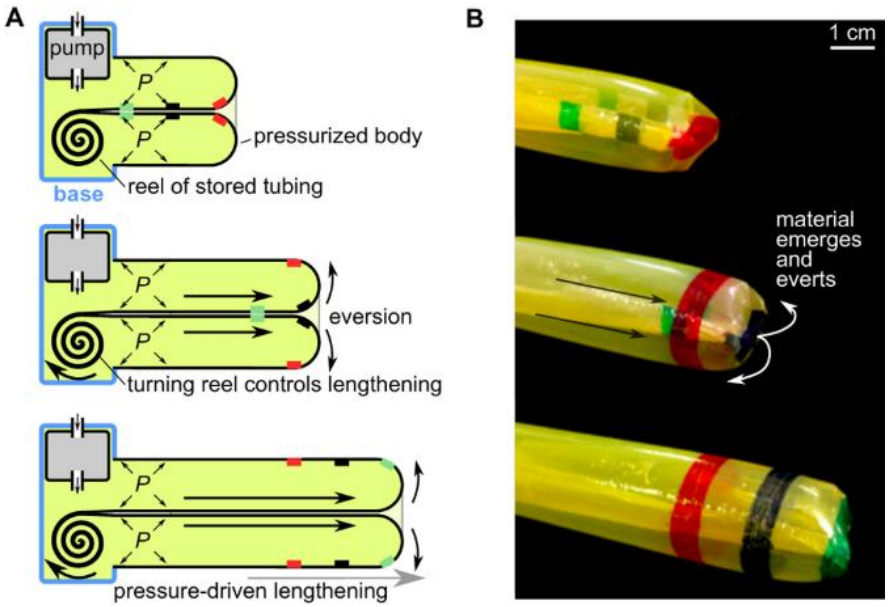


Figure 2.23. Implementation and working principle of the soft growing robot [91].

Greer et al. [89] subsequently introduced obstacle-aided navigation for soft growing robots, demonstrating that controlled interaction with surrounding boundaries could be exploited for passive steering. Their experiments provided important insight into how environmental constraints may assist locomotion, but the approach also revealed a key weakness: the robot's ability to follow pre-defined trajectories was highly dependent on external geometry, making autonomous navigation unreliable in unstructured environments.

Wu and Mintchev [90] proposed a vine-like robot capable of simultaneous bending and elongation through differential pressure control in multiple pneumatic chambers. This multi-tube architecture enhanced manoeuvrability but also introduced notable mechanical limitations. Compared with conventional vine robots equipped with terminal actuators, their design was more sensitive to reel friction, which restricted motion in high-curvature environments. The frictional force between the inflated tail and the outer sheath was approximately 1 N per meter of body length. However, during curved motion, the so-called reel effect, dependent on tail tension, further increased internal friction and the risk of jamming. External radial compression also aggravated this issue by forcing the tail against the sheath surface. Despite these drawbacks, the robot exhibited partial retractability, being able to retract up to around 2 m, demonstrating improved reversibility compared with earlier everting prototypes.

Within the medical domain, Dinkel et al. [93] presented one of the first applications explicitly targeting colonoscopy. Their pressure-modulated expanding robot achieved forward

propulsion in a colon simulator under controlled loading conditions, verifying that eversion-based locomotion can reduce wall stress compared with conventional insertion. However, the prototype remained bulky and dependent on an external pneumatic unit, underscoring the need for more compact, self-contained actuation systems. Collectively, these studies confirm the promise of tip-growing and everting mechanisms for safe, low-pressure locomotion in complex luminal environments, while also revealing persistent barriers related to control accuracy, integration, and miniaturization. These insights motivate further research toward hybrid or hydraulically assisted designs that retain the compliance of everting robots while enhancing force controllability and clinical practicality.

Del Dottore et al. [94] developed a bioinspired soft robot that grows by depositing material at its tip, rather than unfolding stored material through pneumatic eversion. The design draws inspiration from climbing plants, where new structural material is continuously formed at the growing tip to enable adaptation and anchoring. Functionally, this mechanism resembles an additive manufacturing process similar to fused deposition modelling, in which soft polymer material is extruded and solidified to form the extending body. This approach eliminates the need for internal pressure chambers, offering precise shape control and structural stability during growth. However, the additive process is relatively slow and energy intensive, making it unsuitable for fast or long-distance navigation inside the human body. In addition, the need for continuous material supply and local solidification complicates miniaturization and hinders integration with medical sterilization protocols. While conceptually innovative, this growth-by-deposition strategy remains far from clinical implementation.

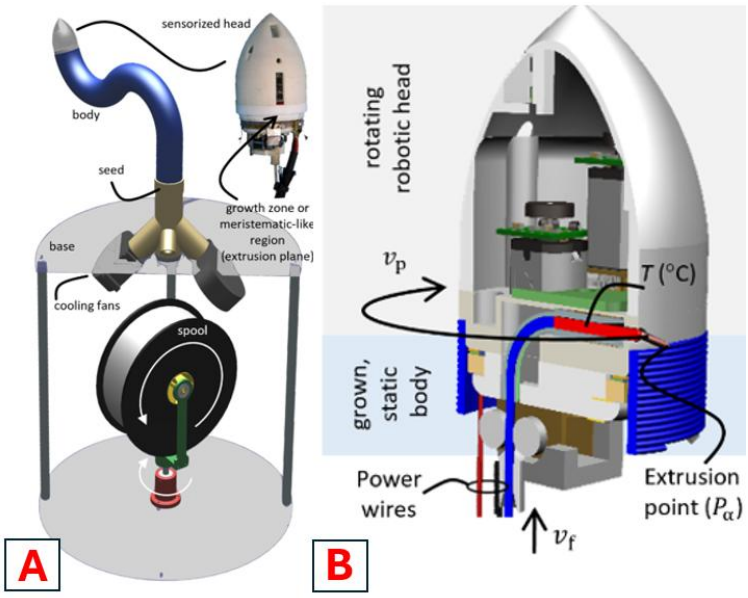

Figure 2.24. Design and working principle of the FiloBot system. (A) CAD model showing the main components of the growing robot, including the sensorized head, the extruded body, and the base station. The base houses the seed element, cooling fans, and a spool mechanism that supplies the filament material for extrusion. The robotic head integrates an FDM-based extrusion module and an onboard control unit for growth regulation. (B) Simplified schematic of the growth mechanism, defined by three key control parameters: the filament feeding speed ($v_f$), the plotting head rotation speed ($v_p$), and the extrusion temperature (T).

## 2.5 Discussion and summary

In summary, current actuation mechanisms for robotic colonoscope and intraluminal robots can be broadly categorized into electromechanical, fluidic, smart material, and magnetic systems. Electromechanical actuation offers precise control and reliability but suffers from limited flexibility and miniaturization. Fluidic actuation provides excellent compliance and bioinspired motion through pneumatic or hydraulic transmission, yet exhibits control complexity and delayed response. Smart material actuation shows promise for miniaturized and adaptive systems, though it is constrained by low force output and slow response times. Magnetic actuation enables non-contact, wireless manipulation and improves patient comfort, but its propulsion efficiency is limited by field decay and the complexity of external magnetic setups.

Table 2-3 Comparison of the principal actuation mechanisms used in robotic colonoscope and intraluminal robotic systems, summarizing their characteristic advantages, limitations, and representative studies.

| Actuation type | Typical implementation | Main advantages | Main limitations |
|---|---|---|---|
| Electromechanical actuation | Electric motor with transmission mechanisms (wheels, worm drive, tracks). | Mature technology, precise control, fast response. | Low compliance, bulky structure, complex transmission, unsuitable for confined lumens. |
| Fluidic actuation | Pneumatic chambers, hydraulic bladders, or water-jet propulsion. | High compliance, bio-inspired motion, capable of peristaltic propulsion. | Complex control, slower response, energy losses, dependency on tubing. |

| | | | |
|---|---|---|---|
| Smart-material actuation | SMA, SMP, DE, piezo and other responsive materials. | Miniaturization potential, variable stiffness, silent operation. | Low output force, slow response, complex control, temperature sensitivity. |
| Everting (growing) actuation | Material extrusion or deposition at the tip (FDM-like printing, plant-inspired growth). | Continuous body formation, inherently smooth motion, minimal friction with environment. | Slow growth, high energy use, and complex material supply. |
| Magnetic actuation | External permanent magnet coupled with internal magnet or electromagnetic coils. | Non-contact wireless control, high safety, structural flexibility. | Limited propulsion force, magnetic-field attenuation, bulky and costly external system. |

Table 2-3 summarizes the main locomotion architectures adopted in robotic systems. Wheeled designs are efficient on rigid tubular surfaces but lack adaptability to varying lumen diameters. Legged and peristaltic systems exhibit high compliance and bio-inspired motion yet suffer from limited propulsion speed and complex coordination. Tracked mechanisms, by contrast, provide continuous and stable traction, making them suitable for soft and curved intestinal environments.

Table 2-4 Locomotion mechanisms for robotic colonoscope.

| **Actuation type** | **Typical implementation** | **Main advantages** | **Main limitations** |
|---|---|---|---|
| wheeled | Motor with gearbox, flexible shaft, DC motor, etc. | Simple, efficient on smooth lumen, low power. | Poor adaptation to bends and diameter changes, slippage on wet tissue. |
| Legged, inching clamps | Motorized linkages, SMA, pneumatic micro-clamps. | High obstacle negotiation, precise step control. | Complex coordination, low speed, potential tissue stress at anchors. |

| | | | |
|---|---|---|---|
| Tracked | Motor to worm or pulley, flexible shaft, electro-hydraulic hybrid, etc. | Large contact area, strong traction, stable speed, tolerant to mucus. | Higher mechanical complexity, belt wear, needs wall-press management. |
| Wall-press | Pneumatic or hydraulic balloons. | Safe contact, good bend navigation, skill independent. | Slow, control complexity, energy demand. |
| Peristaltic | Pneumatic multi-chamber, hydraulic bladders, SMA, micro-motor, etc. | Bio-inspired, compliant, smooth motion. | Low movement efficiency and limited propulsion. |
| Helical screw propulsion | Internal motor, magnetically driven rotation. | High efficiency in viscous, compact. | Limited in tortuous, variable-diameter segments, potential mucosal shear. |
| Water-jet | High-pressure water pump, etc. | Non-contact with wall, low friction, ,fast in liquid-filled lumen. | Requires liquid distension, jet control complexity, integration burden. |
| Magnetic | External permanent magnet or coils. | Wireless control, good safety, precise orientation. | Force decays with distance, external setup. |
| Everting (growing) | Material deposition or tip eversion using pneumatic or extrusion-based mechanisms. | Continuous body formation, smooth and low-friction motion, high adaptability to complex paths. | Slow growth rate, complex material supply, limited control, and low clinical feasibility. |

As can be seen from Table 2-4, different locomotion mechanisms for robotic colonoscopes present distinct characteristics: conventional tracked and wheeled structures have high traction

stability and propulsion efficiency, but lack active adjustment ability to intestinal diameter changes; wall-press and expansion mechanisms exhibit excellent lumen adaptability and contact controllability, yet their propulsion speed and efficiency are relatively low; magnetic and water-jet actuation avoids direct friction but suffers from unstable output force or complicated system integration. Based on the above analysis, the proposed robot integrates the advantages of multiple schemes and overcomes their respective shortcomings: it uses an external motor, flexible shaft and worm drive to realize stable tracked propulsion, inheriting the high-efficiency traction feature of traditional tracked mechanisms; meanwhile, a radial expansion mechanism is introduced to actively adjust the robot size, so as to control contact area, contact force and traction, which absorbs the good adaptability of wall-press and expansion structures; in addition, differential torque control is employed to achieve flexible steering, further improving the robot's manoeuvrability in tortuous environments. The proposed design thus achieves a comprehensive balance among propulsion stability, diameter adaptability and motion flexibility.

It is worth noting that wall-press robots maintain high propulsion efficiency and robust motion stability in slippery, variable-diameter lumens and are therefore widely adopted in many intraluminal robotic designs [38] [41]. It centres on actively regulated normal force, providing reliable anchoring and safe traction in variable-diameter, slippery, and high-curvature lumens, which is essential for high possibility with low tissue load [23] [43].

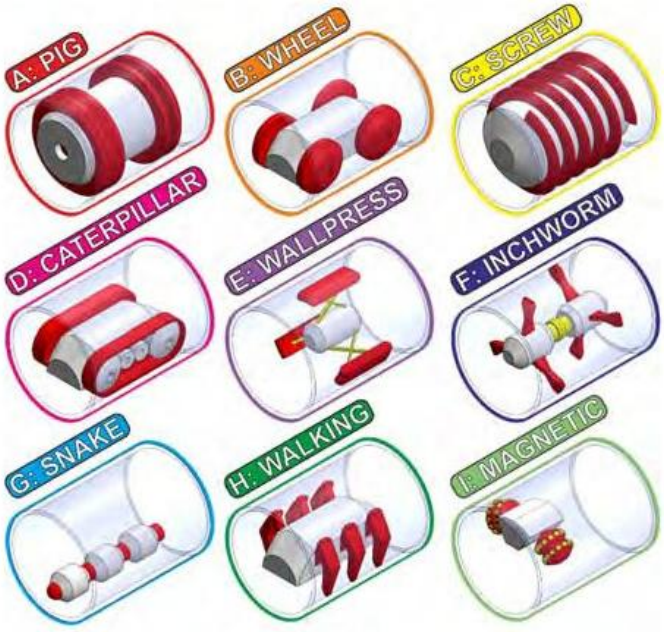


Figure 2.25. Basic in-pipe robotic locomotion types. [38]

Overall, despite significant progress across these domains, achieving a balance between compliance, propulsion strength, controllability, and compactness remains a major challenge for colonoscope applications. Most existing systems emphasize one aspect at the expense of others, resulting in trade-offs between safety, power, and manoeuvrability. Consequently, developing an actuation mechanism capable of delivering stable propulsion, adaptive deformation, and controllable steering within confined anatomical environments is essential for advancing robotic colonoscopy.

In order to cope with the flexible and wrinkled colon environment, we put forward the requirements for the design of colonoscopy in order to meet its movement requirements：

Challenges of colonoscopy based on realistic colonic physiology:

- **Constrained lumen**: limited intraluminal space restricts manoeuvrability and tool deployment.
- **Complex anatomy:** a long, narrow, and highly tortuous pathway makes navigation difficult.
- **Low-friction environment**: mucus and a smooth mucosal surface reduce traction and increase slip risk.

Design requirements for a robotic colonoscope:

- **Flexible steering:** precise and responsive orientation control in three dimensions.
- **Geometric adaptability:** accommodation of variable lumen diameter and curvature.
- **Safe, stable actuation**: sufficient propulsion with minimized tissue interaction forces.
- **Operational efficiency**: an actuator and control strategy that reduce procedure time.

Guided by this principle, the proposed robotic colonoscope with an external motor delivers continuous traction through a flexible shaft and worm gear, while four tracks incorporate independently controlled hydraulic expansion modules that tune normal contact force and contact area, thereby decoupling traction from tissue load and enabling coordinated optimization. The mechanism increases pressure in enlarging segments for secure anchoring, reduces pressure in sensitive or lubricated regions, and uses differential expansion for steering and posture stabilization. The next chapter details the architecture, control strategy, and experiments that substantiate the efficacy of this wall-press focused, hybrid tracked design in both propulsion performance and mucosal safety.

# 3 Development and characterization of the first Robotic colonoscope

*The content of this chapter has been published in Frontiers in Robotics and AI ], under the title "Design and preliminary evaluation of a track-based robotic colonoscope with a shape-adaptable tip for propulsion." (Du, J et al., 2025).*

This chapter presents the design and implementation of a track-based robotic colonoscope prototype. Following contents detail the design principle, structural composition, and assembly process of the expansion mechanism, and experimentally verifies its feasibility and stability in tip-size adjustment and shape retention. These results provide the foundation for subsequent investigations into the robot's propulsion performance and steering behaviour.

## 3.1 Design rationale and key design elements

The preceding review systematically summarized the development of robotic colonoscopes and provided a comparative analysis of different actuation strategies, including electric, pneumatic, hydraulic, and hybrid drives, etc. A horizontal comparison was also conducted among existing prototypes, focusing on their actuators, locomotion performance, and adaptability within tortuous luminal environments. The review revealed that, due to the colon's narrow and curved anatomy with a slippery mucosal surface, different actuation methods exhibit distinct advantages and limitations in terms of efficiency, responsiveness, controllability, and safety. Therefore, selecting an actuation scheme that ensures stable propulsion and safe operation in such a constrained environment is a critical design challenge.

Given the unique physiological characteristics of the human colon, the design of a robotic colonoscope must carefully address several environmental and operational conditions:

- First, the lumen diameter varies continuously along the colon, and the inner wall consists of soft, elastic tissue that can undergo local deformation and displacement. Under such conditions, maintaining continuous traction and stable motion requires the robot to have sufficient contact area and to maintain firm wall attachment throughout movement.
- Second, the colonic lumen is not perfectly circular, and its geometry and curvature differ significantly across segments. If the robot can adapt its shape dynamically in response to lumen variations—adjusting its configuration to match local curvature and

diameter - it can greatly enhance its overall stability and propulsion efficiency in complex pathways.

- Finally, the interior of the colon is wet and slippery, with the surface covered by a mucus layer that drastically reduces friction. Conventional wheel-based or peristaltic mechanisms tend to suffer from slippage, idle motion, or discontinuous propulsion under such conditions. Therefore, maintaining stable frictional traction on a slippery surface is a key challenge that must be addressed in the design of any robotic colonoscope.

In summary, the complexity of the colonic environment imposes stringent requirements on both the structural design and actuation strategy of the robot. The system must maintain stable traction within a wet, deformable, and variable-diameter lumen, while simultaneously adapting to changes in curvature and size to prevent excessive wall pressure or motion instability. To address these challenges, the proposed prototype integrates several key design elements:

- A multi-channel structure, which allows the separation of power transmission, actuation, and sensing modules to improve system modularity.
- A wall-pressing mechanism, designed to maintain continuous traction force against the intestinal wall and ensure stable locomotion.
- A track-based propulsion system, providing bidirectional movement and effective frictional coupling with the lumen surface.
- A flexible rotating shaft, which delivers motor torque from an external drive unit while allowing the robot body to navigate through curved sections of the colon.

The multi-chamber structure enables zoned control of shape and pressure, allowing the robot to actively conform to the varying geometry of the colon, separately. The wall-press mechanism provides a controllable normal preload that ensures firm wall contact and stable traction in low-friction, mucus-covered conditions. The track-based propulsion system ensures continuous and controllable motion, reducing the risk of slippage. Together, these three design elements form the core framework of the proposed robotic prototype, enabling safe, stable, and efficient locomotion within the complex environment of the colon.

## 3.2 Overall design of the first prototype

### 3.2.1 Design objectives and overall concept

The first prototype of the robotic colonoscope was designed to validate the feasibility of a track-based propulsion mechanism combined with an adjustable wall-press system. The robot

aims to achieve three primary functions within a simulated colon: stable propulsion, diameter adaptability and steering ability.

The overall system consists of four main subsystems:

1. Driving system: an external motor transmits power through a flexible shaft to a worm gear, driving four tracks at equal speed;
2. Wall-press adjustment system: a bellows-based expansion mechanism regulates the tip diameter and corresponding normal contact force;
3. Transmission and support structure: including a central shell, support arms, and track frames that maintain the robot's geometry and transmit wall pressure;
4. Control and measurement system: designed to regulate motor speed and pneumatic input based on the predefined traction force and velocity, while simultaneously recording propulsion force and movement data.

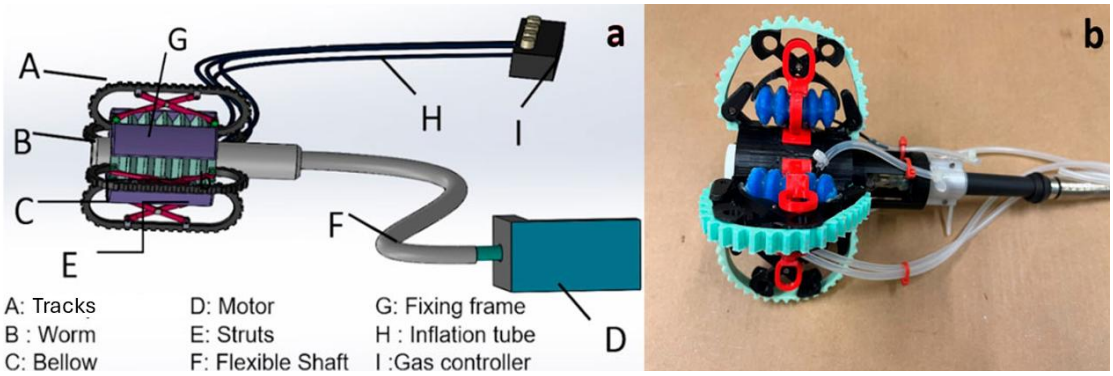


Figure 3.1. **(a)** A conceptual diagram of the robotic endoscope. The endoscope tip is driven using a worm couple **(B)** actuated by an external motor **(D)** through a flexible shaft. The tip also features four independently controlled expansion mechanisms enabled by a pneumatic bellow **(C)** and strut mechanisms **(E)**, **(b)** The expandable tip. The external motor is connected to a Arduino UNO to realize locomotion of the device (not equipped with camera lens).

The overall design follows the principle of simplicity, functional verification, and experimental accessibility, providing the physical foundation for subsequent optimization and theoretical modelling.

### 3.2.2 Design of the locomotion system

The robot employs an external-motor, flexible-shaft, and worm-gear transmission to achieve equal-speed propulsion of the four tracks. The motor is positioned outside, and torque is transmitted through a flexible shaft, allowing the main body to move freely inside the lumen

without being constrained by the drive unit. At the distal end, the flexible shaft connects to a worm gear that simultaneously meshes with four track-mounted racks distributed circumferentially around the central axis. This configuration ensures symmetrical and stable propulsion while avoiding the complexity of differential-driven mechanisms, as shown in Figure 3.2. The detailed fabrication and assembly procedures of this component are described in Section 3.3.

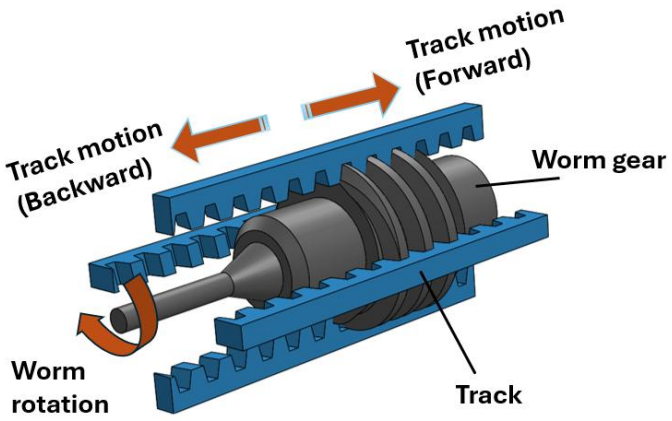


Figure 3.2. Schematic diagram of track-based locomotion. The motor rotation is transmitted through a worm gear to drive the track in the forward or backward direction, enabling linear motion along the colon wall.

Each track is fabricated from silicone with fine surface textures to enhance frictional contact with the inner wall. Internal guide rails and bearings maintain alignment and reduce vibration during motion. The entire transmission system is compact, efficient, and capable of generating stable and continuous traction within confined geometries.

3.2.3 Design of the bellow-based expansion mechanism.

To achieve adaptive diameter adjustment at the robot's tip, a bellows-based expansion mechanism was implemented at the front of the prototype. The bellows expands radially under internal pneumatic pressure, driving the outer support frame outward to press the tracks against the lumen wall. When the pressure is released, the bellows contracts, reducing the contact force and enabling controllable wall-press regulation.

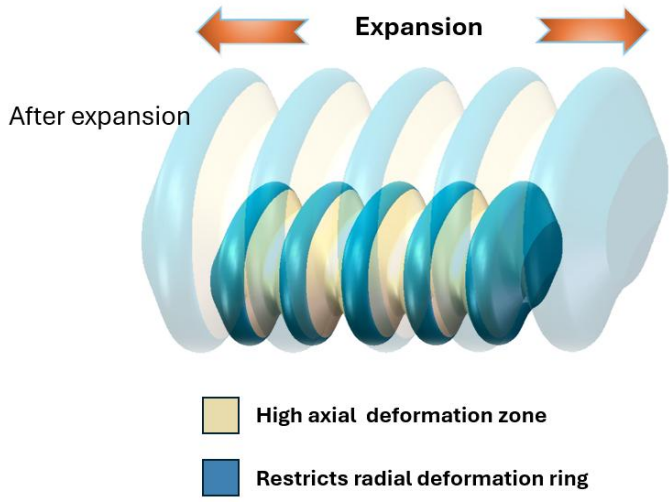


Figure 3.3. Schematic diagram of bellow.

To overcome the excessive radial expansion observed in conventional single-layer silicone bellows, a dual-hardness silicone composite design was adopted. The bellows is fabricated from two silicone materials with different Shore hardness values:

- The outer layer (high-hardness silicone, bule part) restricts radial deformation and maintains geometric stability.
- The inner layer (low-hardness silicone, faint yellow part) provides high axial flexibility, allowing the bellows to deform primarily along its longitudinal direction under pressure.

This material-layered strategy aims to maximize axial deformation while minimizing radial bulging, thereby improving expansion efficiency and ensuring directional consistency of the output force. When the pressure is applied, the constrained bellows generates a concentrated axial displacement that drives the support arms to extend, enabling precise wall-contact adjustment. In addition, the composite structure enhances fatigue resistance, maintaining stable deformation characteristics after repeated inflation-deflation cycles.

This section describes the design principle and structural configuration of the bellows expansion mechanism. The detailed fabrication process, material ratios, and moulding techniques are presented in Section 3.3 Fabrication and Assembly.

### 3.3 Fabrication and assembly

For ease of fabrication and experimental testing, a scaled-up prototype was produced at a 4:1 ratio relative to the intended clinical design. The upscaled dimensions allowed easier

integration of sensors and assembly of mechanical components, while maintaining the same geometric proportions and actuation principles as the final miniature version. The prototype has a nominal outer diameter of 140 mm in its non-pressurised state, corresponding to an equivalent full-scale diameter of approximately 35 mm [95].

### 3.3.1 Materials and fabrication methods

To validate the proposed design, the major components of the first prototype were fabricated and assembled according to the structural specifications. Rapid prototyping and manual assembly methods were adopted to ensure flexibility for experimental adjustments.

The actuation of the prototype is driven by an external stepper motor (NEMA 17, Rtelligent), controlled via an Arduino Uno microcontroller to regulate speed and rotation direction. Power is transmitted from the external motor to the robot body through a flexible shaft (as shown in Figure 3.4.), which serves as the primary torque transmission component.

Figure 3.4. Different kind of flexible shaft.

A flexible shaft is a multi-stranded, steel-wound transmission element capable of bending while reliably transmitting rotational motion. Compared with rigid shafts, it offers superior adaptability in confined spaces or along curved paths, making it particularly suitable for pipeline and endoscopic robotic applications where long, non-linear power transmission is required. Besides, it is also a common tool in daily life, which is very convenient to obtain and low in price, and is often used in electric drill equipment. It is worth emphasising that by positioning the motor externally, this configuration reduces the onboard size and heat accumulation of the robot as well as protects electronic components from mechanical stress and humidity within the lumen.

The transmitted torque drives a worm gear inside the body to actuate the tracks. Based on the production concept of easy access and low price, both the worm gear and the outer sleeve are fabricated using PLA via 3D printing, providing sufficient rigidity and enabling rapid prototyping for iterative optimization. The inner sleeve incorporates four longitudinal grooves that constrain lateral motion and relative sliding of the tracks, ensuring synchronized propulsion. The outer frame encloses the worm and track modules, forming a compact and stable structure.

To reduce excessive friction between the tracks and the sleeve, each track groove features an arc-shaped profile filled with lubricant, improving smoothness and minimizing wear during operation.

To limit the radial deformation of the bellows and maximize its axial expansion, two types of silicone materials with different hardness levels were used during fabrication. The blue section was made from Mould-Star 30 (Shore hardness 30A, Smooth-On, United States), while the faint yellow section was made from Eco-Flex 00-30 (Shore hardness 00-30, Smooth-On, United States), as shown in Figure 3.5. The harder outer silicone constrains radial expansion, whereas the softer inner silicone allows greater axial flexibility, enabling the bellows to deform primarily along its longitudinal direction.

During the preparation process, an air pump was used to evacuate air from the mixed silicone before casting, effectively preventing bubble formation within the material during curing. This degassing step significantly improved the structural integrity of the cured silicone and reduced the risk of cavity fractures or local stress concentration during repeated inflation–deflation cycles.

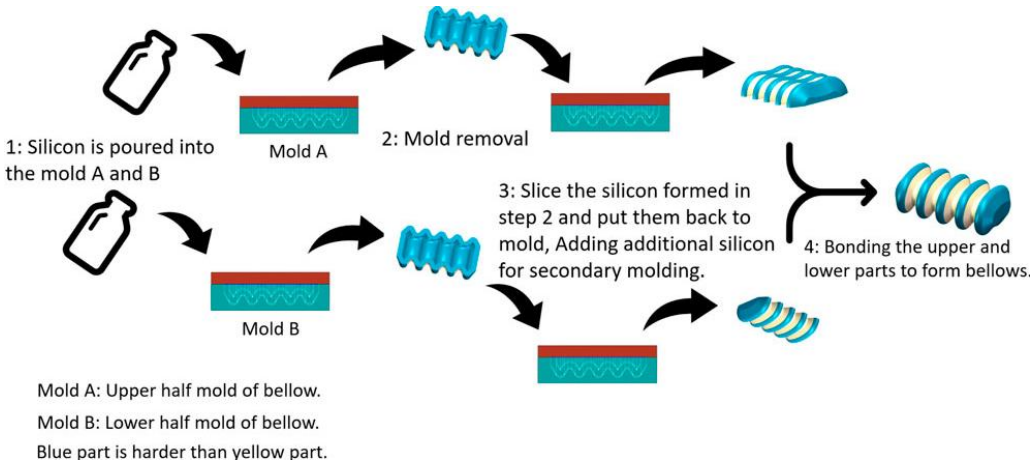


Figure 3.5. Fabrication of the soft-bodied bellows.

3.3.2 Assembly procedure.

The assembly procedure involved the following steps:

1. **Housing and worm installation:** Bearings were press-fitted into the housing seats, and the worm was installed with slight preloading to minimize backlash.
2. **Track and guide installation:** Four tracks were positioned in their respective guide slots at 90° intervals around the circumference. Track tension was adjusted to ensure synchronized motion without slippage.
3. **Bellows and support arm mounting:** The bellows was secured to the front cavity and linked to the support arms so that axial expansion pushed the outer track frames outward.
4. **Flexible shaft and motor coupling:** One end of the flexible shaft was connected to the worm gear through a coupling, and the other end to the external motor shaft. Rotation direction and synchronization were verified.
5. **Pneumatic line and control system connection:** The bellows chamber was connected to the pressure source via tubing and control valves, and leak-tightness was verified through low-pressure testing.
6. **Final calibration:** The bellows expansion and contraction responses were tested under low pressure to confirm radial stability and smooth axial deformation before full operation.

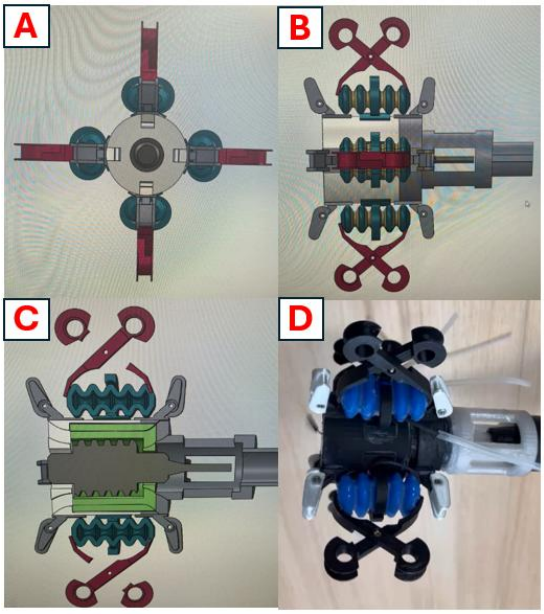

Figure 3.6. Structure and working principle of the expansion mechanism. (A) Top view of the mechanism showing the four-track arrangement;(B) Side view illustrating the transmission and linkage structure; (C) Cross-sectional view of the expansion unit, showing the deformation of the chamber and track interaction; (D) Physical prototype of the assembled mechanism.

The assembly process begins with the central driving unit, where the worm gear and bearings are mounted inside the housing, and the centre distance and meshing clearance are adjusted to ensure smooth transmission. Next, the bellows-based expansion module is fixed at the front cavity and connected to the four support arms, enabling axial outward motion of the track edges during inflation for wall-press regulation.

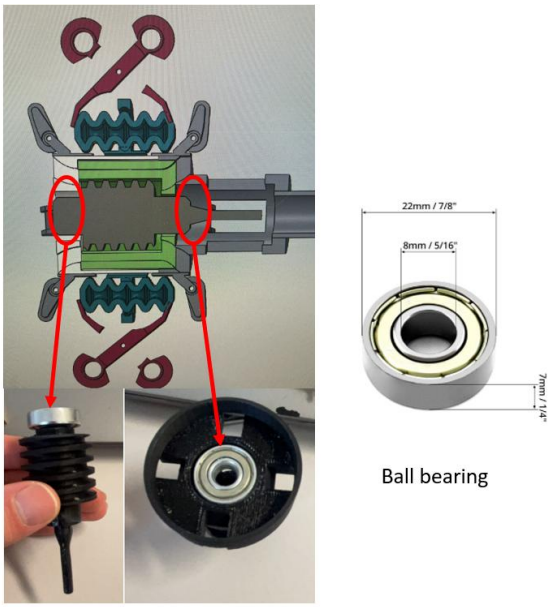


Figure 3.7. Integration of the ball bearings with the worm-gear housing. The CAD model (left) illustrates the position of the ball bearings supporting the worm shaft at both ends. The photographs (bottom) show the corresponding fabricated components, while the right image presents the bearing dimensions (8 mm inner diameter, 22 mm outer diameter, and 7 mm thickness).

Figure 3.7. illustrates the structural integration of the worm gear and its supporting bearings within the housing. Both ends of the worm shaft are supported by deep-groove ball bearings (8 mm inner diameter, 22 mm outer diameter, and 7 mm thickness) to ensure rotational stability and concentric alignment. The bearings are press-fitted into the mounting seats at both sides of the housing, as indicated by the red highlights in the figure.

This configuration effectively reduces frictional resistance during rotation and prevents vibration or energy loss caused by misalignment or uneven support. The Figure 3.6. shows the

assembled components, where the bearings are precisely positioned at both ends of the worm shaft, enabling smooth and low-resistance rotation within the compact housing. This structural design ensures continuous power transmission and provides a solid mechanical foundation for the synchronized movement of the tracks.

The four track modules are then mounted at 90° intervals around the circumference, maintaining symmetrical distribution for balanced traction. As shown in Figure 3.6., the image A, B and C illustrate the internal arrangement from multiple views, showing the spatial relationship among the worm drive, bellows, support arms, and track frames. The lower right image (D) presents the fabricated prototype after assembly, demonstrating the consistency between the designed model and the physical implementation.

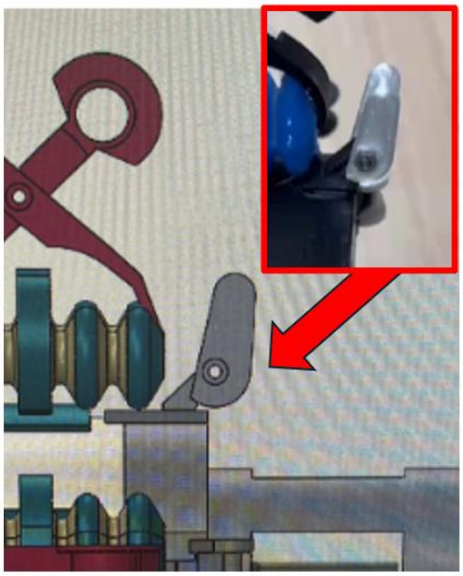

Figure 3.8. Connection between the bellows and supporting arm.

Figure 3.8. illustrates the connection mechanism between the bellows and the supporting arm. The CAD model shows the hinge joint between the bellows and the supporting arm, which converts the axial deformation of the bellows into radial motion of the track module. The inset image illustrates the corresponding fabricated component after assembly. The front end of the bellows is attached to the arm through a hinge joint, allowing the axial displacement generated during bellows expansion to be converted into radial motion of the track module. The hinge employs a pin-bolt configuration that not only maintains flexible rotation and reliable linkage under repeated loading cycles, but also minimizes frictional resistance and prevents motion interference, ensuring smooth transfer of the bellows' axial deformation to the supporting arm without unwanted misalignment or jamming.

The inset image shows the fabricated component after assembly, demonstrating a close match with the CAD model. The mechanism enables smooth and consistent movement of the supporting arm without misalignment or jamming, effectively transforming the bellows' axial expansion into radial extension, an essential linkage in the wall-press actuation chain.

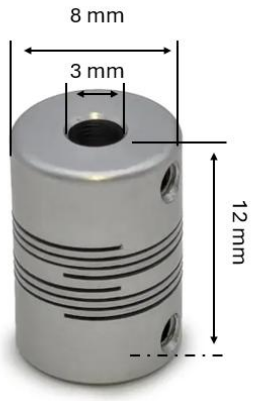


Figure 3.9. Shaft coupler.

After the bellows and supporting arms were assembled, the drive transmission system was installed. The flexible shaft connects to the worm gear at one end and to the external stepper motor at the other, with both interfaces coupled by shaft couplers (3 mm to 3 mm), as shown in Figure 3.9. This coupling configuration ensures precise torque transmission and maintains coaxial alignment while allowing limited axial and angular compensation, thus preserving stable power delivery even when the flexible shaft is slightly bent or offset. The drive chain connecting the motor and the worm remains continuous and backlash-free, ensuring synchronized motion of all four tracks and smooth propulsion.

Following assembly, all rotating components were manually inspected to verify smooth operation without jamming or interference. The pneumatic line and control system were then connected, and preliminary tests confirmed the coordinated actuation between the bellows expansion and track propulsion. The final assembly achieves a compact structure with well-integrated power transmission, wall-press adjustment, and mechanical support.

### 3.4 Control system

For the motor drive module, a NEMA 17 stepper motor is powered through a TB6600 driver, receiving control signals from an Arduino UNO microcontroller. The user interface allows manual input through three control elements:

- ON/OFF button – to start or stop the motor;

- Direction button – to switch the rotation direction, enabling forward or reverse motion of the tracks;
- Potentiometer – to adjust the input voltage and regulate the motor speed.

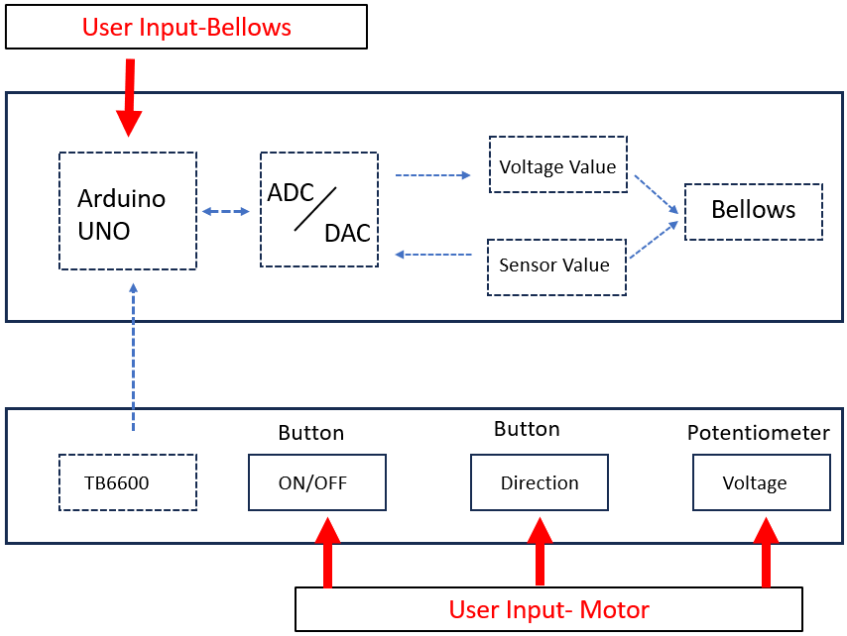


Figure 3.10. Open loop control of four independent bellows using Arduino microcontroller.

The bellows actuation module operates under an open-loop control scheme. The user defines a desired voltage level, which is converted by the Arduino UNO and DAC module into an analogy signal that directly drives the pneumatic actuator (air pump or valve) connected to the bellows. Since no feedback sensor is used in this configuration, the bellows expansion is determined solely by the input pressure magnitude. This open-loop arrangement provides a simple and fast-response setup suitable for prototype testing and performance evaluation.

### 3.5 Modelling

To analyse the propulsion characteristics of the robotic colonoscope, a simplified mathematical model was developed to describe the main force interactions and motion behaviour during locomotion. As illustrated in Figure 3.11., the robot's motion inside the colon lumen is primarily determined by the driving torque, the frictional forces, and the normal contact forces between the tracks and the inner wall. For analytical convenience, the colon is approximated as a rigid cylindrical tube, and its deformation or peristaltic motion is neglected. This assumption allows us to focus on the fundamental relationship among the driving torque, wall pressure, and frictional traction, forming a clear analytical foundation for propulsion analysis.

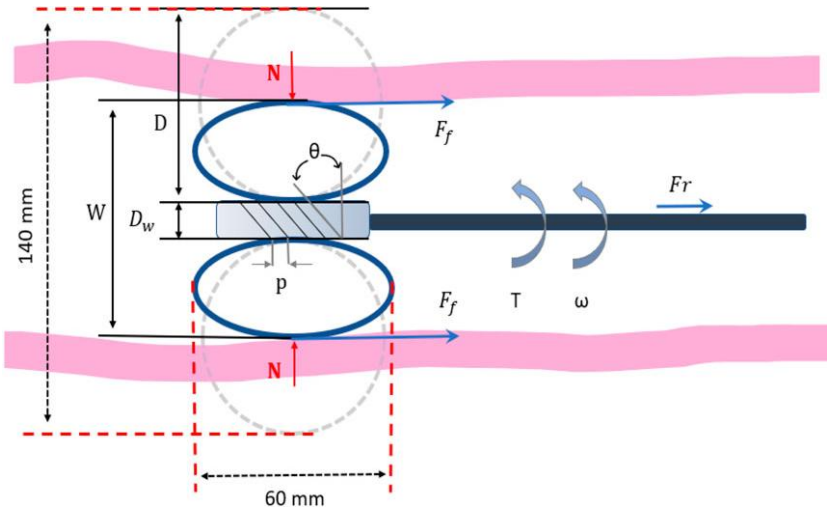


Figure 3.11. Diagram of the kinematic mechanism of the expansion tip.

Although this simplified model cannot fully capture the compliant and nonlinear properties of the real colon, it provides an essential theoretical basis for the subsequent experiments. Future work will incorporate elasticity and geometric variations of the colon wall to obtain a more physiologically realistic model.

In this case (the normal force as the product of the track's elastic modulus and compression), the maximum static friction between the colon wall and the track is：

$$F_f = n\mu_c N = n\mu_c k(D - \frac{W-D_w}{2}) \quad (1)$$

Where n denotes the number of tracks, $\mu_c$ is the frictional coefficient between the track and lumen wall, N is the normal force of track, k is the radial equivalent elastic modulus of track, D is the diameter of track, W is the diameter of colon lumen, $D_w$ is the diameter of the worm gear.

In this initial study, only the static-friction model (Equation 1) was used to evaluate the robot's capability to overcome starting resistance. This assumption is reasonable because, under low-speed and intermittent operation, the difference between static and kinetic friction is relatively small, and adhesion effects are negligible once movement begins. However, dynamic friction and adhesion will be introduced in future work to improve the accuracy of propulsion-performance and safety evaluation under more complex conditions.

The motor drives the sole worm gear, and the angular velocity of the motor can be expressed as follows:

$$v = \frac{D_w tan\theta\omega}{2} = \frac{\omega p}{2\pi p} \quad (2)$$

Where ω represents the angular velocity of the motor, p denotes the pitch of the worm, and v is the velocity of the robot.

The propelling force and torque generated by the worm gear are as follows:

$$F_r = Ncos\theta - \mu Nsin\theta \tag{3}$$

$$T = \frac{D_w}{2}(Nsin\theta - \mu Ncos\theta) + T_f \tag{4}$$

Where N indicate the normal force, μ is the frictional coefficient between the worm and the track, T represents the output torque of motor, and $T_f$ is the reaction torque (resulting from the friction between worm and the tracks).

According to the equation pitch angle of worm,

$$tan\theta = p/D_w\pi \tag{5}$$

Therefore, based on the previous equations (3), (4), and (5), the relationship between motor torque and propelling force can be derived as follows:

$$F_r = \frac{2(\pi D_w - \mu p)(T - T_f)}{D_w(\mu\pi D_w + p)} \tag{6}$$

if we assume the relationship between output torque and rotation speed is linear, it can be determined as follows:

$$\omega = \omega_n(1 - {}^{T}/_{T_M}) \tag{7}$$

Where $\omega_n$ is angular velocity under no load, $T_M$ is maximum torque when angular velocity is zero.

Therefore, according to equations (6), (7), the max propelling force of the robot can be determined as follows:

$$F_{rmax} = \frac{2(\pi D_w - \mu p)(T_M - T_f)}{D_w(\mu\pi D_w + p)} \tag{8}$$

The worm gear transmission ratio is:

$$i = \frac{Z_w}{Z} \tag{9}$$

Where $Z_w$ and $Z$ represent the number of teeth of worm and track respectively, which are shown in Table 2.

The linear velocity of the worm can be calculated using:

$$v_w = \frac{\pi \mathrm{D_w} n_w}{60} \tag{10}$$

Where $n_w$ represents the worm's rotational speed, which corresponds to the motor's angular speed. Neglecting the sliding and frictional losses in the flexible shaft, the linear velocity of the prototype can be approximated by:

$$v = i \cdot v_w \tag{11}$$

Table 3-1 Geometric and transmission parameters of the prototype.

| Parameter | Symbol | Dimension |
|---|---|---|
| Worm teeth number | $Z$ | 5 |
| Track teeth number | $Z_w$ | 34 |
| Prototype frame width (mm) | -- | 140 |
| Track width (mm) | -- | 7.5 |
| Belt height (mm) | -- | 4.5 |
| Tooth length (mm) | -- | 3 |
| Worm gear pitch (mm) | p | 3 |
| Worm gear diameter (mm) | $\mathrm{D_w}$ | 28 |

### 3.6 Experiment tests and results

This section presents the experimental verification of the proposed robotic colonoscope prototype.

Based on the design and theoretical modelling introduced in the previous sections, a series of tests were conducted to evaluate the robot's propulsion performance, wall-press adjustment capability, and overall motion stability inside a simulated colon environment. The experiments aimed to validate the relationship between driving torque, frictional interaction, and output force predicted by the mathematical model, as well as to examine the feasibility of the bellows-based expansion mechanism. The obtained results are analysed and compared with the theoretical predictions to assess the consistency and reliability of the developed system.

3.6.1 Force and displacement measurements of bellows.

Bellows play a very important role in the whole expansion mechanism, even in the robot system, so our first experiment will start with bellows.

Figure 3.12. illustrates the measurement of three forces: Force A, Force B, and Force C (abbreviated as $F_A$, $F_B$, $F_C$), acting at different points of the expansion mechanism as the internal pressure of the bellows changes. Here, $F_A$ represents the normal force applied at the top of the supporting strut, $F_B$ denotes the radial force at the same position, and $F_C$ corresponds to the axial force generated by the bellows.

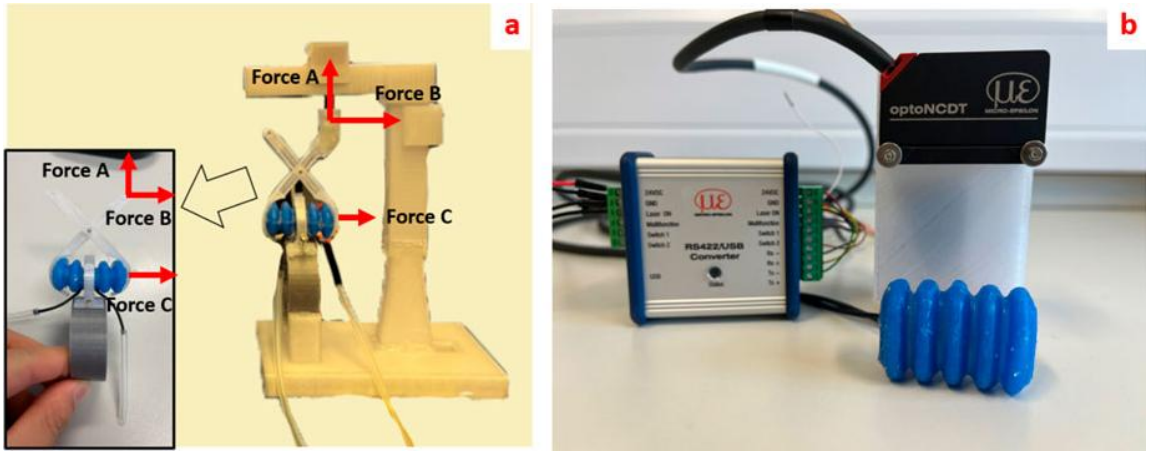


Figure 3.12. Force sensor experimental platform of the bellow with strut (insert shows the direction and position of the force measured in the experiment); b) Laser sensor platform for detecting the deformation of bellows.

The maximum normal force produced by the bellows, $F_A$, was measured to be 3.89 N. During the tests, the bellows cavity air volume was varied between -5 mL and 10 mL, corresponding to a working pressure range of -101 mbar to 283 mbar, as shown in Figure 3.13.

To ensure the accuracy and repeatability of the measurements, each experimental condition was tested ten times without altering any other parameters. All measurements were conducted independently to quantify the random error and to calculate the mean and standard deviation of the collected data. This procedure enabled the acquisition of more reliable measurement results and provided insight into the random fluctuations and stability of the experimental system.

The experimental results for the bellows displacement measurements were obtained using a laser sensor (optoNCDT 1420, MICRO EPSILON, Germany), as illustrated in Figure 3.12. b). The maximum lengthwise displacement of the bellows is 8.98 mm. Significant changes were

also observed in other dimensions, specifically 6.3 mm in the height and 2.12 mm in the width, as shown in Figure 3.13. c). These findings demonstrate that two silicon materials of different hardness can create a flexible linear actuator with relatively constrained radial deformations.

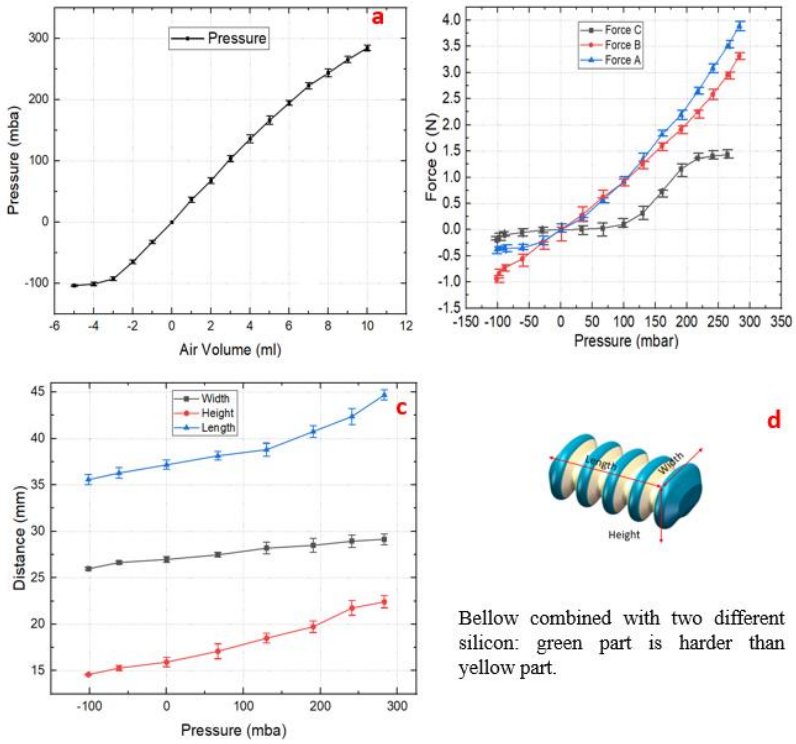


Figure 3.13. The relationship between the air volume inside the bellows and the internal pressure; b) $F_A$, $F_B$ and $F_C$ as a function of pressure change in one bellow; c) Displacements of the bellow along width, height and length pressure in the bellow; d) Bellow rendering.

The four expansion mechanisms are independently actuated by regulating the air pressure within each bellows, enabling the prototype to adapt to variations in the colon's diameter and morphology.

The bellows act as the core linear actuators of the expansion system. By inflating or deflating the bellows, their internal volume increases or decreases correspondingly, driving a pair of scissor-like linkages to move vertically. This motion adjusts the position of the track units and consequently alters the overall diameter of the robot's head section.

The prototype used in this study was fabricated at a 4:1 scale relative to the intended clinical design, with a non-pressurised diameter of 140 mm. According to the experimental data- obtained as the average of ten repeated measurements- activation of the expansion mechanism resulted in an approximate 53% change in diameter, ranging from 99.6 mm to 151.6 mm.

When the bellows were subjected to negative pressure, they contracted, causing the track frame diameter to increase beyond its original size. Conversely, when positive pressure was applied, the bellows expanded and the scissor mechanisms retracted, leading to a reduction in the prototype's diameter, as illustrated in Figure 3.14.

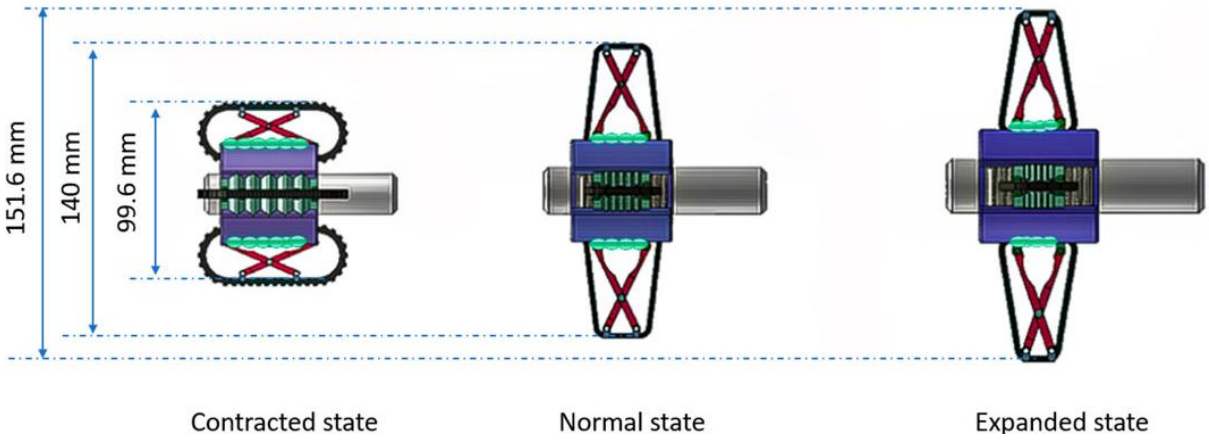


Figure 3.14. Schematic diagram of working principle of expansion mechanism. Left - bellows are subjected to negative pressure; Middle - bellows are at atmospheric pressure, Right - bellows are subjected to positive pressure.

### 3.6.2 Prototype testing

Following the description of the experimental setup, this section presents the testing results of the prototype. The tests were carried out to verify the propulsion efficiency and size-adaptable regulation performance predicted by the model, and to evaluate the mechanical stability of the expansion mechanism during operation.

#### 3.6.2.1 Preparation of testbed

A straightforward experimental platform was established to evaluate the performance of the prototype. The testbed consisted of a 3D-printed PLA support frame, a transparent acrylic pipe, a force sensor, and the robotic prototype. The rigid acrylic tube simulated a straight segment of the colon, providing a controlled environment for testing the propulsion and expansion capabilities of the robot. Although this setup does not replicate the compliance or geometric complexity of the human colon, it effectively isolates the fundamental propulsion and wall-press mechanisms and provides essential data for validating the design concept.

The functionality of the prototype was evaluated within tubes of matching dimensions to its head section. To investigate the effects of surface friction on traction performance, experiments were conducted using three types of internal surfaces:

(1) a commercial silicone -based colon skin sheet (Bowel-9 mm, Lifelike, Canada),
(2) a smooth transparent acrylic tube, and
(3) an acrylic tube with the inner surface covered by foam or artificial tissue to alter its frictional properties.

A 3D-printed bracket was used to fix the tube and prevent displacement during operation.

3.6.2.2 Prototype propelling speed

Figure 3.15. compares the theoretical and measured linear velocities of the prototype across the three surfaces. Due to frictional losses within the flexible shaft, worm gear, tracks, and the contact with the tube wall, the measured velocities were consistently lower than the theoretical predictions, which neglect these losses. Each data point represents the average of five repeated measurements.

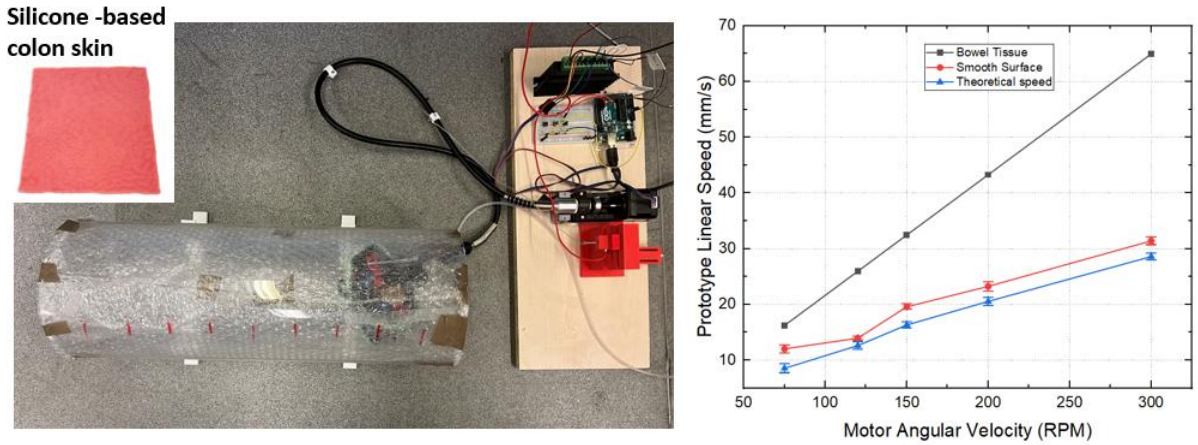


Figure 3.15. Locomotion experiment of the prototype.

The motor angular velocity was set to 75, 120, 150, 200 and 300 rpm to explore corresponding linear velocity of the prototype; Different friction coefficients of the tube surface were emulated using foam, artificial tissue (made of silicone, with mucus) and smooth surface. At a motor speed of 300 rpm, the prototype achieved a maximum velocity of 32.04 mm/s on the smooth acrylic surface and 29.29 mm/s on the wet artificial tissue surface. These results represent the maximum capability of the scaled-up (4:1) prototype and confirm the feasibility of the proposed actuation mechanism. For clinical application, the motor speed can be precisely controlled to ensure safe and slow locomotion within the colon, maintaining operational effectiveness without compromising patient safety.

3.6.2.3 Prototype propelling force

In the ideal theoretical scenario, the motor's resisting torque is assumed to counteract only the frictional forces between the track and the worm gear, while friction within the flexible shaft and other forms of power loss are neglected. According to the motor's torque–speed curve, within the operating range of 75 - 300 rpm, the output torque remains almost constant.

Under these near-constant conditions, the minor torque variation can be ignored, allowing the prototype's theoretical propulsion force to be derived directly from the corresponding analytical formula. To further validate this propulsion force under different rotational speeds and frictional conditions, a dedicated test platform was constructed to measure the robot's propelling performance. The purpose of this model is to analyse the generation of traction force and its dependence on contact conditions, and to provide a theoretical basis for interpreting the experimental results.

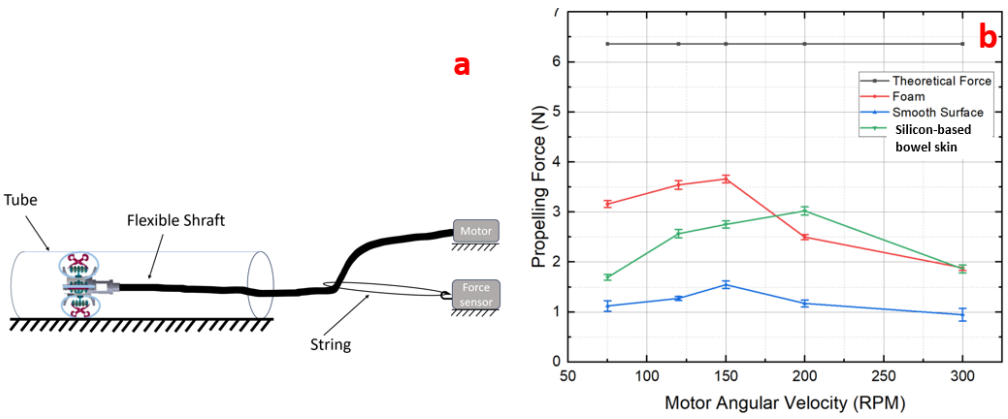


Figure 3.16. (a) Propelling force experiment schematic diagram; (b) Comparison of different propelling forces as a function of motor speed measured on three different surfaces with varying friction coefficients and surface hardness.

A force sensor (Model LSb201, FUTEK, United States) was mounted on the testbed and connected to the flexible shaft through a string to record the propelling force of the prototype as shown in Figure 3.16. (a). The propulsion tests were conducted on three types of surfaces with distinct friction coefficients, smooth acrylic, foam and silicone -based colon skin, while the motor speed was varied from 75 to 150 rpm. For each condition, five repeated experiments were performed to ensure repeatability, as illustrated in Figure 3.16. (b).

Within the 75-150 rpm range, the measured forces increased as expected. However, when the rotational speed exceeded 150 rpm, the propelling force began to decrease. This reduction is

attributed to the loss of transmission efficiency in the flexible shaft at higher speeds, which weakens the coupling between the worm and the tracks and results in partial slippage.

The experimental results showed that the maximum propelling forces were 1.47 N on the smooth surface, 2.83 N on silicone -based colon skin, and 3.61 N on the foam surface. Interestingly, the prototype exhibited greater stability when operating on the silicone -based colon skin surface. This is likely due to the soft and compliant nature of the material, which deforms slightly into a concave shape under load, thereby increasing the effective contact area between the robot and the wall.

This observation suggests that the mechanical compliance and surface properties of the surrounding medium significantly influence the robot's propulsion performance. Further studies should therefore focus on a systematic analysis of material characteristics and their effects on the robot-environment interaction.

3.6.2.4 Experiment of diameter size-adapting

Following the propulsion performance tests, additional experiments were conducted to evaluate the prototype's adaptability to lumens of varying diameters. This investigation aimed to assess how the robot's propulsion and expansion mechanisms respond to different lumen sizes, further validating the system's ability to conform to the variable geometry of the colon.

To evaluate the prototype's adaptability to varying lumen sizes, experiments were conducted using four tubes with inner diameters of 100 mm, 120 mm, 140 mm, and 150 mm. As indicated in Fig. 3.17. (a), previous propulsion tests showed that the prototype achieves optimal performance at motor speeds between 150-200 rpm. To ensure experimental consistency, the motor speed was therefore fixed at 200 rpm for all tests.

Each tube's inner surface was lined with silicone -based colon skin to more closely replicate the texture and frictional characteristics of the colonic wall. Under these controlled conditions, variations in the propulsion force were recorded as the prototype navigated through tubes of different diameters.

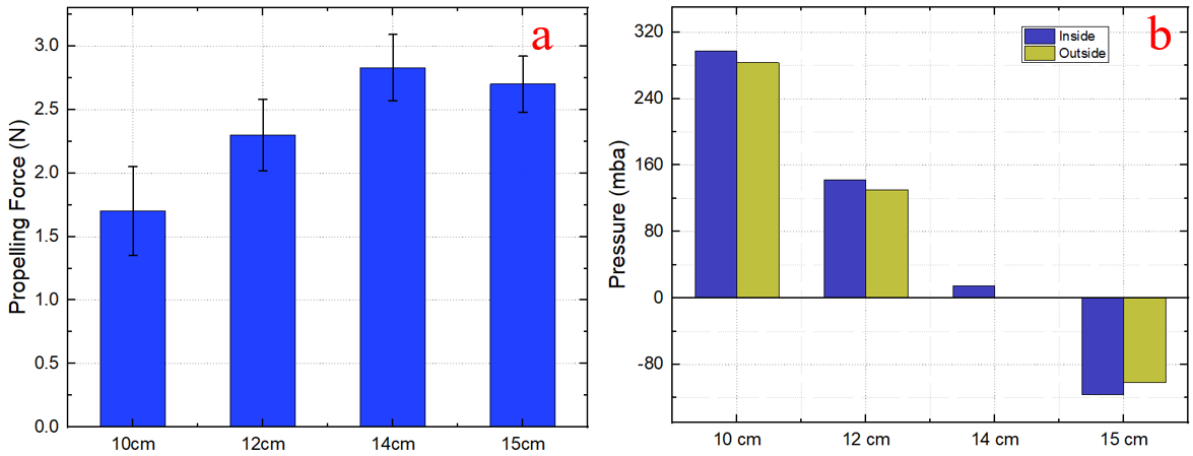


Fig. 3.17. Effect of pipe diameter on bellows pressure and propelling force in a prototype expansion mechanism. (a) Expansion mechanism in nominal state; (b) Conditioned maintenance of stable traction force.

When the prototype traversed narrower tubes, the traction force decreased with decreasing tube diameter, even though the air pressure inside the bellows remained constant. This reduction can be explained by the increased normal force exerted between the tube wall and the robot's expandable tip, which imposes additional stress on the supporting struts. Since these struts are mechanically linked to the bellows expansion mechanism, a higher normal load directly affects the bellows' performance, altering the expansion-contraction balance.

To further investigate this interaction, the internal pressure of the bellows was measured under different tube diameter conditions. In Fig. 3.17(b), the blue bars represent the average internal pressure required to maintain propulsion, while the yellow bars indicate the theoretical pressure without external constraints. A clear discrepancy between the two reflects the additional load imposed by wall contact.

This difference arises because the expandable tip must overcome both its own structural weight and the normal force exerted by the tube walls, particularly when the tube diameter is smaller than the nominal tip diameter (140 mm). As a result, higher internal pressure is required to sustain sufficient traction. Even at the nominal state (0 in Fig. 3.17), a small positive pressure is needed to support the structure.

The results reveal that propulsion force increases with expansion diameter and reaches a maximum around 14 cm, indicating an optimal contact condition. Beyond this point, further expansion provides limited improvement due to increased deformation or frictional losses. Meanwhile, the internal pressure decreases with increasing diameter and becomes negative at

larger expansions, suggesting a transition in structural–environment interaction that may affect stability. It should be noted that these results are based on averaged measurements and do not directly capture the jerky or unstable motion observed during experiments. Such behaviour is attributed to transient contact variations, intermittent slip, and dynamic deformation, which are not reflected in the steady-state measurements but are consistent with the observed trends.

### 3.6.3 Summary of experiment results

This section presented a series of experimental evaluations to validate the performance of the bellow-based expansion mechanism and the proposed robotic colonoscope prototype. Through bellow extension, prototype propulsion, and diameter adaptation experiments, the results demonstrated that the robot is capable of stable motion within a simplify simulated lumen and can effectively adjust its size to accommodate different diameters. The propulsion tests verified the theoretical predictions from Section 3.4 modelling, showing that the propulsion force and velocity change trends align well with the analytical model under varying surface conditions.

The bellows-based expansion mechanism exhibited reliable adaptability, maintaining controllable wall contact across a range of diameters from 100 to 150 mm, and its output response correlated strongly with input pressure. Furthermore, the experiments confirmed that the mechanical interaction between the expansion and propulsion subsystems plays a critical role in determining overall locomotion efficiency. Although the scaled prototype achieved consistent propulsion and stability, certain deviations from theoretical predictions were observed, mainly due to frictional losses and flexible shaft transmission effects. Undeniably, miniaturization is one of the wooden tablets for future research.

Overall, these experimental findings validate the feasibility of the proposed design concept and establish a solid foundation for further system optimization and miniaturisation in future work.

## 3.7 Limitations and future improvements

During the experiments, several phenomena were observed that revealed the limitations of the current prototype and provided valuable insight into potential improvements. Although the system was able to complete the intended tasks of propulsion and expansion, its performance in certain aspects was not fully satisfactory.

### 3.7.1 Limitations

In the mechanical transmission system, we observed that the propulsion speed did not always increase proportionally with motor speed, particularly beyond 150 rpm. This suggests that the flexible shaft has transmission loss and torsional delay. At higher rotational speeds, partial

energy loss occurs due to the elastic deformation and internal friction of the shaft, resulting in delayed response and occasional slippage between the worm gear and the tracks. More seriously, we noticed intermittent "jumping" or "jerking" behaviour, especially when the tracks transitioned between different frictional regions. This not only reduces propulsion efficiency but also leads to small irregular movements of the prototype during continuous operation.

Regarding the track system, the silicone-based tracks used in the first prototype exhibited insufficient stiffness and unstable contact with the lumen surface. During locomotion, we noticed intermittent slip behaviour, especially when the tracks transitioned between different frictional regions. The problem likely arises from the combination of low material stiffness and inconsistent friction inside the sliding grooves, which causes stick–slip motion and interrupts smooth propulsion. The silicone material, while compliant, deforms under load and cannot maintain a uniform pressure distribution along the wall, thus limiting traction consistency.

The most notable issue was identified in the bellows-based expansion mechanism. Although the bellows could achieve the designed deformation range and complete wall-press and size adjustments, we observed a noticeable delay between input pressure and structural response, as well as limited expansion range and insufficient stiffness. The reason for this behaviour is that the bellows rely on air compression and elastic recovery of soft silicone material, both of which introduce hysteresis and slow response. Moreover, the soft wall of the bellows cannot fully support the connecting struts under high load, causing deformation and reducing the precision of wall-press control. This limitation makes it difficult to achieve fine-tuned, repeatable expansion behaviour, especially under variable external constraints.

In addition, since the prototype was manufactured at a 4:1 scale, some mechanical properties such as material stiffness, fluid resistance, and contact friction do not scale linearly with size. These differences may lead to discrepancies between the experimental performance of the scaled prototype and the performance expected at the clinically relevant size. Finally, the system operates under open-loop control, which lacks real-time feedback on wall-press force and traction adjustment. This limitation reduces the robot's adaptability to dynamic changes in lumen geometry and prevents automatic correction during motion.

### 3.7.2 Future improvement

To overcome these limitations, several structural and material improvements are proposed to enhance the robot's stability, control precision, and adaptability in the next design.

First, the silicone tracks will be replaced with 3D-printed TPU tracks, which are expected to provide higher stiffness, improved wear resistance, and more consistent frictional properties. The TPU material combines flexibility with sufficient rigidity, allowing the tracks to deform appropriately while maintaining steady contact with the lumen surface. This modification is anticipated to improve both propulsion stability and the lifespan of the track system.

Second, a low-friction support structure will be added to the inner grooves of the track housing to reduce sliding resistance and prevent stick–slip motion. This enhancement is designed to provide more uniform contact between the track and its guiding surface, minimising sudden jerks or vibrations that were observed in the previous version. It is expected that this modification will allow smoother and more continuous motion under different frictional conditions.

Third, the bellows-based pneumatic actuator will be replaced with a syringe-driven hydraulic actuation mechanism. In the improved configuration, the bellows and their supporting struts will be substituted with push rods connected to small syringes filled with liquid. Using liquid as the transmission medium will minimise compressibility effects, enabling faster and more accurate control of radial deformation. This modification aims to enhance the stiffness and responsiveness of the expansion system, allowing the robot to maintain a stable diameter even under variable wall loads.

In addition, a high-torque motor will be employed to ensure sufficient driving power and reduce the effects of torsional lag in the flexible shaft. The internal layout of the prototype will be redesigned to improve mechanical rigidity and simplify the transmission path, further increasing propulsion efficiency. The incorporation of closed-loop feedback control based on pressure and force sensing is also planned to enable adaptive wall-press adjustment during locomotion. This would allow the robot to automatically maintain an optimal traction force while reducing the risk of excessive pressure on the colon wall.

Through these targeted modifications, the next-generation prototype is expected to achieve smoother propulsion, improved controllability, and enhanced adaptability to lumen geometry changes. While these improvements are proposed based on the limitations identified in the first-generation model, their effectiveness will be validated through subsequent experiments. The detailed design, modelling, and experimental evaluation of the improved prototype are presented in the following chapter.

Table 3-2 Comparison of the main limitations of the first-generation prototype and the corresponding improvement strategies

| Aspect | Observed limitation (first version prototype) | Proposed improvement | Excepted impact |
|---|---|---|---|
| Transmission | Torque loss and delayed response caused by torsional deformation of the flexible shaft, reducing propulsion efficiency at higher speeds. | Use a higher-torque motor and optimise the transmission layout to improve rigidity and reduce torsional lag. | More stable and efficient power delivery. |
| Track system | Silicone tracks too soft, resulting in deformation, uneven wall contact, and stick–slip motion during locomotion. | Replace silicone tracks with 3D-printed TPU tracks and add low-friction support structures inside the track grooves. | Smoother and more continuous propulsion with higher traction stability. |
| Expansion mechanism | Bellows expansion shows limited range, delayed response, and insufficient stiffness due to air compressibility and soft silicone walls. | Replace the pneumatic bellows with a syringe-driven hydraulic actuation system and push-rod linkage. | Faster and more precise wall-press adjustment with improved repeatability. |
| Control system | Open-loop control without real-time feedback on wall pressure or traction force. | Integrate closed-loop control with pressure and force sensing feedback. | Adaptive control and enhanced safety during operation. |
| Scaling effect | The 4:1 scaled prototype exhibits non-linear scaling in stiffness, friction, and fluid resistance, which may affect performance prediction. | Develop a dimensionless scaling model and validate performance through smaller-scale experimental prototypes. | More accurate prediction of clinical-scale performance. |

| Aspect | Observed limitation (first version prototype) | Proposed improvement | Excepted impact |
|---|---|---|---|
| Safety consideration | Excessive wall pressure may cause mucosal damage, and no automatic protection mechanism is implemented. | Add sensor-based feedback for overload detection and automatic retraction control. | Improved operational safety and clinical reliability. |

### 3.8 Summary

This chapter presented the design, fabrication, modelling, and experimental validation of the first-generation robotic colonoscope prototype. The robot was designed with a track-based propulsion mechanism and a bellows-driven wall-press adjustment system to achieve both forward locomotion and adaptive diameter control. A simplified mathematical model was developed to describe the relationships between motor torque, frictional forces, and propulsion velocity, which provided a theoretical foundation for experimental evaluation. A series of experiments were then conducted to verify the model and assess the prototype's propulsion performance, wall-press behaviour, and size adaptability within simulated colon environments.

The results demonstrated that the prototype can achieve stable propulsion and controllable expansion, confirming the feasibility of the proposed mechanical concept. However, several limitations were identified through these experiments, including energy loss in the flexible shaft, insufficient stiffness of the silicone tracks, and limited response of the pneumatic bellows expansion mechanism. These findings provided important insight into the dynamic coupling between the propulsion and wall-press systems and revealed key factors affecting motion smoothness and control precision.

Based on these analyses, a series of structural and material improvements were proposed to address the observed issues. The next chapter introduces the design and development of an improved prototype that incorporates these enhancements, focusing on increasing propulsion efficiency, improving wall-press accuracy, and enhancing overall system stability and adaptability for future clinical applications.

# 4 Design and evaluation of the prototype with hydraulic actuated expansion

## 4.1 Introduction

Building upon the findings and limitations identified in Chapter 3, this chapter presents the design and evaluation of an improved robotic colonoscope prototype. The new prototype was developed to address the key issues observed in the first prototype, including transmission inefficiency, unstable locomotion performance, and the limited responsiveness of the bellows-based expansion mechanism. Through systematic structural and material optimisation, the improved system aims to achieve more stable propulsion, enhanced adaptability to varying lumen diameters, and more precise control of wall-press force. This approach will also lay a foundation for the realization of subsequent steering function.

In this chapter, the improved prototype is described in detail, including its mechanical structure, actuation system, and control configuration. Subsequent experiments are conducted to evaluate its propulsion performance, wall-press regulation, force control and adaptive capability, with results compared against the first prototype to verify the effectiveness of the implemented improvements. The findings demonstrate the enhanced stability and controllability achieved through these design modifications and provide further insight into the potential of the proposed robotic colonoscope system for clinical applications.

## 4.2 Overall design concept

The overall structure of the improved prototype retains the same cylindrical layout and four-track configuration as the first prototype design introduced in Chapter 3, but several structural and material upgrades were implemented to enhance performance and reliability.

The design process focused on four main aspects:

- replacing the silicone tracks with 3D-printed thermoplastic polyurethane (TPU) tracks to increase stiffness and traction stability;
- introducing a low-friction support structure inside the track grooves to minimise stick–slip motion;
- substituting the pneumatic bellows with a syringe-driven hydraulic actuation mechanism to improve control precision and response speed;
- upgrading the motor and optimising the internal layout to improve power transmission efficiency.

Each of these improvements was conceived to directly resolve the shortcomings identified during experimental testing of the earlier prototype, ensuring better mechanical reliability and controllability.

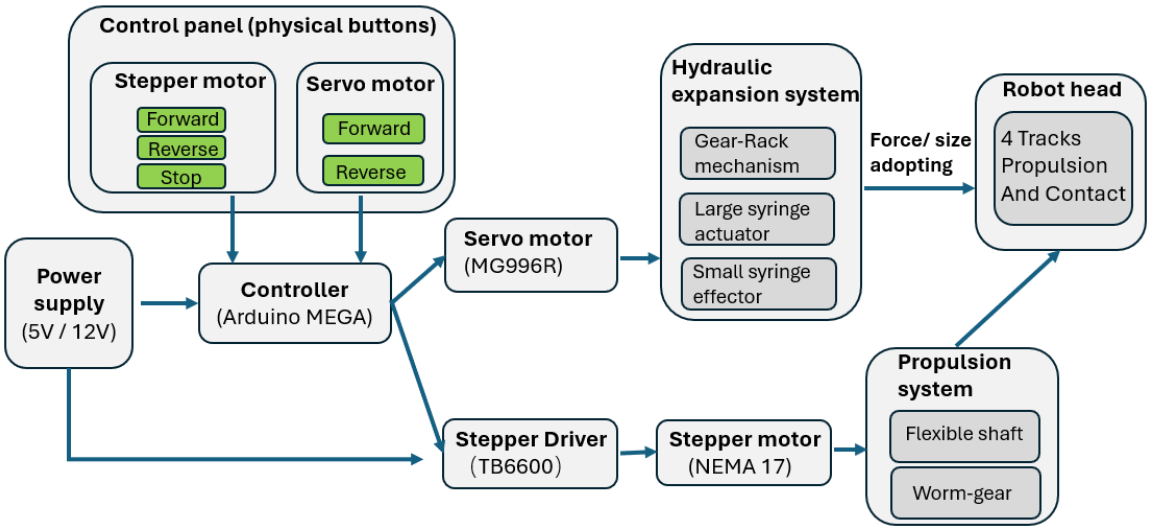


Figure 4.1. Block diagram of the control and actuation architecture of the robotic colonoscope.

The system integrates a syringe-driven hydraulic expansion mechanism and an external motor transmission mechanism for track propulsion. Figure 4.1. illustrates the control and actuation architecture of the track-based robotic colonoscope. The system consists of a power module, controller, propulsion unit, hydraulic expansion unit, and robot body. Physical buttons on the control panel enable manual operation of the stepper motor (forward, reverse, and stop) and the servo motor (forward and reverse). The controller (Arduino MEGA) sends control signals to the stepper driver (TB6600) and servo motor to actuate the propulsion and hydraulic subsystems, respectively. The propulsion system drives the four tracks through the stepper motor, flexible shaft, and worm-gear, while the hydraulic system uses a servo-driven gear-rack mechanism and a large syringe actuator to adjust the pressure in the small syringes, thereby controlling the normal force and diameter of the tracks.

Similar to the first prototype, power is supplied by an external DC motor, which is mounted outside to simplify wiring and avoid space limitations. The torque generated by the motor is transmitted through a flexible shaft to the internal drive unit of the robot. At the distal end of the flexible shaft, a worm-gear assembly converts the rotational motion into synchronous linear motion of four tracks. The four tracks are evenly distributed at 90° intervals around the circumference of the cylindrical frame and are driven at equal speed to produce forward

propulsion. Motion is achieved through tangential friction between each track and the inner wall surface.

Each track is tensioned over a pair of pulleys (rollers) and supported by a compliant base, as shown in Figure 4.2. The tracks are fabricated from thermoplastic polyurethane (TPU), a material chosen for its moderate stiffness, high wear resistance, and reliable traction on moist surfaces. According to Marechal et al. [97] polyurethane elastomers exhibit an elastic modulus of 10 - 30 MPa and Shore A hardness of 70-90, which are an order of magnitude higher than those of silicone rubbers (0.05-1 MPa, Shore A 20-40). Experimental wear tests have also shown that TPU has wear rates of 1- $4 \times 10^{-6}\ mm^3/N \cdot m$ and a friction coefficient around 0.4, compared with $10^{-5}$- $10^{-4}\ mm^3/N \cdot m$ reported in [98]. These quantitative differences support the improved durability and traction stability observed in the redesigned tracks. The robot's body frame and connecting mounts are printed using high-strength polymer materials (PLA and PETG), ensuring structural rigidity while keeping the total mass low. The compact and symmetric arrangement of the four tracks ensures uniform wall contact and balanced normal forces during propulsion.

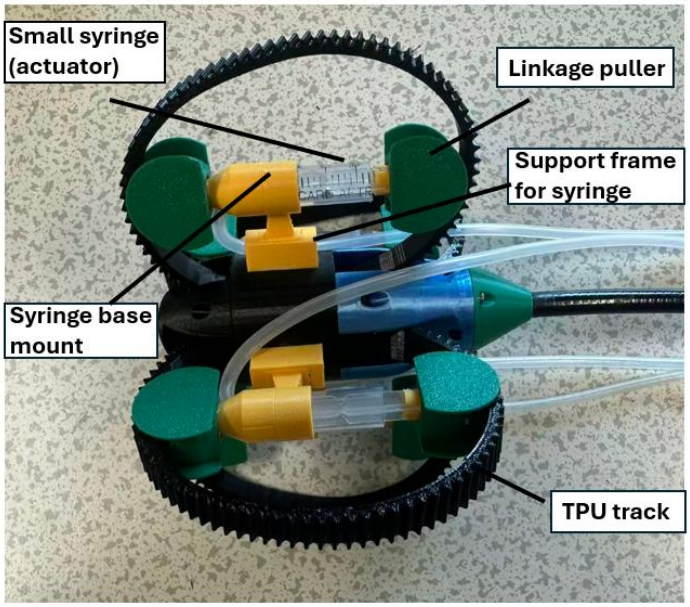


Figure 4.2. Detail of robotic colonoscope head.

To enable adaptive wall-press adjustment, the pneumatic bellows used in the first prototype have been replaced with a syringe-based hydraulic expansion module. This module consists of four large external syringes connected to four small syringes embedded behind each track via sealed fluid lines. The hydraulic actuation of each small syringe occurs in the axial direction, parallel to the robot's longitudinal axis. Through the geometric constraint of the syringe holder

and the supporting linkage beneath each track, this axial motion is transformed into a radial displacement of the track module. As a result, advancing the plunger increases the radial expansion of the corresponding track, enhancing wall contact, whereas retraction leads to contraction and traction reduction. Conversely, retracting the external syringe reduces the internal pressure and allows the tracks to retract slightly. Through this mechanism, the normal contact force between the track and the wall can be finely adjusted, allowing the robot to adapt to variations in the internal diameter while maintaining continuous traction force.

The hydraulic syringe system and mechanical transmission are fully decoupled: the motor provides steady kinematic motion, while the hydraulic network adjusts size-adapting conditions independently. This configuration improves controllability and repeatability of wall contact, reduces slippage, and enhances propulsion efficiency.

## 4.3 Structural and functional improvements

### 4.3.1 Hydraulic expansion mechanism

In the first prototype, size adjustment relied on pneumatic bellows, whose air medium is highly compressible (bulk modulus is almost 0.1 MPa). This inherent property led to a slow and nonlinear expansion response. In the improved design, the pneumatic actuator was replaced by a syringe-driven hydraulic system that transmits pressure through water, an incompressible medium with a bulk modulus approximately four orders of magnitude greater than that of air (almost 2200 MPa). This configuration allows faster pressure transmission and more predictable volume control, thereby improving actuation precision and repeatability.

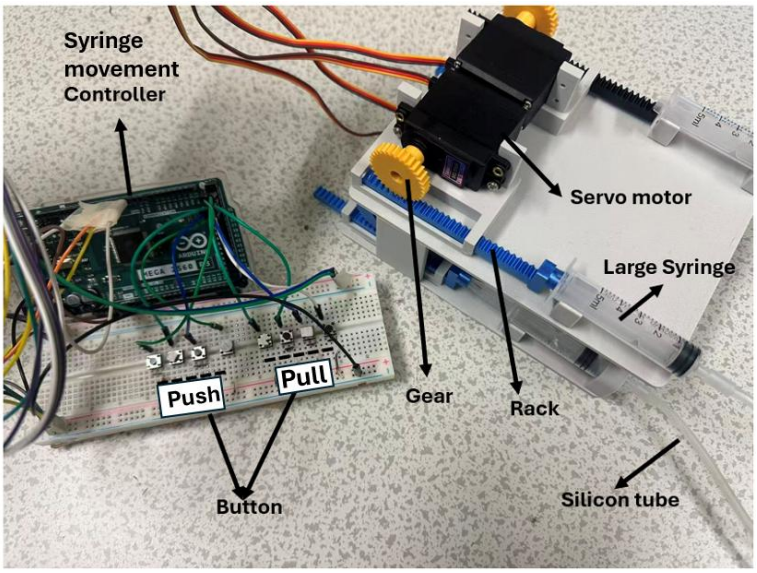


Figure 4.3. Actual setup of syringe-driven hydraulic expansion system.

Each large syringe in the hydraulic expansion system is driven by a dedicated servo motor (MG996R). The MG996R is a high-torque metal-gear servo capable of delivering approximately 1 $N \cdot m$ at 6 V, providing sufficient force to actuate the syringe plunger through a lead-screw transmission. A total of four servo motors are installed externally, corresponding to the four large syringes that control the four embedded small syringes on the robot. Each servo motor is operated via two manual push buttons for forward and backward motion of the syringe plunger, with the signals managed by an Arduino MEGA controller. At the output shaft of the servo motor, a circular gear is mounted, which meshes with a linear rack connected to the plunger of the large syringe. When the "push" button is pressed, the servo rotates in the forward direction, driving the gear-rack mechanism to advance the syringe plunger and inject fluid into the silicone tube. The incompressible liquid is then transmitted through the sealed tubing to the corresponding small syringe inside the robot, generating radial expansion at the track support. Pressing the "pull" button reverses the servo rotation, causing the plunger to retract and drawing the fluid back, which in turn allows the small syringe to retract and reduce wall pressure. This mechanism realises a precise and repeatable hydraulic actuation process for wall-press regulation and size-adjusting, synchronously.

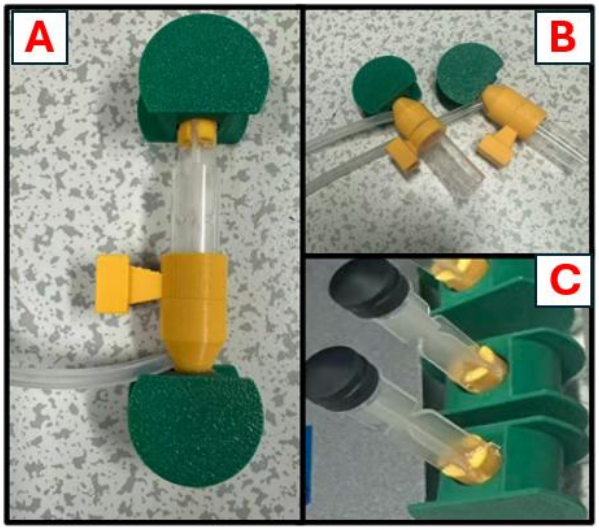


Figure 4.4. Syringe-based hydraulic expansion module. (A) Overall structure of a single expansion module, consisting of one syringe, a base mount, and two puller. (B) Detailed view of both ends showing the syringe holder and puller connector components. (C) Mounted configuration where the syringe modules are installed beneath the track supports to generate radial expansion.

The syringes used in the hydraulic system were selected as a low-cost and easily accessible solution. Each syringe was manually trimmed with a precision knife to the required length,

allowing it to fit within the available space and meet the designed displacement range. The syringes are interconnected by silicone tubes with an inner diameter of 3 mm, which are both flexible and durable. The tube has good flexibility and durability, and is fixedly arranged along the outer side of the flexible shaft, and does not disrupt it's the torsion and bending

The gears and racks employed in the servo-driven actuation mechanism were fabricated by 3D printing using PLA material. This manufacturing approach enables rapid prototyping, dimensional consistency, and low production cost, while providing sufficient mechanical strength for transmitting the actuation force required by the syringe plungers. The gear-rack mechanism has a module of 1 mm, with a pitch diameter of 30 mm and 30 teeth. Thus, the transmission ratio is $i = 15$ mm/rad, meaning the rack advances 15 mm for each radian of gear rotation. A full revolution (360°) of the gear corresponds to approximately 94.2 mm of linear displacement of the rack.

### 4.3.2 TPU-Based Tracks

Previous studies have proposed multi-layer track designs, in which different silicone rubbers were used to provide specific stiffness and friction properties for each region of the track [23]. These designs typically consisted of a soft, high-friction surface layer combined with stiffer, low-friction structural layers to balance traction, compliance, and wear resistance. The underlying concept is that appropriate hardness and friction characteristics are required across the track to maintain wall adhesion while minimizing deformation during motion. In this work, a simplified approach was adopted by employing a single-material thermoplastic polyurethane (TPU) track, which inherently offers moderate stiffness, elasticity, and abrasion resistance without the need for complex multi-material fabrication.

This study compared three tread geometries: trapezoidal, triangular, and hybrid, each exhibiting distinct structural and functional characteristics.

- The trapezoidal profile, used in the first prototype silicone track, features a wide crown and shallow flanks, providing stable contact but low local pressure, resulting in limited traction under lubricated conditions. It is easy to manufacture and distributes stress evenly, but its stiffness and grip are insufficient.
- The triangular profile has sharp tips and steep flanks, forming a small contact area with high local pressure that enhances traction and fluid drainage. However, the sharp apex causes stress concentration and wear, is difficult to manufacture precisely, and tends to deform over time.

- The hybrid profile, adopted in the improved TPU track, combines the advantages of both geometries. It retains a narrow flat crown and rounded apex while increasing the flank angle to improve traction and drainage, reducing stress concentration and improving print reliability. This design achieves a balance between traction, wear resistance, and manufacturability, making it suitable for locomotion in narrow and lubricated environments.

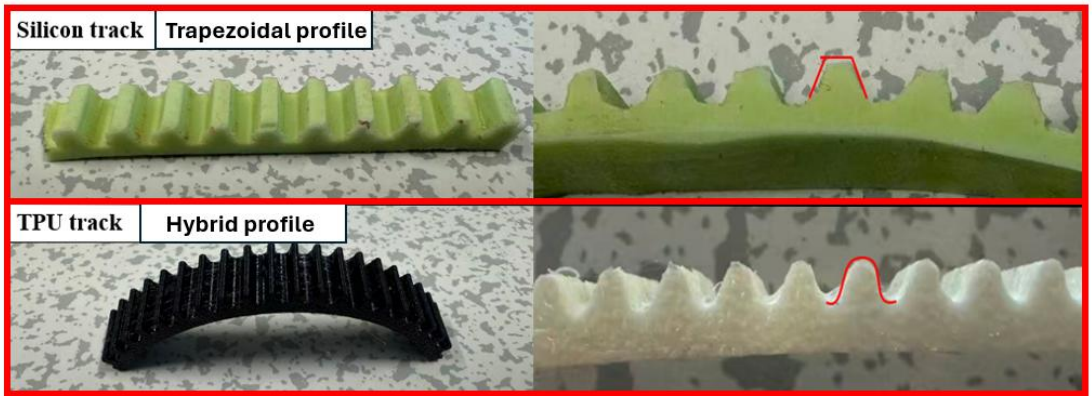


Figure 4.5. Comparison of track materials and cross-sectional tooth profiles between the first prototype (silicone, upper) and improved (TPU, lower) designs. The black and white TPU samples differ only in colour and are used to highlight the details.

The first prototype employed a silicone track with a trapezoidal tooth profile featuring a flat crown and a relatively small flank angle. This configuration provided limited stiffness and insufficient traction under compression, particularly on lubricated surfaces. In the improved prototype, the track was fabricated from thermoplastic polyurethane (TPU) and redesigned with a hybrid tooth profile that lies between trapezoidal and triangular geometries.

The TPU tracks are fabricated using precision 3D printing to achieve accurate dimensions and consistent surface patterns. The track hardness and texture are designed to maintain sufficient flexibility for conformal wall contact while providing enhanced grip. Each track is assembled on a pair of miniature pulleys, forming a closed loop that runs around its support frame. Compared with silicone, the TPU tracks maintain dimensional stability over long-term use, preventing slippage and deformation that could lead to propulsion inconsistency.

In addition, the new track mounting structure allows easy removal and replacement without disturbing the internal transmission, simplifying maintenance and ensuring experimental repeatability across multiple test cycles.

### 4.3.3 Structural reinforcement and transmission optimisation

In the improved prototype, the overall structural design was comprehensively optimised to enhance mechanical robustness, reduce internal friction, and improve experimental usability. The appearance of the robot was redesigned with smooth, rounded contours instead of the sharp-edged structure used in the first prototype. This aesthetic and functional refinement reduces the sense of invasiveness, making the form factor more acceptable for potential medical applications, while also eliminating unnecessary protrusions that could generate friction or interfere with the surrounding wall during motion.

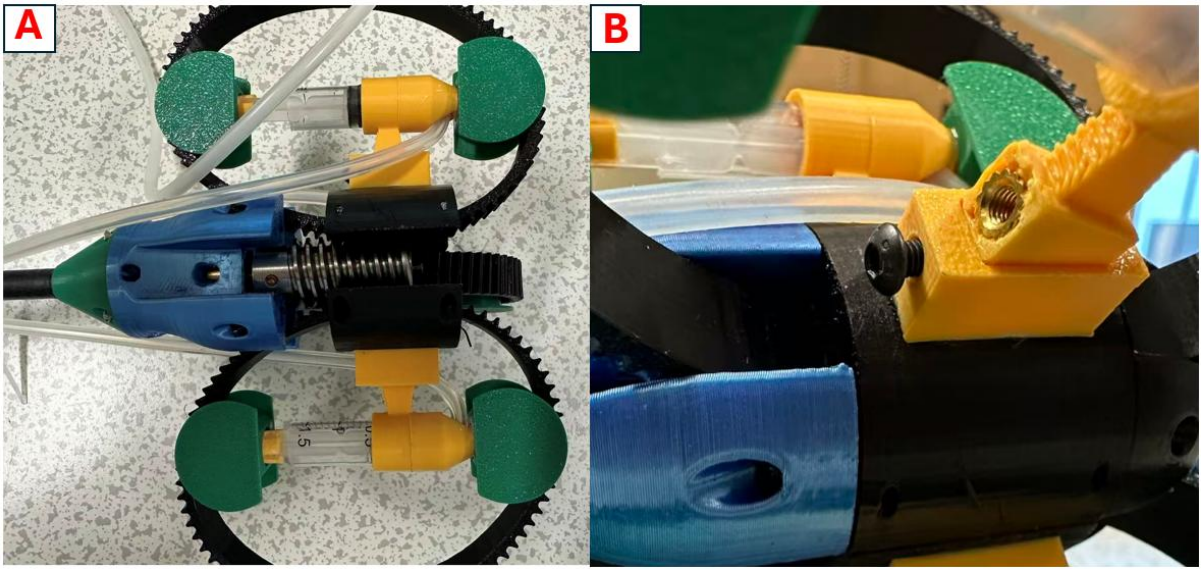


Figure 4.6. Quick-release mechanism for track replacement in the improved robotic colonoscope. (A) Quick-release interface of the track module, allowing rapid removal and replacement without disassembling the transmission system, (B) Quick-release mount of the hydraulic expansion mechanism, enabling convenient installation and adjustment of the syringe holder during experiments.

To further improve mechanical coordination, the geometric relationship between the tracks and the main body was optimised to minimise motion interference. The clearance between moving and stationary components was carefully adjusted, resulting in smoother track operation and lower energy loss. A quick-release mechanism was incorporated into the improved design to simplify the assembly and replacement of the track modules, as shown in Figure 4.6. (A). The mechanism uses screw-based connectors with brass threaded inserts embedded in the 3D-printed housing, allowing each track to be detached or reinstalled without dismantling the internal transmission system, as shown Figure 4.6. (B). This feature significantly simplifies

maintenance, shortens the preparation time between experiments, and enhances the repeatability of testing.

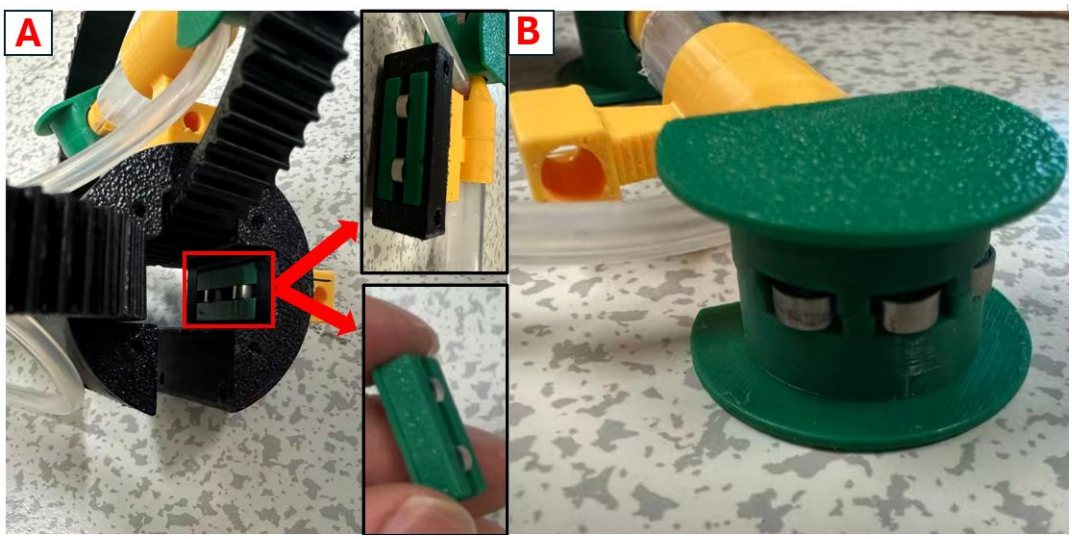


Figure 4.7. Bearing-based sliding and support structures integrated in the improved prototype. (A) Sliding support unit installed beneath the track, consisting of two miniature bearings embedded in a 3D-printed housing to reduce internal friction between the track and the guiding wall. (B) Sliding support unit installed on the roller of the track.

Each track was equipped with a sliding support device, adapted from miniature ball bearings, to reduce friction between the track and the inner guiding surface of the robot. The same bearing-based mechanism was also integrated into the hydraulic expansion system, where the roller were fitted with bearing sleeves to minimise sliding resistance during actuation. These additions effectively reduce internal mechanical friction, improving transmission efficiency and ensuring smoother wall-press adjustments.

In addition, several reinforcements were introduced to the drive and transmission systems. The 3D-printed polymer worm gear used previously was replaced with a metallic worm gear, which provides higher strength, better wear resistance, and more stable torque transmission. To further improve rotational stability, bearings were added to both ends of the flexible shaft, preventing vibration and misalignment caused by torsional deformation. The robot body was divided into three modular sections connected by screws, allowing convenient assembly, alignment, and internal maintenance. This modular configuration facilitates independent replacement of components such as the drive or hydraulic units, improving both structural integrity and usability.

Furthermore, the width of each track was increased from 7.5 mm to 12 mm, expanding the effective contact area between the track and the colon-like wall. The wider track distributes normal pressure more evenly, providing more stable traction and reducing the likelihood of local slippage.

Together, these improvements create a robot that is not only mechanically stronger and more efficient but also easier to maintain and better suited for repeated experimental trials. The combination of structural refinement, bearing-based friction reduction, and modular design greatly enhances the overall robustness, controllability, and reliability of the robotic platform.

## 4.4 Mathematical modelling of the hydraulic expansion system

Since the mechanical transmission architecture of the improved prototype remains identical to that of the first prototype, which consists of an externally mounted motor, a flexible shaft, and a worm gear driven four-track system, the corresponding formulations described in Chapter 3 are directly applicable here. Therefore, the modelling of the transmission subsystem is not repeated in this chapter. Instead, the focus is placed on the hydraulic expansion mechanism, which represents the main improvement introduced in the second prototype.

The following establishes the mathematical model of the syringe-based hydraulic system, describing the relationship between input displacement, pressure transmission, and output deformation at the small syringes. This model forms the basis for analysing the dynamic response, pressure losses, and volumetric efficiency of the hydraulic actuation during the wall-press regulation process.

### 4.4.1 Location of syringe-actuator

The placement of the syringe actuator plays a key role in determining the hydraulic system's responsiveness and structural compactness. This section explains the design rationale and positioning scheme.

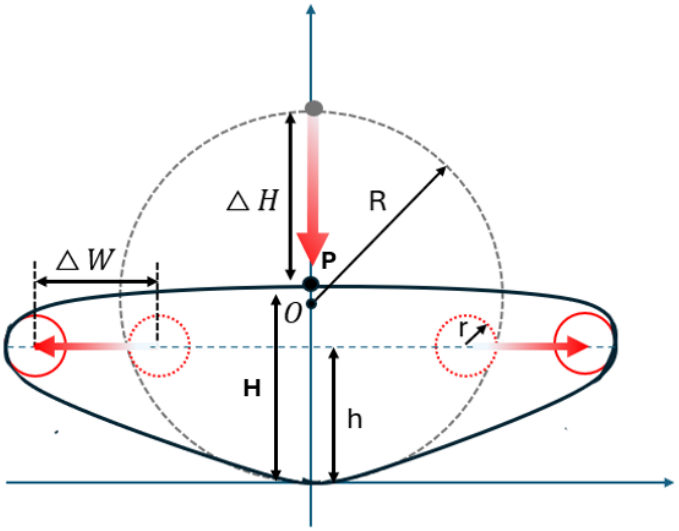


Figure 4.8. The analysis diagram of syringe's location.

Suppose that R is the radius of track, P is a point with a diameter in the vertical direction and moves in the vertical direction, and its distance from the bottom of the belt is H. The horizontal distance W of P point from one side of the track is：

$$W=\sqrt{R^2-(h-R)^2} \tag{1}$$

Now, two rollers with radius $r$ spread the crawler outward from the inside of the crawler. As shown in Figure X, the deformation of the crawler increases with the movement of the rollers in the horizontal direction. In which the variation of the highest point：

$$\triangle H = 2R - h - r \tag{2}$$

At this time, the corresponding width of the two rollers in the horizontal direction is:

$$W = 2\left[\sqrt{R^2-(h-R)^2}+r\right] \tag{3}$$

So, the increase in the horizontal direction is：

$$\triangle W = 2\left[\sqrt{R^2-(h-R)^2}+r-R\right] \tag{4}$$

In order to ensure the validity of the formula，

$$(h-R)^2 \leq R^2 \tag{5}$$

$$0 \leq h \leq 2R \tag{6}$$

That is, the rollers must be within the upper and lower range of the track.

In this case, the spread width at a given height is only approximated, while the actual curvature of the track surface is neglected. The size and hydraulic stroke of the central small syringe must be determined carefully, as the syringe's length, stroke, and installation height directly influence the efficiency of the expansion mechanism. By establishing a mathematical model, the optimal position and dimensions of the syringe can be derived. Geometrically, the problem can be simplified to the relationship between two intersecting circles.

The formula for calculating the horizontal stroke of the small syringe $x$ is:

$$x = \sqrt{(R-r)^2 - (R-h)^2} \tag{7}$$

To ensure that the small syringe reaches the predetermined position, the following conditions must be satisfied:

$$x_f + S_{Max} \geq x \tag{8}$$

Table 4-1 Definition of symbols related to the location of syringe.

| Symbol name | Symbol meaning |
|---|---|
| R | Radius of the track |
| r | Radius of the roller |
| h | Distance from the bottom |
| $x$ | In order to jack up the belt at h, the horizontal distance that the top block should be pushed out. |
| $S_{Max}$ | Maximum push-out stroke of hydraulic rod |
| $x_f$ | Horizontal distance between the rear end (fixed end) of the hydraulic rod and the centre of the great circle |

4.4.2 Displacement and force amplification in the hydraulic system

According to the basic geometric formula of circular area :

$$A_1 = \frac{\pi D_1^2}{4} \tag{9}$$

$$A_2 = \frac{\pi D_2^2}{4} \tag{10}$$

Where $A_1$ and $A_2$ are the cross-sectional areas of the large and small syringes, respectively, and $D_1$ and $D_2$ denote their corresponding inner diameters.

Based on Pascal's law, the pressure in a closed liquid system is transmitted uniformly (The formula is applicable to: when ignoring the height difference of liquid column, low-speed static pressure and local pressure loss, the static pressure is equal everywhere in the communication cavity.) :

$$P_1 = P_2 = \frac{F_1}{A_1} = \frac{F_2}{A_2} \tag{11}$$

Where $P_1$ and $P_2$ are the pressures in the large and small syringes, $F_1$ and $F_2$ are the corresponding output forces.

From this relationship, the force amplification ratio can be expressed as:

$$\frac{F_1}{F_2} = \frac{A_1}{A_2} = (\frac{D_1}{D_2})^2 \tag{12}$$

4.4.3 Theoretical modelling of force transmission in hydraulic expansion

Ignoring the normal decomposition loss caused by tooth surface friction and pressure angle, the ideal upper limit of driving force transmitted to the piston of large syringe tube can be obtained, the thrust of large syringe tube $F_B$ is:

$$F_B = \frac{\tau}{r} \tag{13}$$

Where $r$ is the radius of the motor output gear, $\tau$ is the toque of servo motor.

According to the conservation of volume, the volume of liquid displaced by the large syringe is equal to that advanced by the small syringe, which can be expressed as:

$$V = A \times S \tag{14}$$

$$\frac{S_2}{S_1} = \frac{A_1}{A_2} = (\frac{D_1}{D_2})^2 \tag{15}$$

Where $S_1$ and $S_2$ denote the piston displacements of the large and small syringes, respectively.

A geometric scaling factor of approximately four is adopted to facilitate prototyping and experimental validation. Accordingly, the design of the expansion mechanism is configured to accommodate the scaled diameter range while preserving the relative variation in lumen size.

This ensures that the mechanical behaviour observed in the experiments remains representative of the intended physiological conditions.

The transmission characteristics of the hydraulic system play a critical role in determining the effectiveness of the expansion mechanism. As shown in Eq. (12), the force amplification ratio is governed by the area ratio between the large and small syringes, i.e., $(\frac{D_1}{D_2})^2$. A larger ratio increases the output force at the small syringe, which is beneficial for generating sufficient normal contact force against the surrounding wall. However, this comes at the expense of reduced displacement, limiting the achievable expansion range.

Conversely, a smaller transmission ratio allows for larger output displacement but reduces the available force, potentially resulting in insufficient traction during locomotion. Therefore, the dimensions of the syringes and the corresponding expansion mechanism are selected to balance these competing requirements, ensuring that the system can achieve both adequate radial expansion and sufficient normal force across the scaled lumen diameter range.

This design consideration also extends to the geometric configuration of the expansion structure, including the scissor mechanism and track deformation behaviour, which are selected to ensure compatibility with the scaled anatomical constraints while maintaining effective force transmission and structural stability.

Considering the hydraulic resistance and frictional losses during fluid transmission, the actual output force, $F_{out}$ can be expressed as:

$$F_{out} = F - F_f \tag{16}$$

Where $F$ is the theoretical output force derived from the pressure transmission, and $F_f$ represents the total frictional and viscous losses within the tubing and syringe seals.

The main sources of energy loss in the hydraulic system include:

(1) mechanical friction within the transmission mechanism,

(2) frictional resistance between the syringe piston and barrel, and

(3) viscous losses caused by the internal flow of the liquid.

The total frictional force acting on each component can be expressed as:

$$F_{fi} = F_{ci} + b_i v_i \tag{17}$$

Where $F_{c,i}$ is the Coulomb friction force, $b_i$ is the viscous friction coefficient, $v_i$ represents the relative velocity of the fluid or moving part. The subscript $i$ corresponds to the respective component in the system, where G, B, and S to correspond to the gear, large syringe, and small syringe.

Considering these frictional losses, the effective thrust of the large syringe can be expressed as:

$$F_{B,eff} = \frac{\tau}{r} - F_{f,G} - F_{f,B} \tag{18}$$

where $\tau$ is the servo motor torque, $r$ is the pitch radius of the gear, $F_{f,G}$ is the frictional loss in the gear transmission, and $F_{f,B}$ is the frictional loss within the large syringe. This corrected force $F_{B,\text{eff}}$ represents the actual driving thrust transmitted to the hydraulic fluid.

The actual output force of the small syringe, after accounting for hydraulic transmission and local frictional losses, can be expressed as:

$$F_{S,out} = \left(\frac{\tau}{r} - F_{f,G} - F_{f,B}\right)\frac{A_2}{A_1} - F_{f,S} \tag{19}$$

When the liquid flows through the connecting tube, viscous friction causes a pressure drop, which further reduces the transmitted force. The pressure loss due to fluid motion in the pipe can be calculated as:

$$\Delta P = R_h Q = \frac{8\mu LQ}{\pi R_{pipe}^4} \tag{20}$$

Where $R_h$ is the hydraulic resistance of the tube, $L$ and $R_{\text{pipe}}$ are the length and radius of the connecting pipe, $\mu$ is the dynamic viscosity of the liquid, and $Q$ is the volumetric flow rate.

$$F_{S,out} = \frac{A_2}{A_1}\frac{\tau}{r} - F_{C,eq} - b_{eq}v_B \tag{21}$$

Where $F_{C,\text{eq}}$ and $b_{\text{eq}}$ represent the equivalent Coulomb and viscous friction terms of the entire system, respectively, and $v_B$ is the velocity of the large syringe piston.

where the equivalent Coulomb friction term and the equivalent viscous coefficient can be expressed as:

$$F_{C,eq} = \frac{A_2}{A_1}\left(F_{C,G} + F_{C,B}\right) + F_{C,S} \tag{22}$$

$$b_{eq} = \frac{A_2}{A_1}(b_G + b_B) + \frac{A_1}{A_2}b_S + b_H \tag{23}$$

$$b_H = R_h A_1 A_2 \tag{24}$$

where $F_{C,G}$, $F_{C,B}$, and $F_{C,S}$ are the Coulomb friction forces of the gear transmission, large syringe, and small syringe, respectively; $b_G$, $b_B$, and $b_S$ represent their corresponding viscous friction coefficients. The term $b_H$ denotes the hydraulic damping coefficient caused by the flow resistance in the connecting pipe, which depends on the fluid resistance $R_h$ and the effective cross-sectional areas $A_1$and $A_2$.

This formulation integrates both mechanical and fluidic losses into unified equivalent parameters, providing a simplified representation of the system's overall energy dissipation characteristics.

Table 4-2 Symbols and meanings related to force transmission in hydraulic expansion.

| Name | Meaning |
|---|---|
| $F_c$ | The Coulomb friction force |
| $b$ | The viscous friction coefficient |
| $v$ | The flow rate of the liquid |
| $\tau$ | Motor toque |
| $F_{B,eff}$ | The effective thrust of the large syringe |
| $F_{S,out}$ | The actual output of the small syringe |
| $\Delta P$ | Pressure drop |
| Q | Volumetric flow rate |
| $\mu$ | Dynamic viscosity |
| $R_h$ | Liquid resistance |
| $F_{C,eq}$ | Equivalent Coulomb friction force |
| $b_{eq}$ | Equivalent viscous damping coefficient |

| | |
|---|---|
| $b_H$ | Hydraulic viscous damping coefficient |

In this section, the mathematical model of the syringe based hydraulic expansion system was established to characterise the pressure transmission and deformation behaviour of the improved robotic colonoscope. The modelling process described the relationship between the input displacement of the large syringe, the fluid pressure, friction and viscosity, etc. in the connecting tube, and the resulting expansion of the small syringe within the robot body. The analytical framework provides a quantitative basis for evaluating system parameters such as response time, volumetric efficiency, and pressure loss.

## 4.5 Experimental evaluation and comparative analysis

This section presents both the comparative tests between the two robotic prototypes and the detailed characterisation of the newly introduced syringe based hydraulic system. A series of dedicated tests were performed on the hydraulic subsystem to investigate its pressure transmission characteristics, response delay, and force output behaviour.. In addition, the comparative experiments were conducted to evaluate the overall locomotion performance of the improved prototype (second) relative to the first generation under identical test conditions These experiments provide a deeper understanding of the hydraulic actuation efficiency and validate the mathematical model established in Chapter 4.4.

### 4.5.1 Characterisation of the hydraulic system

To evaluate whether the hydraulic actuator can provide sufficient force to deform the track and achieve detachment from the contact surface, a finite element model of the track segment was established in ANSYS 2023 R2. The simulation determined the minimum force required to initiate the intended deformation. The results of the data provide a great guiding significance for the subsequent design.

#### 4.5.1.1 Prerequisite experiments

To improve computational efficiency and focus on the primary deformation mode, the finite element model of the track segment was simplified. The belt was represented by its load-bearing section only, with surface textures and fastening details omitted. The material was modelled as homogeneous and isotropic TPU, and the surrounding structures were replaced with idealized boundary conditions replicating the actual constraints. These simplifications

were justified as the neglected features have negligible influence on the overall stiffness and the minimum force required for the intended deformation.

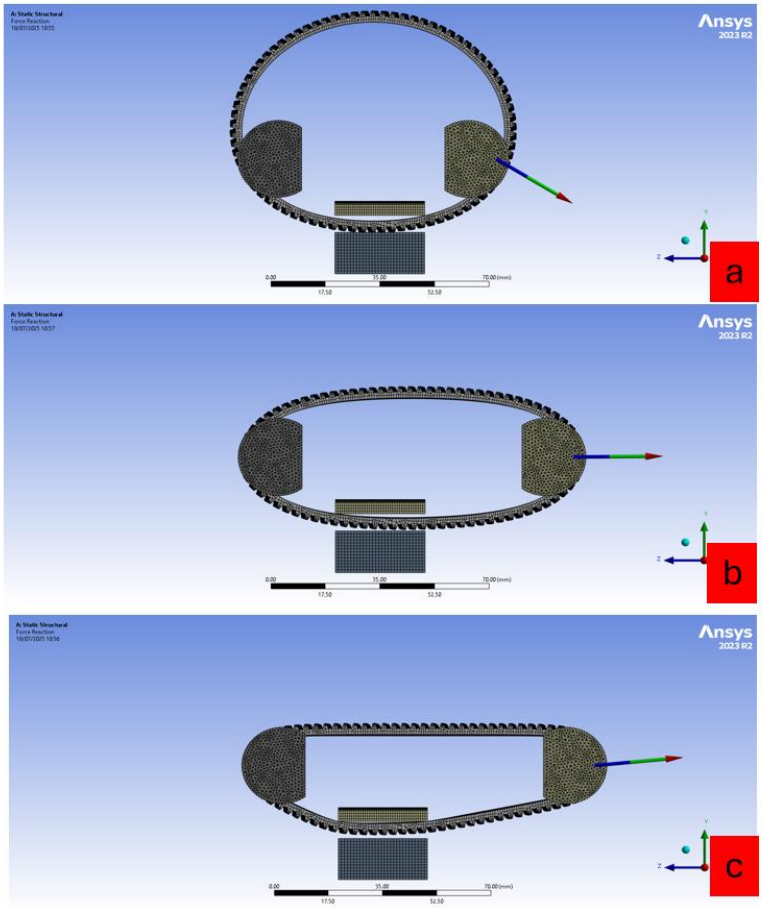


Figure 4.9. Finite element analysis (FEA) of the TPU track deformation under different expansion states. (a) Initial state before expansion; (b) Moderate expansion under partial hydraulic actuation; (c) Maximum expansion corresponding to the full stroke of the small syringe.

As shown in Figure 4. 10, the left axis represents the radial expansion displacement (mm), while the right axis indicates the total radial force magnitude (N). Both quantities increase nonlinearly with the syringe stroke, demonstrating the nonlinear amplification behaviour of the hydraulic system.

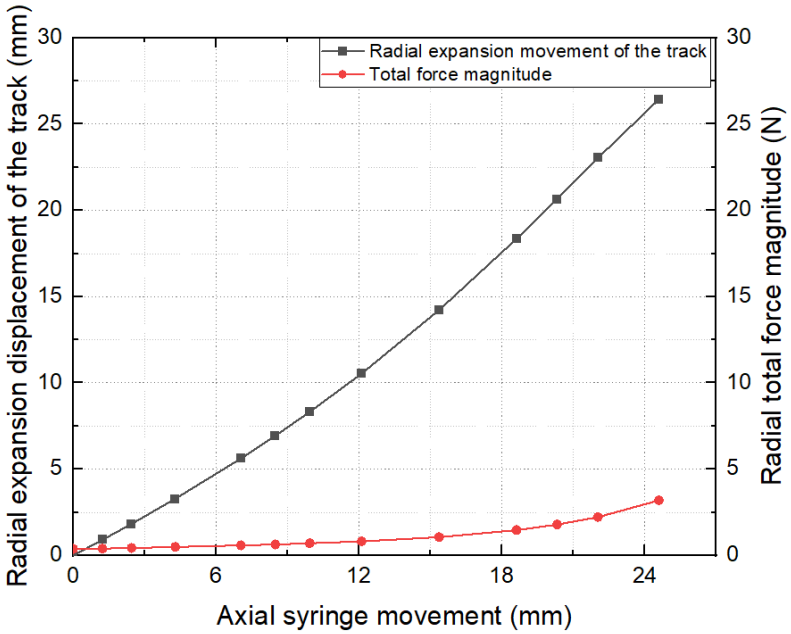


Figure 4.10. Relationship between axial syringe displacement, radial expansion of the track, and generated radial force.

The simulation results indicated that, during the stroke of the small syringe from 0 mm to 25 mm, the maximum force exerted on the track was approximately 3.2 N, resulting in a peak vertical displacement of about 26.5 mm. This means that to ensure that the track can deform to a predetermined position, the small syringe needs to provide at least 3.2 N force to maintain the balance of the track, as shown in Figure 4.10..

4.5.1.2 Syringe force output test

The experimental setup consisted of a rigid acrylic base, on which a custom 3D-printed PLA fixture was mounted to secure the force sensor (MiniONE, Bota, Switzerland) and connect it to the small syringe. The small syringe, with an inner diameter of 4.2 mm, was hydraulically coupled to the large syringe (inner diameter 12 mm). Both syringes were connected by a silicone tube (inner diameter 3 mm, outer diameter 5 mm, length 150 mm) filled with water as the working fluid. The large syringe was mechanically driven by an MG996R servo motor through a 3D-printed gear-rack mechanism, which converted the rotational motion of the motor into a linear displacement of the syringe plunger. The hydraulic pressure generated by the large syringe was transmitted to the small syringe, producing an output force that was continuously recorded by the high-sensitivity sensor. All components were rigidly assembled using bolts to ensure structural stability and accurate force measurement throughout the experiment.

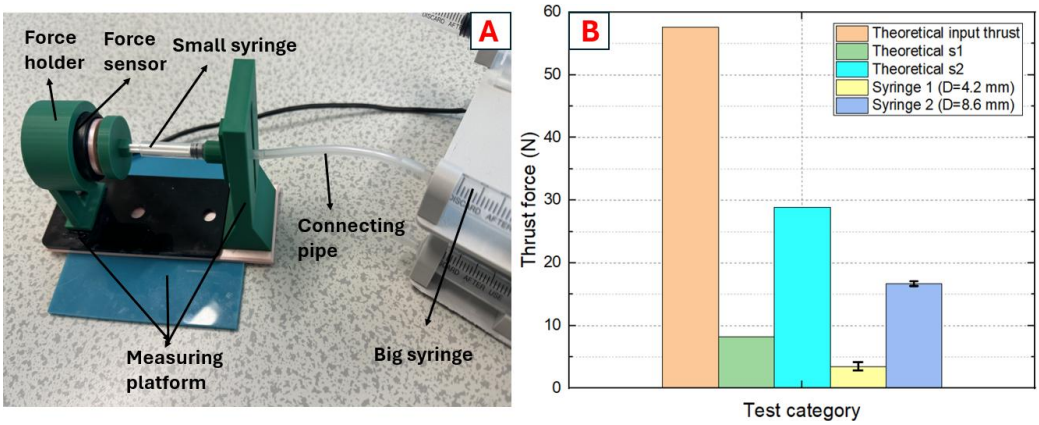


Figure 4.11. Experimental setup and comparative results of hydraulic force amplification using different syringe combinations.

As shown in Figure 4. 11, the experimental setup (A) consists of a large syringe, a small syringe, a connecting pipe, and a Mini-ONE force sensor. The results (B) demonstrate that increasing the diameter of the small syringe from 4.2 mm to 8.6 mm significantly enhances the output thrust, consistent with the theoretical predictions.

In the preliminary tests, a commercially available syringe with an inner diameter of 4.6 mm was used as the small syringe. Based on the hydraulic model, the theoretical output force under a driving pressure of 0.2 MPa was approximately 3.2 N, which is the minimum required to deform the track. The measured force in this configuration reached 3.4 N, leaving only a narrow safety margin for reliable operation. To enhance actuation performance, a syringe with an inner diameter of 8.6 mm was subsequently adopted, providing a significantly larger effective area and thus higher output force. Under the same pressure range (0 - 0.25 MPa), the measured average output increased to 16.7 N, fully satisfying the expansion requirement of the track. Therefore, all subsequent experiments were conducted using the 8.6 mm syringe. The deviation between theoretical and measured forces is mainly due to hydraulic transmission losses, including tube compliance, fluid resistance, and minor leakage in the system.

The two syringes selected in this experiment are $D_1 = 12mm$, $D_2 = 8.6mm$ . The key parameter is the cross-sectional area ratio of two syringes, which determines the force magnification and stroke ratio. For example, if the cross-sectional area of a large syringe tube is almost 2 times that of a small syringe, the output force is increased by 2 times, but the stroke is almost shortened to 1/2.

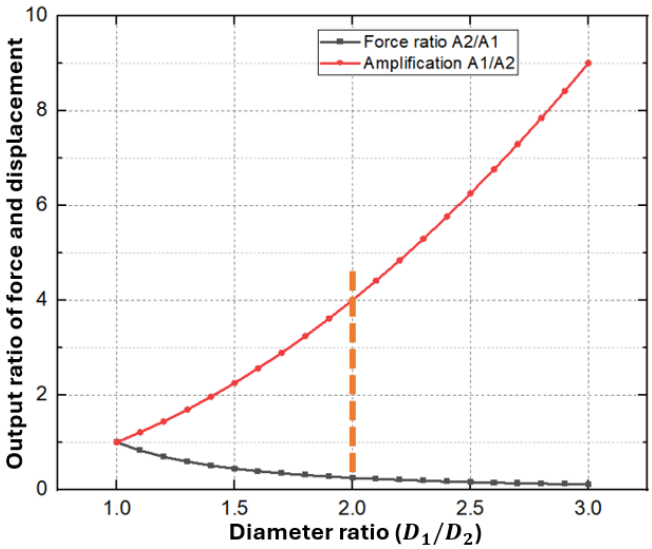


Fig. 4.12. Theoretical relationship between syringe diameter ratio and output amplification of force and displacement.

4.5.1.3 Response delay measurement

During the hydraulic actuation tests, it was observed that the motion of the small syringe exhibited a short response delay following the initiation of movement in the large syringe plunger. This phenomenon is likely attributable to factors such as fluid compressibility, elastic deformation of the tubing, mechanical clearance in the connectors, and viscous flow resistance. Such a delay could affect the actuation responsiveness and control precision of the overall system, especially in dynamic operating conditions.

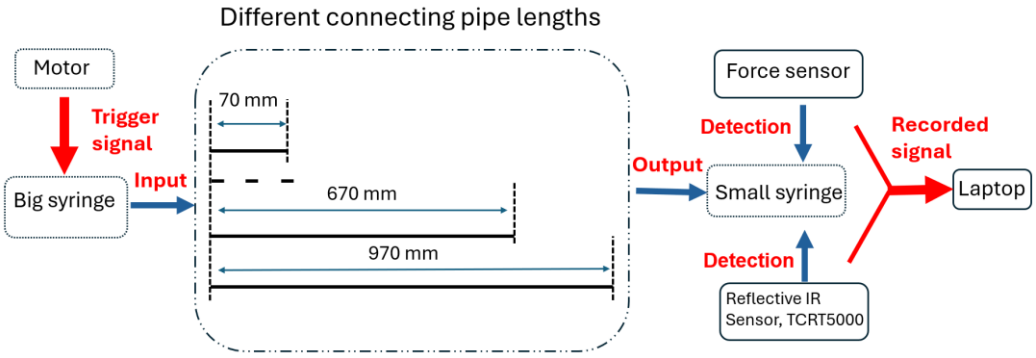


Fig. 4.13. Schematic diagram of small syringe response experiment.

To quantitatively evaluate this delay, a dedicated measurement experiment was conducted. The experimental platform consisted of the previously described setup, in which the large syringe was driven by an MG996R servo motor through a gear-rack mechanism, while the small syringe was connected to a high-sensitivity force sensor. An optical TCRT5000 sensor was positioned to detect the initial motion of the large syringe plunger, while the force sensor

simultaneously recorded the onset of force generation at the small syringe. As the plunger moved, the TCRT 5000 reflected infrared intensity changed proportionally to its position, allowing for precise detection of the initial motion. Both sensors were connected to a microcontroller for synchronous data acquisition at a fixed sampling frequency. The delay time was calculated as the temporal difference between the plunger movement detection signal and the corresponding force signal from the small syringe. All components were rigidly mounted on an acrylic base to minimise structural vibration and ensure repeatable measurements.

In order to investigate the effect of tubing length on the system's response time, six different connecting tube lengths were tested: 70 mm, 170 mm, 270 mm, 370 mm, 670 mm, and 970 mm. And, each group of experiments was repeated 10 times, results as shown in Figure 4.14.

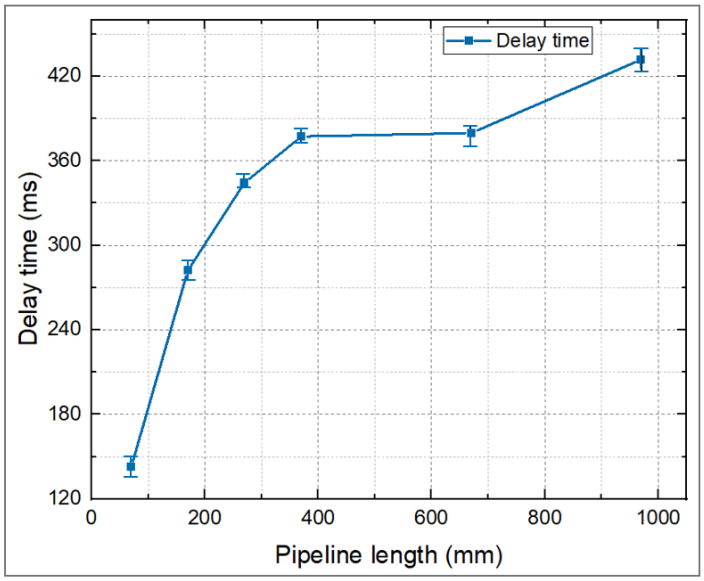


Figure 4.14. Relationship between hydraulic pipeline length and system response delay time.

The average measured delays increased progressively with tube length, ranging from 142.6 ms at 70 mm to 431.9 ms at 970 mm, as shown in Figure 4.14.. The short-length range (70–270 mm) showed a relatively steep rise, with average delays of 142.6 ms (70 mm), 282.3 ms (170 mm), and 344.5 ms (270 mm), representing increments of roughly 140 ms and 62 ms between successive lengths. Beyond 270 mm, the growth rate slowed; the delays for 370 mm (377.4 ms) and 670 mm (379.8 ms) were very similar, indicating a near-plateau in this range. The maximum average delay of 431.9 ms was recorded at 970 mm, confirming the cumulative effect of longer fluid paths on system responsiveness.

4.5.1.4 Displacement amplification experiment

In a hydraulic transmission consisting of syringes with different cross-sectional diameters, the displacement of the output plunger is theoretically amplified according to the ratio of the cross-sectional areas.

This experiment was designed to quantify the actual displacement amplification in the system and to assess potential deviations from theoretical predictions caused by factors such as fluid compressibility, tubing elasticity, and mechanical clearances. Based on the previously described experimental platform, a laser sensor (optoNCDT 1420, MICRO EPSILON, Germany) was integrated to measure the linear travel of the small syringe plunger. The sensor was positioned in line with the plunger axis to directly detect the displacement at the plunger tip during actuation. This modification enabled real-time, non-contact measurement of the output displacement, allowing for accurate quantification of the displacement amplification effect in the hydraulic system.

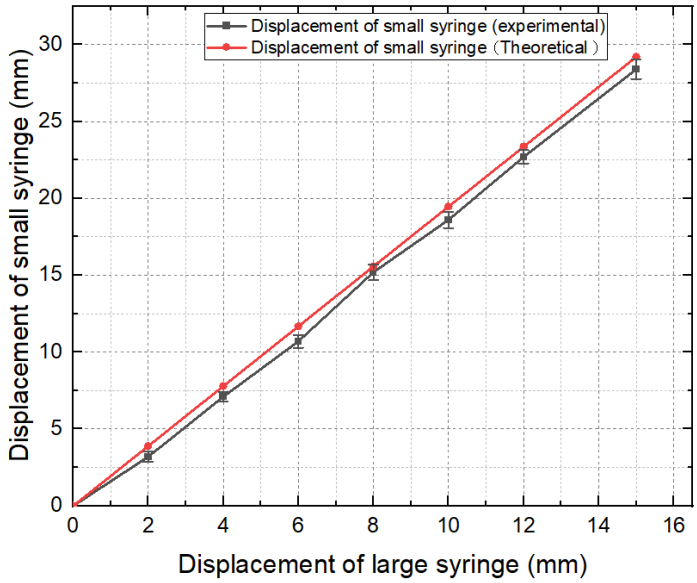


Figure 4.15. Comparison between experimental and theoretical displacement of the small syringe as a function of large syringe displacement.

Figure 4.15. compares the theoretical and measured displacements of the small syringe as a function of the large syringe displacement. Both datasets exhibit a linear relationship, confirming the displacement amplification behaviour predicted by the cross-sectional area ratio of the syringes (theoretical ratio ≈ 2). The measured values closely follow the theoretical line, with only slight deviations attributable to factors such as fluid compressibility, tubing elasticity, and mechanical clearances. Across the tested range (0-15 mm displacement of the large

syringe), the amplification remained consistent, with the measured small syringe displacement reaching approximately 28 mm at a 15 mm large syringe input.

#### 4.5.2 Comparative tests of locomotion performance

To evaluate the improvements in propulsion force and traction efficiency achieved by the redesigned robotic system, we constructed an experimental platform similar to that used for the original prototype, enabling controlled and repeatable comparative testing. The setup consisted of a 3D-printed plastic frame supporting a transparent acrylic tube (representing a simplified colonic environment), a force sensor, and the robot system itself.

Due to the relatively large size of the prototype, the use of a straight rigid acrylic tube presents certain limitations: it cannot fully replicate the anatomical features, compliance, and geometric complexity of the human colon. Nevertheless, this simplified model allows for effective performance benchmarking between the prototypes and serves as a reliable foundation for proof-of-concept validation. To further enhance physiological relevance, we introduced commercially available artificial tissue sheets (Bowel-9mm, Lifelike, Canada) that are commonly used in intestinal modelling and surgical training. These materials were used to line the inner surface of the tube in order to simulate the compliance and fluid-covered texture of real colonic walls. This modification contributed to improving the ecological validity of the experimental data.

##### 4.5.2.1 Prototype propelling force

To systematically evaluate how propulsion performance varies with rotational speed and pipeline friction coefficient, we designed and implemented a dedicated test rig. Each experimental condition was tested with five independent repeats to enhance statistical robustness. In parallel, based on the motor torque–speed characteristics and the derived equations, we computed the theoretical upper bound of propelling force at each speed, which served as a baseline for comparison with the measured results.

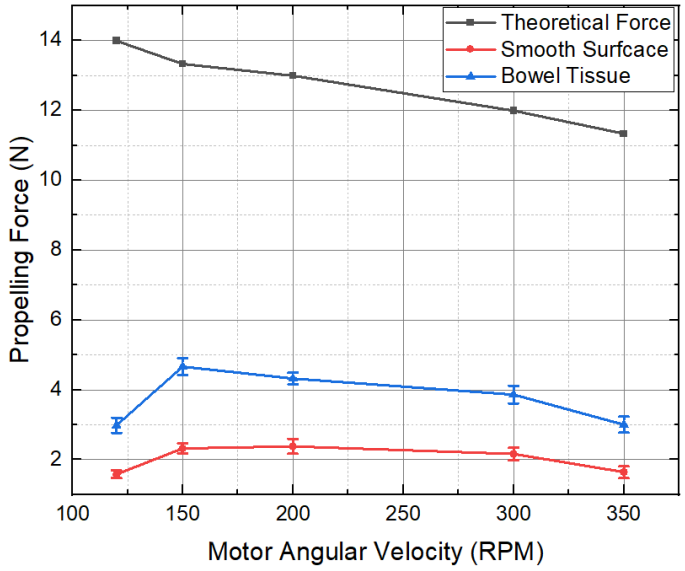


Figure 4.16. Effect of motor speed on propelling force: theory vs. two contact surfaces (smooth surface and bowel tissue).

We mounted the force sensor (LSb201, FUTEK, United States) on the testbed and connected it to the flexible shaft via a string to measure the propelling force. Tests were conducted over 120-350 rpm on both smooth surface and artificial tissue surfaces. Based on the motor torque–speed curve, the theoretical propelling force decreases with increasing speed (Figure 4.16.). In contrast, the measurements show that on the smooth surface the force increases and then stabilizes within 1.5-2.2 N, whereas on artificial tissue it peaks at 4.7 N around 150 rpm and subsequently declines. This behaviour is attributed to reduced transmission efficiency of the flexible shaft and impaired worm-track coupling at higher speeds, causing slippage. The maximum forces achieved are 2.2 N (smooth) and 4.7 N (tissue), representing improvements of 49.7% and 66.1% compared with the previous prototype (1.47 N and 2.83 N, respectively).

#### 4.5.2.2 Propulsion speed testing

To quantify the prototype's propulsion speed and compare it with the prior model, we conducted tests on the rig under two conditions: smooth surface and artificial intestinal tissue, with five independent repeats per condition, the results are shown in Figure 4.17.

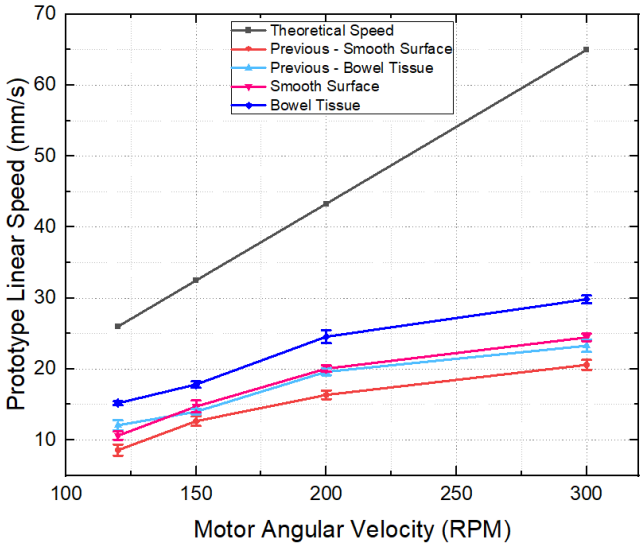


Figure 4.17. Comparison of Propulsion Speed: Current prototype vs. Prior prototype (with smooth surface and silicone -based colon skin)

As shown in Fig. 4.17., we compared the previous and optimized prototypes across motor speeds and contact conditions (smooth surface and bowel tissue). Measured speeds increased monotonically with rpm but remained below the no-slip theoretical limit, indicating persistent transmission losses and slippage. In the figure, cyan and red denote the previous prototype on the smooth surface and bowel tissue, respectively; blue and pink denote the optimized prototype on the smooth surface and bowel tissue, respectively. The optimized prototype outperformed the previous across the entire range of speeds; its maximum bench speed approached 30 mm/s at 300 rpm, which we report solely as a rig-level performance metric and not as a target for in-vivo operation. Notably, speeds on bowel tissue were consistently higher than on the smooth surface. For instance, at 120 rpm the optimized prototype achieved 14.5 mm/s, representing an improvement of 3.9 mm/s  (+36.8%) over the previous (10.6 mm/s)

#### 4.5.2.3 Expansion mechanism experimentation

To assess and compare shape adaptability relative to the previous prototype, tests were conducted in tubes with inner diameters of 120, 140, and 150 mm. For consistency, the motor speed was fixed at 150 rpm, and five independent repeats were performed for each condition. All tubes were lined with artificial intestinal tissue and coated with simulated mucus to approximate the colonic surface. Under these controlled conditions, we measured the propelling force of the prototype across tube diameters; the results are presented in Figure 4.18.

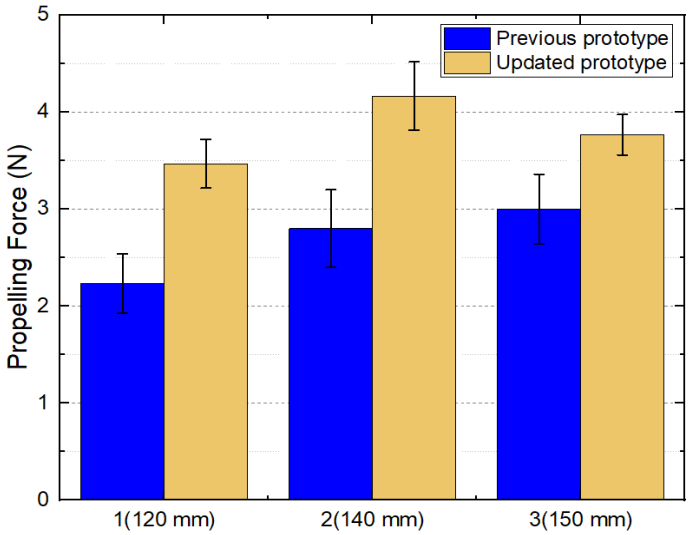


Figure 4.18. Comparison of the propelling force with previous and updated prototype in different tube size.

The yellow bars denote the optimized prototype, and the blue bars denote the original prototype. Across all three tube diameters, the optimized prototype exhibits markedly higher propelling force, with an increase of about 55% for the diameter of 120mm, and the average thrust of the optimized prototype is 3.4 N, 4.2 N for the tube diameter of 140mm (up 46% compared with the original prototype's 2.8 N) and 3.7 N under the diameter of 150mm (up 23% compared with the original prototype's 3 N). These results indicate that improvements to the track structure and the expansion mechanism substantially enhance adaptability and traction across tube sizes. A plausible explanation is the increased stability of the new expansion mechanism: compared with the bellows-based pneumatic approach, a syringe-based hydraulic system provides a more stable and controllable normal load and wall contact, thereby reducing slip, improving effective traction, and ultimately increasing propelling force.

### 4.6 Discussion and summary

The experimental results collectively demonstrate that the improvements implemented in the second prototype effectively enhanced the performance, and stability of the robotic system. The syringe based hydraulic expansion mechanism exhibited fast response during the pressure transmission process, which verified the validity of the mathematical model established in Chapter 4.4. The measured force and displacement relationships closely matched the theoretical predictions, confirming that the liquid filled system behaves as an approximately incompressible within the working range.

The comparative locomotion tests further confirmed that the structural and material optimisations led to a substantial improvement in propulsion efficiency. The TPU tracks provided higher traction stability on lubricated surfaces, while the hydraulic mechanism allowed more accurate control of wall pressure. The combined effect of these two modifications resulted in smoother locomotion and higher repeatability. The reinforced transmission structure, the metallic worm gear, and the additional bearings also contributed to reducing internal friction and mechanical vibration, which improved the overall energy utilisation and motion consistency.

Despite these improvements, several limitations remain. The hydraulic system still exhibits minor hysteresis due to the tubing compliance and seal friction, which could influence dynamic response under fast actuation. Moreover, the current system relies on external motorised syringes for control, which increases the experimental setup size. Future work will focus on miniaturising the hydraulic unit, integrating sensors for real-time pressure monitoring, and optimising the control strategy to achieve more autonomous regulation of wall-press force.

In summary, the experiments presented in this chapter validate the design rationale of the improved prototype. The proposed hydraulic actuation and structural modifications significantly improved propulsion stability and wall-press adaptability, establishing a reliable mechanical foundation for the steering and directional control investigations discussed in Chapter 5.

# 5 Evaluation of force differential steering

## 5.1 Introduction

Navigation within the tortuous and compliant lumen of the colon presents a key challenge for robotic colonoscope. In traditional colonoscopy, the flexible insertion tube is advanced by manual pushing and torquing, which frequently causes loop formation and high wall stress, resulting in patient discomfort and potential tissue injury. To overcome these limitations, robotic colonoscopes have been developed with self-propelling locomotion; however, propulsion alone is insufficient. In a highly curved and slippery environment, a colonoscope must also be capable of actively steering to align itself with the colon pathway and minimize unwanted interaction with the surrounding wall.

Without steering control, the robot tends to deviate from the lumen centreline during motion, especially when entering curved or size-changed sections. This misalignment can lead to excessive wall contact, uneven traction, or complete loss of support, eventually resulting in blockage or slippage. Moreover, when the robot encounters consecutive bends, passive compliance is often inadequate to reorient the body, requiring either excessive propulsion force or manual repositioning [6]. Both scenarios increase the risk of mucosal abrasion and prolong the procedure time [31].

By contrast, active steering allows the robot to proactively regulate its posture and contact pattern before or during turning. This capability brings several benefits:

- it reduces the propulsion force required to traverse sharp bends;
- it maintains balanced wall pressure, minimizing local tissue stress;
- it enables smoother transitions through multi-bend regions; and
- it enhances the overall safety and stability of navigation in confined, fluid-covered environments.

In essence, steering transforms the colonoscope from a purely passive follower of the colon shape into an adaptive, self-adjusting t robotic system.

Various steering mechanisms have been proposed to achieve directional control in in-pipe, endoluminal and soft robotic systems. These mechanisms can generally be divided into those categories:

(1) mechanical differential steering [98-100], this type of steering mainly relies on differential driving speeds between the left and right tracks or wheels, generating a turning moment around

the central axis. It has been widely applied in track-based, wheeled pipe robots and endoluminal robot due to its simplicity and fast response. However, it requires independent actuators and often fails under high wall-friction or small-radius bends.

(2) articulated or joint-based steering [44], Segmented robots employ multiple rigid sections connected by joints, with steering achieved through cables, servos, or pneumatic actuators. This configuration allows precise orientation control and has been used in industrial pipe-inspection systems. Yet, the complex structure and large space occupation limit its miniaturization for medical applications.

(3) magnetic-assisted [86] [87], it utilizes external magnetic fields, generated by permanent magnets or electromagnets, to interact with internal magnetic elements embedded in the robot, producing controllable torque for directional adjustment. This approach enables wireless and continuous steering in confined spaces while reducing onboard actuation complexity. However, magnetic-field-guided systems rely on bulky external magnets and precise field feedback, and their effectiveness decreases rapidly with distance, which limits portability and torque output, making them more suitable for small or soft-bodied robots. [42].

(4) compliant or continuum-based steering [50] [55] [101]. Soft or continuum robots realize steering by modulating internal pressure within pneumatic or hydraulic chambers, enabling continuous bending. Such designs exhibit excellent compliance and safety, making them suitable for narrow or curved ducts [101]. However, the response speed is limited and the control often couples with structural deformation, leading to reduced precision.

Compared to rigid industrial pipelines, the human colon presents unique challenges [10-14]: (1) a non-constant curvature with variable diameter; (2) a soft and deformable wall; (3) a mucus-covered surface that reduces friction; and (4) strict safety constraints on contact pressure. These factors make traditional differential or joint-based steering unsuitable for colon navigation [17].

Roh et al. [98] proposed a differential-drive in-pipe robot capable of turning through multiple independently driven motors. However, the multi-motor configuration increased structural complexity, making size reduction a major challenge for application in the confined colonic environment. Dehghani et al. [50] developed a pneumatically driven self-steering colonoscope that could move at an average speed of 28 mm/s and achieve a minimum turning angle of approximately 30°. Chen et al. [55] designed an inchworm-inspired soft robotic colonoscope based on rubber bellows, which offered excellent compliance and wall safety but suffered from

limited steering precision due to pneumatic hysteresis and structural constraints. Vucelic et al. [44] introduced the Aer-O-Scope system, which enabled full-length colon examination; however, its operation mode remained similar to conventional colonoscopy and exhibited limited autonomous navigation capability. Verra et al. [87] proposed a magnetically actuated, soft-tethered capsule that allows non-contact orientation adjustment, but its reliance on bulky external magnets and precise field feedback reduced portability. Giri et al. [101] developed the *InchIGRAB* mechanism combining guided traction with continuum bending, capable of operating through bends of 80-130°, though its multi-chamber design increased synchronization complexity and reduced response speed.

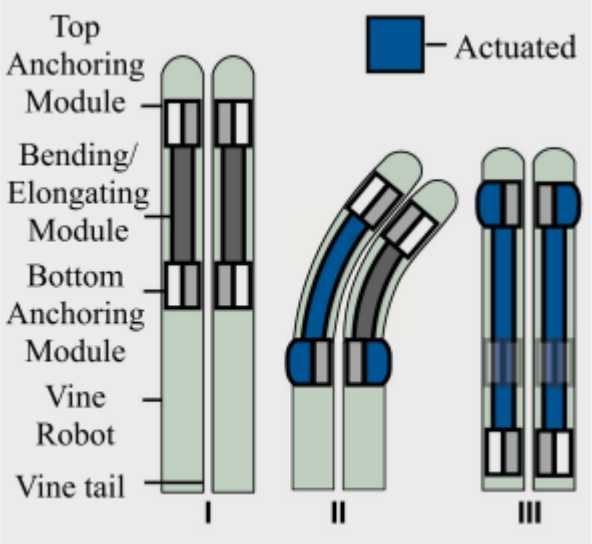


Figure 5.1. Schematic of the system showing the InchIGRAB module integrated between the body and tail sections of the vine robot [101].

Overall, these studies illustrate the evolution of steering mechanisms from rigid differential and articulated structures toward flexible, pneumatic, and magnetically assisted hybrid designs. However, when faced with the complex and highly variable anatomy of the colon, the limitations of these approaches remain evident.

To address these challenges, this concept introduces a force differential steering mechanism integrated into a four-track robotic colonoscope. By selectively retracting one or more tracks using a syringe-driven hydraulic system, the robot generates asymmetric wall-press forces that produce a controllable yaw moment for directional change. This approach eliminates the need for external magnetic fields or complex joints and provides a compact, simple, and stable method for steering.

The following sections detail the principle, mathematical modelling, and experimental validation of this mechanism, focusing on its feasibility, dynamic behaviour, and adaptability under different geometric and frictional conditions.

### 5.2 Principle of steering mechanism

The proposed robotic colonoscope consists of four evenly distributed tracks arranged circumferentially around the body, each separated by 90°. All tracks are synchronously driven by a single external motor through a flexible shaft and worm-gear transmission, ensuring identical linear velocity for each track during propulsion. Because differential speed control is not feasible in this configuration, directional changes cannot be achieved by conventional differential drive. Instead, steering is realized by regulating the normal contact forces between the tracks and the colon wall through a hydraulic expansion mechanism.

Each track is connected to a syringe-driven hydraulic actuator that controls its radial deformation. When hydraulic pressure is applied, the track expands outward to press against the wall, generating a normal force that provides frictional traction for forward motion. Conversely, retracting the hydraulic actuator decreases the contact pressure, partially detaching the track from the wall and reducing its traction. By selectively retracting one or more tracks, an asymmetric wall-press distribution is created around the robot circumference.

During straight motion, all four tracks maintain equal wall contact, and the resultant tangential forces are balanced, producing zero yaw torque. When steering is required, the hydraulic system retracts the tracks on one side of the robot (for instance, the left). This reduces their normal forces and frictional traction, while the opposite (right) tracks maintain full wall contact and continue to generate a larger force. The difference in traction between the two sides induces a yaw moment around the robot's central axis, rotating its body toward the side with bigger traction (i.e., toward the right). Once the robot realigns with the curvature of the intestinal path, the hydraulic pressures are equalized again to restore symmetric wall contact for stable propulsion.

This process can be interpreted as a "force differential steering" mode, where the difference in wall-press forces replaces the conventional differential track speeds. The magnitude of the generated yaw torque is determined by both the normal-force difference and the effective lever arm between opposite tracks. By precisely controlling the syringe displacement or hydraulic pressure, the robot can achieve smooth, continuous, and reversible steering while maintaining stable wall adhesion. This mechanism allows the robot to conform naturally to curved segments

without losing traction or causing excessive wall stress, providing a simple yet robust solution for navigation in narrow and slippery lumens.

### 5.3 Mathematical modelling of steering

5.3.1 Geometric constraint analysis

When the robot travels through a curved section of the colon, its geometric dimensions must satisfy specific spatial constraints imposed by the pipe's curvature. If the robot body is excessively wide or long relative to the inner diameter and curvature radius of the pipe, it may experience wall interference or fail to align with the bending trajectory. Therefore, a geometric constraint analysis is necessary to determine the admissible range of the robot's body width $W$and length $L$, ensuring that the robot can smoothly pass through curved segments without collision or excessive deformation.

Figure 5.2. illustrates the geometric relationship between the robot and the curved pipe, where $R$denotes the curvature radius, $D$is the inner diameter of the pipe, $W$ is the robot width, $L$ is the robot length, and $\gamma$ represents the bending angle of the curved section. Based on this configuration, the following geometric constraints can be derived to describe the feasible range of $W$ and $L$.

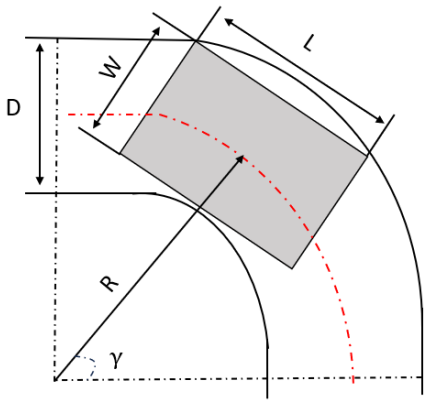


Figure 5.2. Geometric Model of the Robot in a Curved Section.

The width W of the robot satisfies the following relationship:

$$\left(R+\frac{D}{2}\right)\cos\gamma-\left(R-\frac{D}{2}\right)<W<D \tag{1}$$

The limit of the robot length L is:

To ensure that the robot can pass through the curved pipe, the distance difference between the robot's corner point and the pipe wall must be equal to half of the robot's length, that is:

$$\frac{L}{2} = \sqrt{\left(\frac{D}{2} + R\right)^2 - \left(R - \frac{D}{2} + W\right)^2} \tag{2}$$

The distance relationship of L can be obtained:

$$L = 2\sqrt{\left(\frac{D}{2} + R\right)^2 - \left(R - \frac{D}{2} + W\right)^2} \tag{3}$$

5.3.2 Establish a curved pipe model

The curved pipe can be regarded as a circle with a diameter of D, which is generated by rotating around the centre of curvature o, and a coordinate system XYZ is established at the center of curvature o. $\alpha$ is the rotation angle of the orbital circle interface.

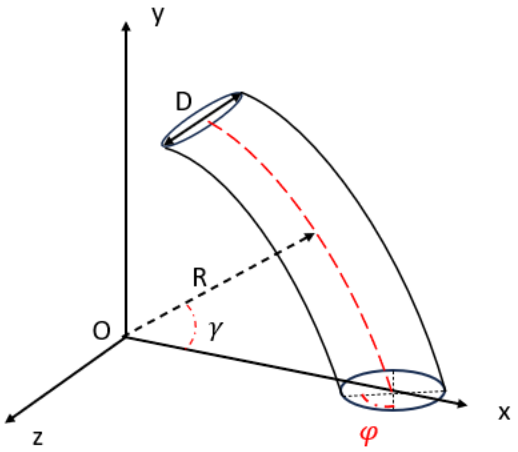


Figure 5.3. Geometric representation of a curved tube.

It should be noted that the above expression of the curved pipe only includes the $x$ and $y$coordinates because the curve lies on the $x$-$y$ plane, with the $z$-axis representing the out-of-plane direction. In this formulation, the pipe centerline is defined as a circular arc with radius $R$in the $x$-$y$ plane, and the local cross-section at each position is perpendicular to this plane. Therefore, $z$ is not an independent variable in the projection view of Figure 5.3.. When the spatial geometry of the pipe is considered in full three dimensions, the coordinate $z$ can be introduced through the cross-sectional rotation angle $\varphi$, yielding the complete toroidal representation:

$$P(\gamma, \varphi)\begin{bmatrix}\left(R + \frac{D}{2}\cos\varphi\right)\cos\gamma \\ \left(R + \frac{D}{2}\cos\varphi\right)\sin\gamma \\ \frac{D}{2}\sin\varphi\end{bmatrix} \tag{4}$$

Where. $P(\gamma, \varphi)$ denotes the spatial position vector of a point on the pipe surface. When the pipe is straight, the cross-section remains identical along the z-axis; therefore, the spatial dependence on z can be omitted, and the cross-section can be simply expressed by Eq. (5) as a circle of radius $D/2$ cantered at (R, 0).

$$(x - R)^2 + y^2 = \frac{D^2}{4} \tag{5}$$

The movement of the robot in the colon bend can be considered to have the following stages:

1. When the robot is in a posture where part of the body is already in the curved pipe and the other part is in the straight pipe. At this time, the movement of the pipeline robot can be decomposed into two parts, one part is the translation of the robot along the X axis, and the other part is the rotation around its own Z' axis. This is the robot's entry stage in the curve movement.
2. When the robot leaves the curved pipe, part of the robot is already in the straight pipe, and the other part is still in the curved pipe. At this time, the robot's movement is divided into translation along the negative direction of the Y axis and rotation around its own Z' axis.
3. When the robot is completely in the curve, the robot's centre of mass can be regarded as a rotation along the centreline of the colon. In this state, the angular velocity and angular acceleration of each point on the robot are the same.
4. During bending motion, the normal forces acting on individual tracks continuously change with curvature and contact orientation. These variations play a crucial role in maintaining traction and stabilizing the robot's posture within the curve.

5.3.3 Track's normal force and traction

Each track, when in contact with the inner pipe wall, is controlled by an expansion mechanism. In this mechanism, a syringe acts as a linear actuator directly connected to the track, enabling its deformation and contact with the pipe. We simplify each track as a spring-contact model. When a track contacts the pipe wall, the normal force can be expressed as:

$$N_i = k_n(\delta_0 - r_i) \tag{6}$$

Where $N_i$ is the normal force of tracks, $k_n$ is the equivalent normal stiffness, which is related to the material elasticity and contact area; $\delta_0$ is the preload compression when the track is placed in the pipe; $r_i$ is the deformation of the track under hydraulic action. It define $r_i$ as positive when the track is retracted.

Thus, the friction traction of the robot can be expressed as:

$$F_{t,i} = -\mu_k N_i sgn(v_{s,i}) - c_v N_i v_{s,i} \tag{7}$$

Where, $\mu_k$ is the kinetic friction coefficient, $c_v$ is the viscous friction coefficient; $c_v N_i v_{s,i}$ is the viscous shear term; $sgn(x)$ is the sign function. To ensure clarity in the interpretation of the steering model, the tangential force $F_{t,i}$is defined as the force exerted by the surrounding wall on the $i$-th track, and the slip velocity $v_{s,i}$is defined as the relative velocity between the track and the wall. Under this definition, the tangential force always acts in opposition to the direction of slip.

$$sgn(x) = \begin{cases} +1, & x > 0 \\ 0, & x = 0 \\ -1, & x < 0 \end{cases} \tag{8}$$

In this project, aside from the frictional traction force from the tracks, there is no other propulsion mechanism. The propulsion relies entirely on friction; therefore, there is no fundamental difference in meaning between traction force and frictional traction force.

5.3.4 Steering analysis

The central trajectories of the robot's four tracks differ: the inner path is shorter, while the outer path is longer. If the linear velocities of the four tracks are identical, it will inevitably lead to a mismatch between the required differential speed and the actual supply. In this project, all four tracks simultaneously engage with a single worm gear. Consequently, the tracks on the outer side of the curve are more prone to slippage.

Approximating the centreline of the curved pipe as a circle with radius $R_c$. By offsetting this circle in the normal direction by $y_i$, a parallel curve is obtained, whose radius is:

$$R_i = R_c + y_i \tag{9}$$

For the same angular displacement $\Delta\theta$, the arc length of the centerline is:

$$\Delta x = R_c \Delta\theta \tag{10}$$

Therefore, the arc length for the each parallel curve is:

$$\Delta S_i = (R_c + y_i)\, \Delta\theta \tag{11}$$

The difference between the two is:

$$\Delta l = \Delta S_i - \Delta x = \frac{y_i}{R_c} \Delta x \tag{12}$$

The velocity increment is:

$$\Delta v = v_i - v = v \frac{y_i}{R_c} \tag{13}$$

In short, when the robot moves through a curved pipe, the four tracks generate a velocity difference $\Delta v$ due to their different path radius. At constant speed, this inevitably leads to a pair of opposing slips. Therefore, the hydraulic device in the expansion mechanism can be used to actively adjust $N_i$, ultimately achieving a yaw moment for stable steering.

- Yaw moment for active steering

Considering the robot body as a rigid body with a cross-sectional radius of $r_b$, its yaw (steering) moment originates from the difference in traction between the left and right tracks:

$$M_\varphi = \sum_i F_{t,i} r_b \sin(\theta_i - \beta) \tag{14}$$

where $\beta$ is the yaw angle of the robot relative to the curved pipe coordinate system, as shown in Figure 5.4..

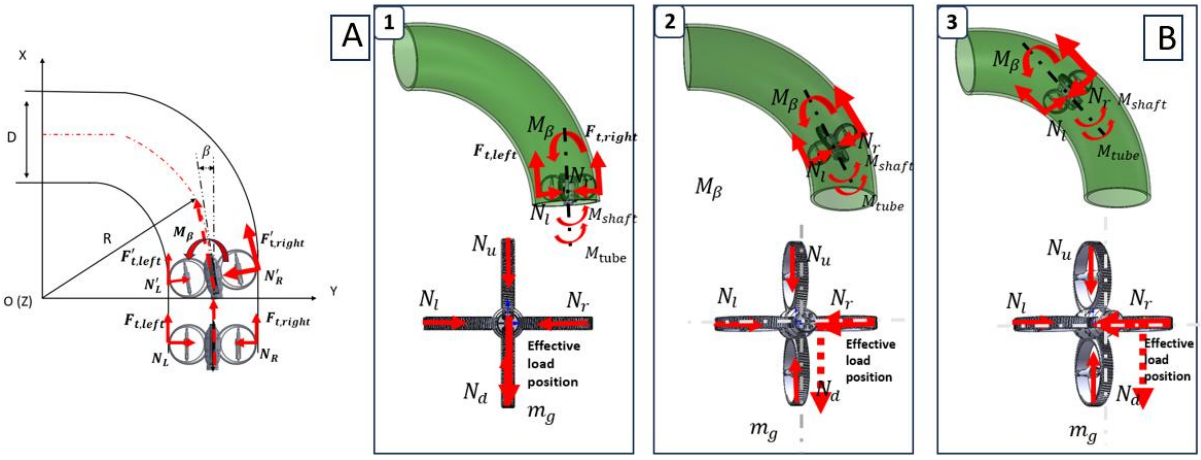


Figure 5.4. Schematic of the robot steering mechanism in a colon bend: (A) 2D geometric and force relationship; (B) 3D full-field force analysis.

The terms $N_l$, $N_r$, $N_u$, and $N_d$ denote the normal contact forces between the robot tracks and the surrounding wall on the left, right, upper, and lower sides, respectively. These forces are determined by the track expansion state and the redistribution of load due to gravity. As the contact configuration changes, the load is unevenly distributed among the tracks, resulting in variations in the normal forces.

Under the simplified assumption of zero yaw angle:

$$M_\beta = r_b\left(F_{t,left} - F_{t,right}\right) \tag{15}$$

At this point, if the right track is retracted (i.e., $r_{right}$ increases, $N_{right}$ decreases), leading to a reduction in the magnitude of the corresponding tangential force. As a result, yielding $M_\beta < 0$.

The steering model described by Eq. (15) captures the primary mechanism of yaw generation, which is governed by the traction imbalance between the left and right tracks. Under this formulation, the yaw moment is determined by the difference in tangential forces, assuming a simplified and symmetric distribution of contact forces.

To further illustrate the effect of gravity under varying expansion conditions, Fig. 5.4 shows how the effective gravitational moment evolves with track retraction. Under symmetric expansion, the load is approximately evenly distributed and the effective load application point is near the cross-sectional centre, resulting in a negligible gravitational contribution to yaw moment.

As the expansion becomes asymmetric, e.g., when the left track is retracted, the contact condition weakens on that side, leading to a redistribution of load towards the right. This causes a shift in the effective load application point and an increase in the moment arm of the gravitational force. With increasing retraction, this shift becomes more pronounced, resulting in a higher effective gravitational moment, as illustrated in Fig. 5.4 (B, 1-3). This effect arises from changes in load transmission rather than any variation in the magnitude or direction of gravity. In addition, the overall yaw moment is influenced by structural effects and the flexible shaft generates a restoring moment $M_{shaft}$, opposing the yaw motion, while the hydraulic tubes introduce an additional moment $M_{tube}$ due to asymmetric constraint forces.

Therefore, the yaw behaviour is governed by the combined effects of traction imbalance, gravity-induced load redistribution, and structural constraints, providing a more complete explanation of the observed deviations from the simplified model.

To account for these additional effects, Eq. (16) can be extended as:

$$M_{\beta} = r_b\left(F_{t,left} - F_{t,right}\right) + M_{shaft} + M_{tube} \tag{16}$$

where $M_{shaft}$, $M_{tube}$ represent the equivalent yaw moments induced by the flexible shaft stiffness and tube constraints, respectively.

The term $M_{shaft}$ originates from the bending and torsional stiffness of the flexible shaft. During steering, deformation of the shaft generates a restoring moment opposing the yaw motion, which can be approximated using an equivalent linear stiffness model:

$$M_{shaft} = -k_{\theta}\beta \tag{17}$$

where $k_{\theta}$ is the equivalent rotational stiffness and $\beta$ is the yaw angle.

The term $M_{tube}$ arises from asymmetric constraint forces induced by the hydraulic tubes. Due to their routing and deformation during steering, the tubes impose uneven forces on the robot body. These forces can be mapped into an equivalent yaw moment using the moment definition

$$M_{tube} = r_b\left(F_{tube,left} - F_{tube,right}\right) \tag{18}$$

It should be noted that gravitational effects are not introduced as an independent moment term. Instead, gravity influences the steering behaviour indirectly by modifying the normal force distribution among the tracks, which in turn alters the available traction forces. As the robot undergoes configuration changes during steering, this redistribution leads to a configuration-dependent variation in the resulting yaw moment.

These additional contributions primarily act by modifying the normal force distribution among the tracks, rather than introducing a fundamentally different steering mechanism. The dominant factor remains the traction imbalance between the tracks. Nevertheless, the inclusion of these secondary effects provides a more realistic interpretation of the system behaviour and helps explain deviations observed between the simplified model and experimental results, particularly in complex curved environments.

Due to the geometric characteristics of the curved pipe and the influence of friction within the pipe wall, a restoring moment is generated on the robot, pulling its direction back toward the tangential direction of the pipe. This restoring moment acts as a resistive yaw moment against the robot's steering direction, opposing the turn. In other words, the applied steering moment must overcome the environmental restoring moment to ensure stable steering of the robot, i.e.:

$$|M_\beta| \geq |M_{\beta,f}| \tag{19}$$

$$\left|M_{\beta,f}\right| = \alpha\mu_k N_{total}\frac{r_b^2}{R_b} \tag{20}$$

where $N_{total}$ is the total normal force on the robot, and $\alpha$ is a calibration coefficient, with $\alpha \in (0,1]$.

Finally, the pass-ability index for the robot navigating through the curved pipe can be obtained as:

$$\Gamma = \frac{|M_\beta|}{|M_{\beta,f}|} \geq 1 \tag{21}$$

Among them, Γ is the steering margin.

Table 5-1 Definition of symbols related to force differential steering.

| Symbol name | Symbol meaning |
|---|---|
| $R_c$ | Curvature radius of the bend， $\frac{D}{2}$ |
| $r_b$ | Robot body radius , $\frac{d}{2}$ |
| $y_i$ | Lateral offset of the each track relative to the pipe centre |
| $v_i$ | Linear velocity of the track |
| $v_{s,i}$ | Track slip velocity |
| $N_i$ | Normal force on any track |
| $r_i$ | Track deformation amount |
| $\delta_0$ | Track preload compression amount |
| $k_n$ | Equivalent normal stiffness |
| $\mu_k$ | Kinetic friction coefficient |
| $F_{t,i}$ | Frictional traction force of the track |
| $sgn(x)$ | Sign function |
| $c_v$ | Viscous friction coefficient |
| $\mu_k$ | Kinetic friction coefficient |
| $c_d$ | Viscous resistance coefficient |
| $F_0$ | Coulomb friction resistance |
| $\Delta S_i$ | Arc length increment |
| $\Delta v$ | Velocity increment |
| $\theta_i$ | Azimuth angle of the four tracks in the robot's own coordinate system |
| $\beta$ | Yaw angle of the robot relative to the curved pipe coordinate system |
| $M_\varphi$ | Yaw (steering) moment |
| $\alpha$ | Calibration coefficient |
| $N_{total}$ | Total normal force on the robot |

| | |
|---|---|
| Γ | Steering margin for the robot passing through the curved pipe |

## 5.4 Experiment setup and results

To validate the proposed force differential steering mechanism and the theoretical model developed in Section 5.3, a series of experiments were conducted using a dedicated test platform. These experiments aimed to

(1) characterize the relationship between hydraulic actuation and traction force,

(2) verify the robot's steering capability in curved environments, and

(3) evaluate how curvature, frictional conditions, and continuous bending geometries affect steering performance.

The experimental setup was designed to reproduce realistic colonic conditions while allowing precise control of curvature radius, and wall contact force. The test platform integrates mechanical, hydraulic, and sensing subsystems, including a synchronized track drive, syringe-based expansion mechanism, and multi-sensor data acquisition for force and motion measurement. Both straight-tube and curved-tube tests were performed to assess the steering performance under various controlled parameters.

### 5.4.1 Experiment setup

In this experiment, a flexible corrugated duct was used instead of rigid transparent acrylic tubes to better simulate the mechanical characteristics of the human colon. The duct is made of lightweight aluminium composite material with a spiral corrugated surface, which provides both structural flexibility and elastic resilience. Its high compliance allows it to be manually shaped into different curvature configurations, including single bends and continuous S-shaped geometries, while maintaining sufficient restoring force to mimic the passive elasticity of intestinal walls.

Figure 5.5. Corrugated aluminium duct (D = 152mm).

The use of this flexible duct offers several advantages over rigid pipes. First, it allows the curvature and orientation of the testing environment to be continuously adjustable, enabling the same setup to replicate different intestinal geometries (e.g., 90°, 120°, or multi-bend configurations). Second, its surface friction (after adding artificial intestinal tissue) and slight compressibility reproduce the deformable and compliant nature of colonic tissue more realistically than rigid materials. Finally, the corrugated texture helps to simulate the mucosal folds of the colon, providing a more representative traction and contact condition for the robot's tracks.

The duct used in this study had an inner diameter of approximately 152 mm and a total length of 1000 mm (continuous bend). During testing, it was fixed onto an acrylic base to maintain stability while allowing controlled curvature adjustments between trials. This flexible environment enabled the assessment of the robot's propulsion and steering behaviour under conditions closer to those encountered in actual endoluminal navigation.

The head-mounted configuration ensured that the IMU (Xsens DOT, Movella, US) accurately reflected the robot's actual turning motion as it entered and exited curved sections. The sensor was housed within a custom 3D-printed base, which was securely fixed to the front head of the robot to maintain alignment and minimize vibration, as shown in Figure 5.6. The IMU data were sampled at 15 Hz and recorded through the dedicated software.

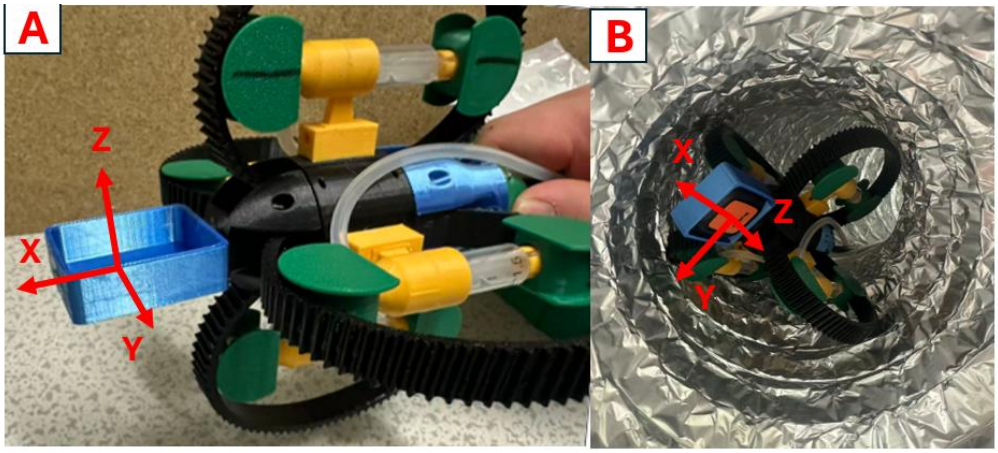


Figure 5.6. Coordinate definition and experimental setup of the robotic colonoscope. (A) The fixture designed for mounting the IMU sensor on the robot head. (B) The robot during locomotion inside the test duct, with the X, Y, and Z axes indicating the IMU coordinate directions (X: forward, Y: lateral, Z: vertical).

For traction measurement, the load cell (DBBSM Load Cell, Applied Measurements Ltd, UK) was connected to the flexible shaft via a thin cable aligned along the shaft axis. This setup allowed the sensor to record the axial pulling force generated by the robot during propulsion without constraining its motion. For the normal force of track's measurement, the same sensor was rigidly attached to the track module, allowing the direct measurement of the wall normal force of track produced by the hydraulic expansion mechanism. By incrementally increasing the syringe displacement, the relationship between hydraulic input and normal force of track was characterized quantitatively.

### 5.4.2 Force characterization experiments

As shown in Figure 5.7., in each case, one track was hydraulically retracted while the remaining three maintained full wall contact. This asymmetric wall-press distribution was used to investigate how localized pressure reduction affects the overall traction performance of the robot. The circular insets illustrate the corresponding cross-sectional contact states between the four tracks (black) and the pipe wall (red ring).

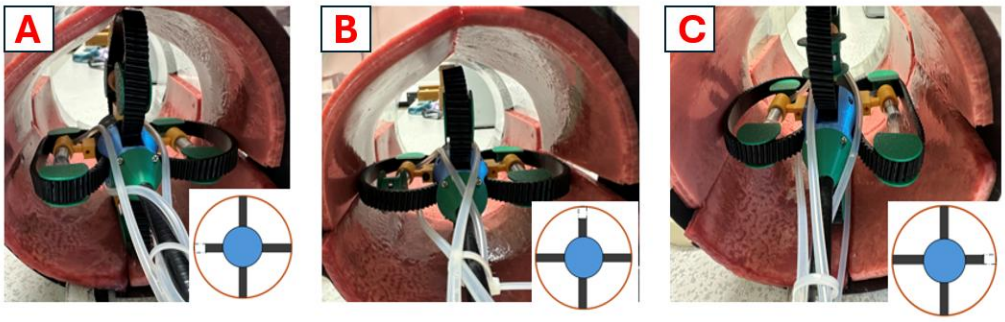


Figure 5.7. Experimental configurations for traction measurement under different track retraction conditions. (A) Left track retracted, (B) Top track retracted, and (C) Right track retracted.

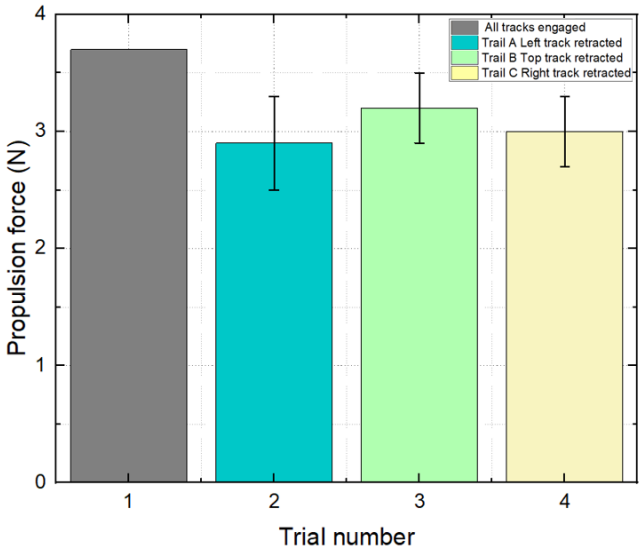


Figure 5.8. Comparison of measured traction forces under different track configurations.

Retracting one track reduces the total traction due to decreased wall contact pressure. When all four tracks remained in full contact with the wall, the average propulsion force reached 3.7 N (measured in Chapter 4), which serves as the baseline performance. When one track was hydraulically retracted, the overall traction force decreased due to the local reduction in wall contact pressure.

For Trial A, the mean propulsion force dropped to approximately 2.9 N, while Trial B produced a slightly higher value of 3.2 N. In Trial C, the traction was similar to the left-side case, around 3.0 N. The reductions correspond to about 20-25 % loss relative to the baseline. This trend indicates that retracting a single track significantly weakens the total driving capability, and that lateral retraction (left or right) has a stronger influence than vertical (top) retraction.

The observed asymmetry can be attributed to two combined effects: (1) the decrease of normal force on the retracted side reduces available frictional traction; (2) the resulting unbalanced wall-press distribution generates a yaw moment, diverting part of the traction into rotational motion instead of forward propulsion. These results confirm the theoretical prediction that local force imbalance directly affects both propulsion efficiency and steering torque generation.

In order to quantify how the hydraulic system input affects the normal force applied on a single track, a load cell (DBBSM Load Cell, Applied Measurements Ltd, UK) was used to measure the wall normal contact force exerted by the track during expansion.

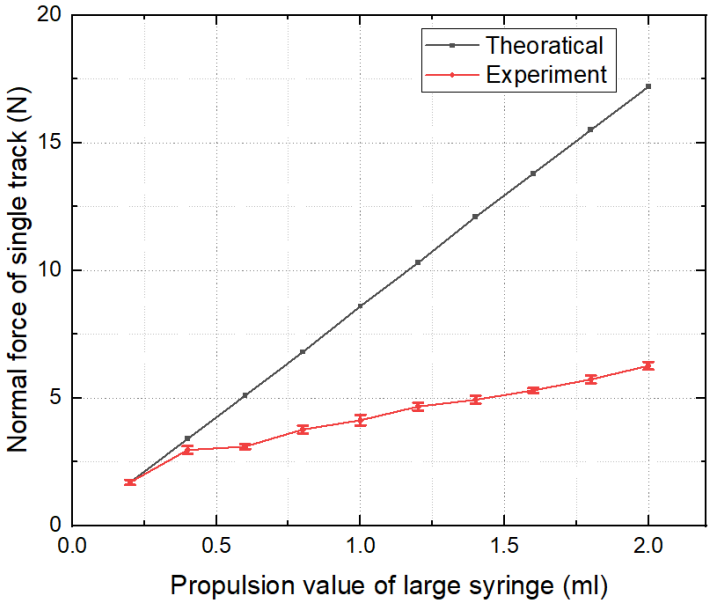


Figure 5.9. Measured and theoretical normal forces of a single track under different hydraulic pressure.

During the test, the track module was placed on a rigid support, with the load cell mounted directly behind the track pad to record the reaction force normal to the wall. The large syringe (diameter 12 mm) was manually advanced in increments of 0.2 mL, while the small syringe connected to the track actuator (diameter 8.6 mm) transferred the pressure to the expansion chamber. For each step, the corresponding normal force was recorded after the system reached a steady state. This procedure was repeated five times, and the mean value with standard deviation was used to plot the experimental curve, as shown in Figure 5.9..

The experimental results (red line) show a near-linear increase in normal force with hydraulic input but with a significantly lower magnitude than the theoretical value (black line). At a syringe input of 2 mL, the measured normal force reached approximately 6 N, while the theoretical model predicted around 20 N. The discrepancy can be attributed to fluid leakage,

bubble presence in the liquid, and structure deformation, etc. within the miniature hydraulic circuit, which cause part of the input displacement to be lost before reaching the actuator. Nevertheless, the overall linear trend confirms that the hydraulic expansion mechanism provides a controllable and proportional modulation of the track-wall contact force, validating its suitability for steering control.

### 5.4.3 Steering experiments

To evaluate the steering performance of the robot inside curved ducts, a series of experiments were conducted using the Xsens DOT IMU mounted on the robot head, see Figure 5.6. The IMU provided real-time measurements of the yaw angle, allowing quantitative analysis of the robot's turning motion under different conditions.

These experiments aimed to verify whether the proposed force differential mechanism can actively generate sufficient yaw motion to assist the robot in passing through curved paths. The study also investigated how factors such as pipe curvature, wall friction, etc. influence the steering behaviour. By comparing active and passive steering, as well as single and continuous bends, this section establishes the relationship between hydraulic actuation and actual steering response recorded by the IMU.

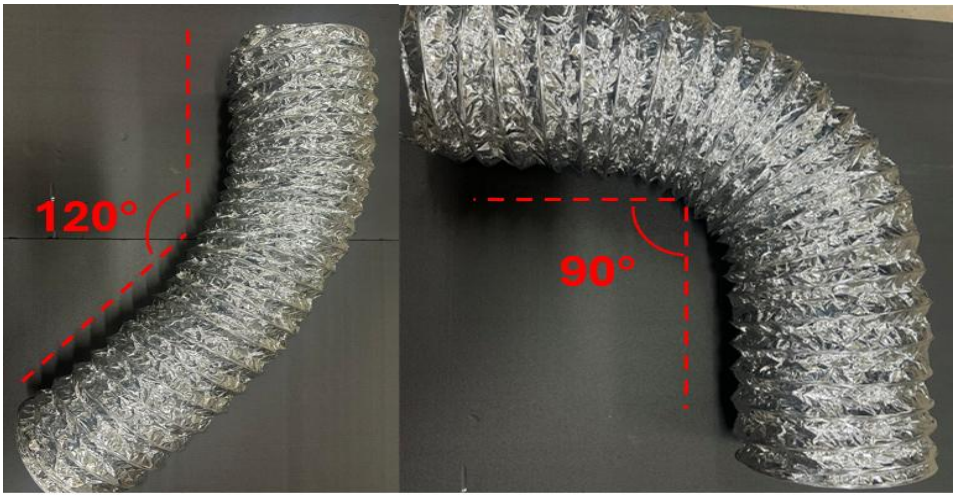


Figure 5.10. Corrugated aluminium duct with 90° and 120° bending angles used for steering experiments.

The ducts were manually shaped from the same flexible corrugated tube to reproduce different colon-like curvatures. The 90° bend was mainly used to evaluate the influence of wall friction on steering performance, while the 120° bend was used to compare active and (inactive) passive hydraulic steering modes. Both geometries provide realistic curvature conditions for testing the robot's turning capability inside confined lumens.

To evaluate the performance of force differential actuation steering, the robot was tested in a 120° curved duct under two steering modes:

(1) inactive steering, where no hydraulic retraction was applied and all four tracks remained at their nominal contact height, driven solely by the external motor through equal-speed rotation; and

(2) active steering, where a hydraulic input was introduced as the robot entered the bend to induce asymmetric track deformation and facilitate turning.

The yaw angle was continuously recorded by the IMU mounted on the robot head. The geometric bending angle of the duct (120°) corresponds to an actual turning requirement of approximately 60° for the robot, since it moves along the centreline rather than rotating about the curvature centre. The measured yaw angle is slightly smaller than this theoretical value due to the flexibility and deformation of the duct, as well as the robot's body vibrations during motion, both of which reduce the effective alignment change detected by the IMU.

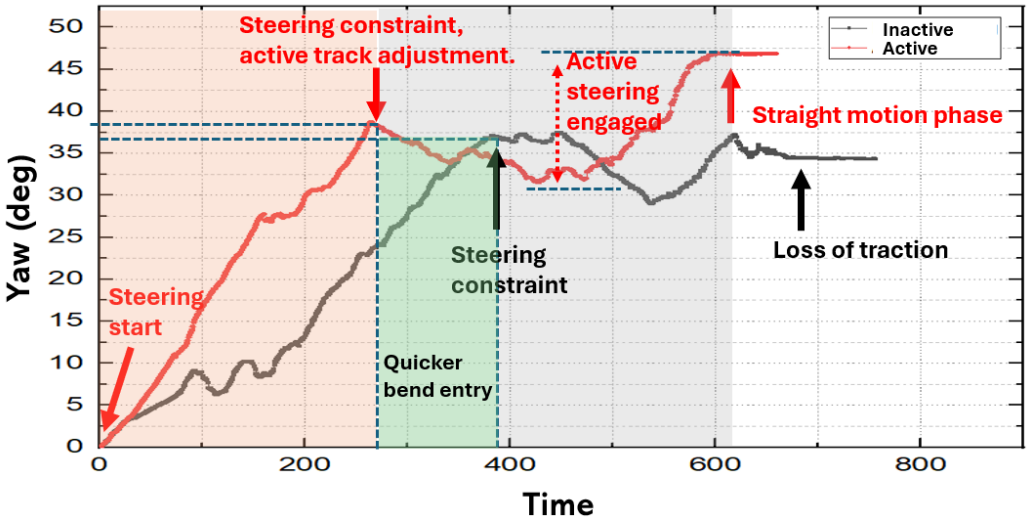


Figure 5.11. Comparison of yaw angle evolution between active and inactive steering during a 120° bend.

In the inactive mode (black curve), the robot began turning gradually after entering the curved section, but the yaw angle increased slowly and saturated at around 35°, which is notably smaller than the required 60°. After approximately data index 600 (corresponding to about 40s of motion), the robot exhibited a clear loss of traction, reflected by fluctuations and the stop of yaw, indicating that the tracks slipped against the wall and the robot could no longer advance smoothly. This behaviour suggests that purely passive contact forces are insufficient to generate the necessary yaw moment for large curvature navigation.

In contrast, during the active steering mode (red curve), the hydraulic system retracted one side's tracks as the robot approached the bend, creating a wall-pressure asymmetry that produced an additional yaw moment. As a result, the robot entered the bend earlier and more smoothly, and the yaw angle rose to about 45°, reaching a steady state with minor variation. The shaded regions in the figure highlight distinct motion phases: (1) steering start, (2) constraint region where wall pressure adjustment occurred, and (3) straight motion phase after exiting the bend. The quicker rise and higher steady-state yaw in the active case confirm that force differential steering significantly enhances turning efficiency and stability compared to the passive motion. These results experimentally validate the theoretical model predicting that increased hydraulic asymmetry produces a larger effective yaw torque, enabling the robot to negotiate curves without losing traction.

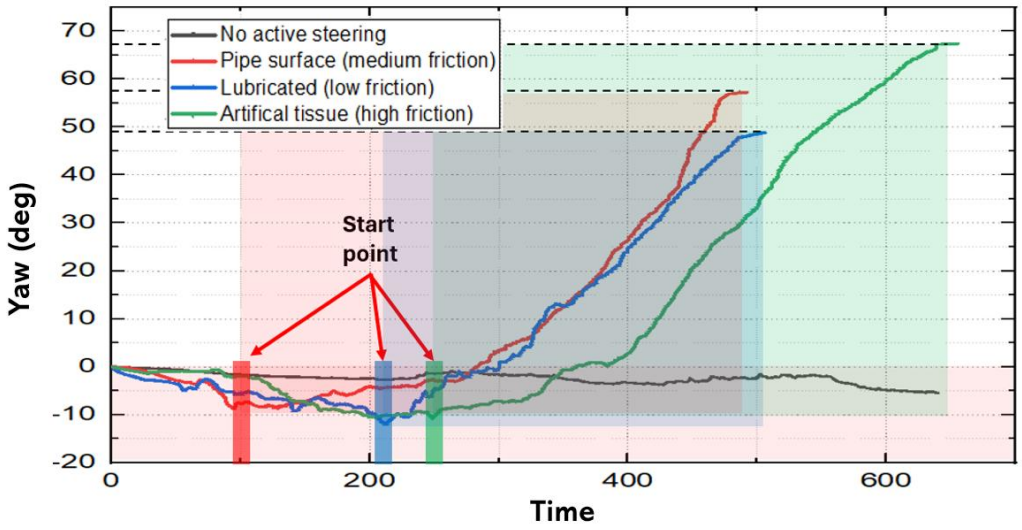


Figure 5.12. Yaw angle under different wall friction conditions in a 90° bend. duct surface (medium friction, red), lubricated surface (low friction, blue), and artificial tissue (high friction, green).

At the start of each trial, the robot entered the bend at approximately the same position (indicated by the shaded regions in the figure). Without active steering (black curve), the yaw angle remained nearly constant around 0-5°, indicating that the passive wall-press forces alone could not generate sufficient torque to overcome the pipe curvature. When hydraulic actuation was applied, clear differences emerged among the three frictional conditions.

Under the high-friction condition (green line), the yaw angle increased rapidly after entering the bend and reached approximately 80° (start from approximately -15° to 65°), showing a smooth and continuous growth with minimal oscillation. The robot was able to maintain strong

traction and complete the steering efficiently. For the medium-friction surface (red line), the yaw angle increased at a slower rate and stabilized at around 50°. Under the low-friction (lubricated) surface (blue line), the robot exhibited the slowest yaw development and the smallest final value (about 40°). In this case, the robot slide inside the curve, which delayed its response and insufficient steering.

The results clearly demonstrate that wall friction is a critical in an effective yaw motion. Higher wall friction enhances coupling and allows the force differential between tracks to be efficiently transferred into steering torque. In contrast, excessive lubrication reduces the effective contact force and leads to partial loss of traction. Therefore, in the low-friction environment similar to colon, in order to realize stable active steering, higher hydraulic actuation or adjustable wall pressure distribution control strategy is required.

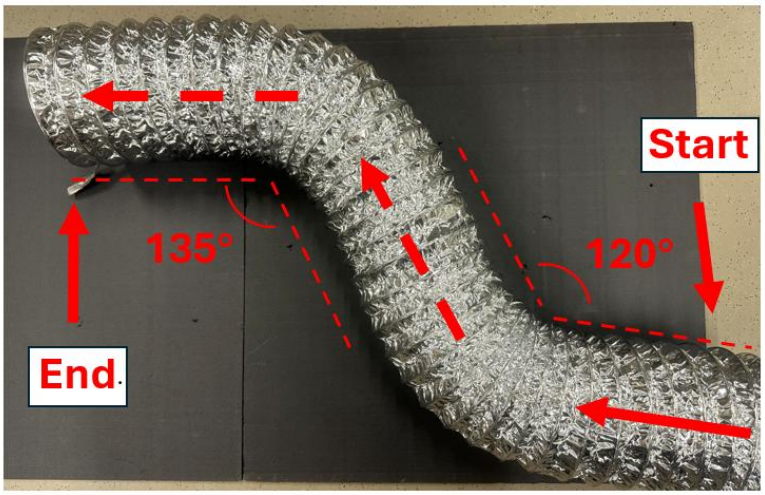


Figure 5.13. Configuration of the continuous S-shaped flexible duct used for steering experiments.

The duct consists of two consecutive bends: a approximately 120° right bend followed by an approximately 135° left bend, manually shaped from a flexible corrugated tube to simulate complex colon-like curvature. The Start and End positions indicate the robot's entry and exit points. This geometry was used in IMU-based tests to evaluate the robot's ability to perform successive steering manoeuvres and maintain traction across consecutive curvature transitions.

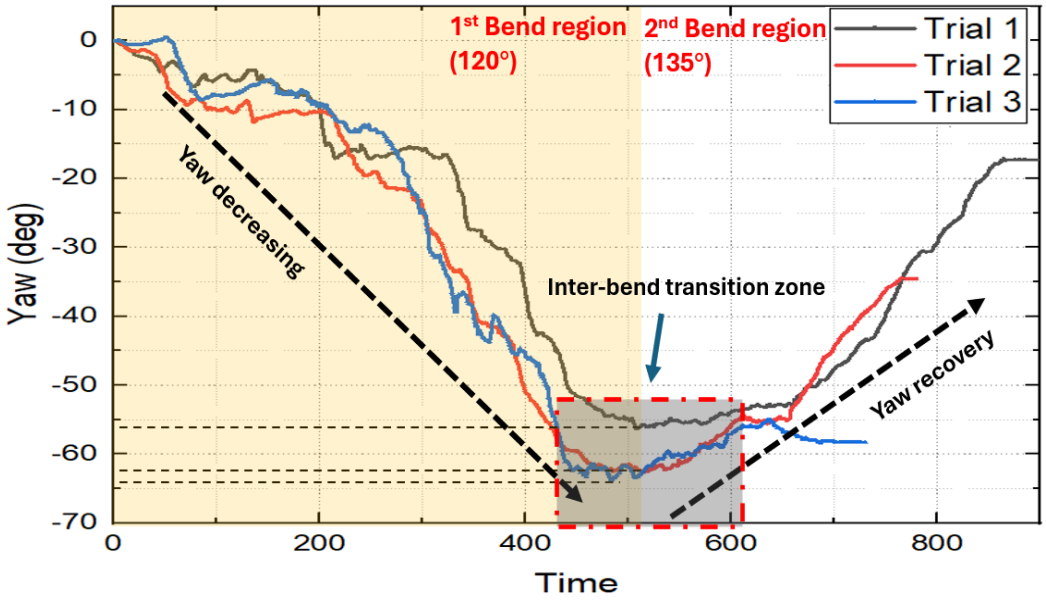


Figure 5.14. Yaw angle evolution during navigation through a continuous S-shaped duct.

To assess the robot's steering stability under complex multi-curvature ducts, the robot was tested in a continuous S-shaped flexible duct consisting of a 120° right bend followed by a 135° left bend. The corresponding yaw-time data from three selected trials are shown in Figure 5.14.. Three repeated trials (black, red, and blue) are shown. The motion comprises a yaw-decreasing phase in the first bend, an inter-bend transition zone, and a yaw recovery phase in the second bend. Trials 1 and 2 demonstrate stable and repeatable steering performance, while Trial 3 (blue) exhibits incomplete yaw recovery, suggesting reduced traction and limited curvature adaptability.

All trials exhibit a consistent two-phase steering pattern: a yaw-decreasing stage during the first bend, an inter-bend transition region where the yaw angle remains nearly constant ( approximately -60°), and finally a yaw-recovery phase as the robot enters the second bend.

In Trial 1 (black) and Trial 2 (red), the robot successfully completed both bends with smooth transitions between phases. The yaw angle decreased by approximately 55- 65° in the first bend and then recovered symmetrically during the second bend, indicating effective hydraulic reconfiguration and stable wall contact. In contrast, Trial 3 (blue) represents a continuous steering failure case: the yaw angle remained nearly constant after the transition zone, and the robot did not achieve full orientation recovery. This incomplete steering is attributed to traction loss and delayed hydraulic response, likely caused by slippage and flexible duct deformation between the bends.

Overall, these results demonstrate that the proposed force steering mechanism can achieve stable consecutive steering under most conditions, while occasional failures highlight the sensitivity of continuous steering to local friction variations, duct elasticity, and the timing of hydraulic input (track-adjustment).

### 5.4.4 Dynamic response analysis based on IMU measurements

To analyse the robot's dynamic response during steering, both yaw angle and three-axis free acceleration were recorded simultaneously by the head-mounted IMU at 15 Hz. Figure 5.15. shows the time evolution of the yaw angle (top) and the corresponding free accelerate (FreeAcc) components (X, Y, Z) during navigation through a continuous S-shaped duct.

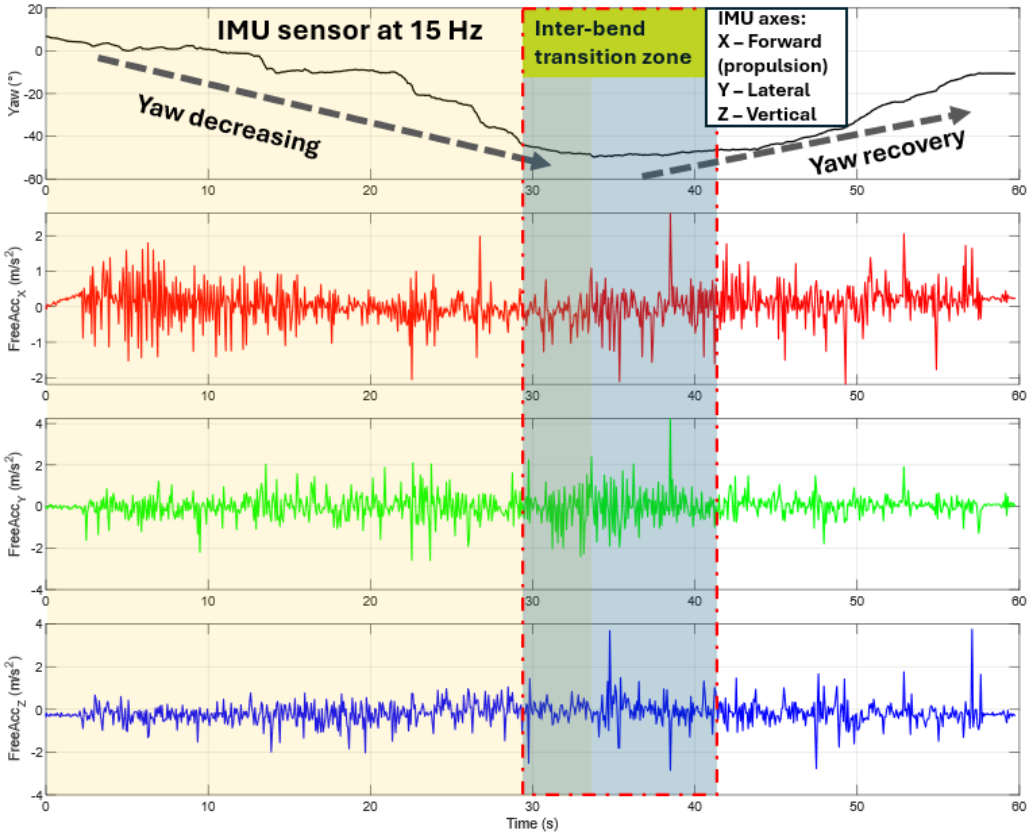


Figure 5.15. Correlation between yaw angle and three-axis free acceleration during S-shaped bend navigation.

Figure 5.15 shows the robot's yaw angle and the three components of linear acceleration (FreeAcc-X, FreeAcc-Y, and FreeAcc-Z) recorded by the IMU sensor at 15 Hz during navigation through a continuous S-shaped duct. The yaw angle decreases as the robot enters the bend and recovers upon exiting, reflecting the turning behaviour. The shaded region indicates the inter-bend transition zone, corresponding to a short straight segment between two curved ducts. The axes follow the IMU coordinate system: X represents the forward

(propulsion) direction, Y the lateral direction, and Z the vertical direction. The IMU signals are presented without filtering to avoid introducing signal distortion and to preserve the original sensor measurements, ensuring consistent interpretation of the experimental data.

The three acceleration signals correspond well to these phases:

Freeacc-X (red) represents acceleration in the robot's forward direction. It shows regular fluctuations during the first bend, suggesting periodic changes in traction as the tracks alternately engaged with the wall. Near the transition zone, several sharp peaks appear, indicating brief slip or re-contact events as the robot switched curvature. Afterward, the signal becomes smoother, showing that forward propulsion recovered and became stable.

FreeAcc-Y (green) corresponds to the lateral acceleration directed toward the duct wall, which indirectly reflects variations in wall contact and normal pressure. During turning, the asymmetric contact between the inner and outer tracks generates differential normal forces, resulting in small lateral reactions that appear as periodic oscillations in FreeAcc-Y. These oscillations therefore indicate alternating increases and decreases in wall contact pressure as the robot body adjusts its position within the bend. The strongest fluctuations occur in the transition zone, corresponding to temporary loss and re-establishment of wall contact. Once the robot entered the second bend, the oscillation amplitude decreased, suggesting that wall contact became stable again.

Freeacc-Z (blue) represents vertical acceleration. Although smaller in magnitude, several noticeable peaks appear near the transition zone, suggesting small vertical vibrations or elastic rebound of the flexible duct as the robot adjusted its position.

Overall, the figure shows that the yaw angle describes the robot's turning motion, while the three-axis accelerations reveal how forces and body posture changed during the process. These reflect the whole process of the robot from instability to re-stability in the curve. It also strongly proves that the expansion mechanism based on hydraulic control plays an important role in realizing the steering function.

### 5.5 Discussion

The steering mechanism proposed in this work is fundamentally governed by the generation of traction imbalance through differential normal force modulation. While the simplified model presented the primary relationship between normal force distribution and yaw moment, it does not fully account for several factors that influence the dynamic behaviour of the system.

In particular, the generation and maintenance of differential traction depend critically on sustained contact between the tracks and the surrounding wall. Variations in environmental compliance, surface friction, and local geometry can affect the effective transmission of forces. In addition, the robot's mass and inertia introduce dynamic effects that influence how the yaw motion evolves over time, especially during transient conditions.

Furthermore, the flexible shaft transmission and hydraulic actuation introduce additional compliance and delay, which may affect the responsiveness and controllability of the steering behaviour. As a result, the system does not operate as a conventional differential drive with precise trajectory tracking capability. Instead, it produces a controllable directional bias that enables the robot to adaptively navigate within confined and deformable environments.

These considerations highlight that the proposed steering mechanism is best understood as a force-mediated navigation strategy, where motion emerges from interaction with the environment rather than strict kinematic control. Future work may incorporate more detailed dynamic modelling or closed-loop control strategies to improve trajectory predictability.

The experimental results demonstrate that the proposed force differential steering mechanism enables effective control of the robot's traction and orientation in curved ducts. Both the force characterization and IMU-based measurements confirmed that asymmetric traction force input generates measurable yaw torque through redistribution of wall-contact pressure. This validates the theoretical assumption that syringe-based expansion mechanism can produce steering moments without requiring differential drive or active bending joints.

In the force characterization tests, retracting one track reduced the overall traction by about 20-25%, confirming that local pressure reduction weakens the tangential force on that side and induces yaw torque. The normal-force measurements revealed a near-linear correlation between syringe input and wall-press force, confirming the controllability of the hydraulic expansion mechanism, although the magnitude was lower than theoretical predictions due to duct deformation and fluid leakage.

The IMU-based steering experiments further verified the practical performance of this mechanism. In the 120° bend, active hydraulic steering produced faster yaw increase and complete curve traversal, whereas passive motion stalled before achieving full rotation. The 90° bend tests revealed that higher wall friction facilitated stronger traction coupling and larger yaw response, while low friction caused delayed turning and smaller steady-state angles. In the continuous S-shaped path, the robot maintained stable motion through consecutive

curvature reversals in most cases, except for one trial where insufficient yaw recovery indicated partial steering failure due to traction loss.

In addition to yaw motion, the IMU-recorded three-axis accelerations provide valuable insight into the robot's dynamic response during turning. The three components: Freeacc-X (tangential), Freeacc-Y (lateral), and Freeacc-Z (radial), which describe how propulsion, wall pressure, and structural vibration interact throughout the motion phases.

Although the steering experiments have demonstrated the feasibility of the proposed force differential mechanism, several limitations remain that affect performance and reproducibility.

The hydraulic system still suffers from response delay and hysteresis, especially during rapid curvature transitions, because of the compressibility of the working fluid and the compliance of the connecting tubing. As a result, part of the input displacement is dissipated before reaching the actuator, leading to an underestimation of the effective wall-press force and reduced control precision.

In addition, deformation of the flexible duct introduces geometric uncertainty: while the elastic wall helps to mimic the physiological behaviour of the colon, its deformation changes the local curvature and wall pressure distribution during motion, complicating the correlation between yaw response and the actual geometry. Such deformation also induces small vertical oscillations of the robot body, which are visible as spikes in the Freeacc-Z signal.

The experimental setup itself also presents constraints: the prototype was tested at a relatively large scale and low speed, so inertial and viscous effects were not fully captured, and the IMU measurements suffered from drift and noise over long runs. Moreover, hydraulic control was performed manually without closed-loop feedback, making it sensitive to operator precision and unable to compensate for transient slip or fluid loss in real time.

Finally, the current test environment cannot fully replicate the compliant, lubricated, and peristaltic nature of real intestinal tissue, limiting physiological accuracy. Besides, In this study, all duct geometries used for steering tests were designed with bending angles greater than 90°. This is because in the preliminary trials showed that when the curvature radius was smaller or the bending angle was below this threshold, the robot could not complete the turn due to the combined constraints of its body length, track configuration, and duct diameter. Therefore, larger bend angles were selected to ensure sufficient space for traction development and to better evaluate the effectiveness of the hydraulic steering mechanism under realistic colon-like conditions.

Future improvements should focus on enhancing hydraulic control precision through closed-loop feedback, miniaturizing the actuation components, and employing more realistic colon simulators or biological tissue models to evaluate steering performance under physiologically relevant conditions.

### 5.6 Summary

This chapter presented a comprehensive set of experiments conducted to validate the performance of the proposed track-based robotic colonoscope with a force differential steering mechanism. The experiments covered mechanical characterization, propulsion and traction analysis, steering performance evaluation, and dynamic response measurement.

The results demonstrated that the robot can effectively adapt to variable lumen diameters and navigate through curved, colon-like ducts with high stability and repeatability. Force characterization experiments confirmed that asymmetric hydraulic input enables controllable wall-press adjustment, leading to measurable yaw torque generation. The IMU-based steering experiments in 90°, 120°, and continuous S-shaped ducts verified that active hydraulic control significantly improves steering smoothness, directional accuracy, and success rate compared to passive motion.

Furthermore, the multi-axis acceleration analysis revealed the coupling between hydraulic actuation and dynamic stability, showing that curvature transitions involve temporary load redistribution followed by rapid mechanical recovery. Overall, the experimental outcomes validated the theoretical models established in previous chapters and demonstrated the feasibility of the proposed force differential mechanism for adaptive steering in confined, flexible environments. Nevertheless, challenges such as hydraulic hysteresis, tubing compliance, and flexible duct deformation remain and will require improvements in control precision and structural integration.

These findings lay the groundwork for future development toward a miniaturized, sensor-integrated, and autonomous robotic colonoscope capable of safe and efficient navigation in realistic biological settings.

# 6 Discussion

This chapter provides a critical discussion of the design choices, experimental findings, and underlying physical mechanisms of the proposed robotic system. Rather than presenting additional results, the purpose of this chapter is to interpret how and why the system performs as observed, and to assess the strengths and limitations of the proposed approach in relation to the research objectives.

The discussion is structured to reflect the key components of the system, including the expansion mechanism, structural design, steering strategy, and control architecture. For each aspect, the analysis focuses on three questions: (1) what has been improved compared to the initial design or existing approaches, (2) what physical mechanisms explain the observed behaviour, and (3) what limitations remain and how they affect the applicability of the system.

Through this analysis, the chapter aims to connect the experimental observations with the underlying engineering principles, providing a deeper understanding of the proposed system and its potential for future development.

This thesis focused on the design, development, and experimental evaluation of a track-based robotic colonoscope capable of adapting its shape and actively steering within tortuous intestinal environments. The work was motivated by the inherent challenges in conventional colonoscopy, such as excessive friction, and difficulty navigating sharp bends, etc. To address these problems, a series of bio-inspired mechanical and hydraulic innovations were proposed and experimentally validated.

The study progressed through five main stages: (1) establishing the design objectives and performance criteria based on clinical and colon anatomy constraints; (2) developing the first prototype using a pneumatic bellows expansion mechanism and silicone tracks; (3) identifying the limitations of the initial design through propulsion and traction experiments; (4) developing an improved second prototype featuring a syringe-driven hydraulic expansion system; and (5) demonstrating active steering capability via force differential control in curved ducts.

### 6.1 Discussion on expansion mechanisms: from pneumatic bellows to hydraulic syringes

In the first design, a dual-hardness silicone bellows was used to suppress undesired radial deformation. The harder outer layer increased axial stiffness, while the softer inner layer preserved radial compliance. The structure allowed about 10 mm axial deformation and limited radial deformation of up to 5 mm. However, experiments showed that this approach only

partially reduced instability. Owing to the flexible corrugated shell, the bellows deformation depended strongly on boundary conditions and dynamic loading, resulting in asymmetric expansion during motion.

During locomotion, tangential friction between the tracks and the tube wall acted directly on the bellows surface, resulting in lateral bending and localized structural collapse of the corrugations. Consequently, internal pressure became uneven, leading to fluctuations in the normal force applied to each track. Even under identical input pressure, the expansion varied with posture, friction, and previous deformation cycles. This path-dependent behaviour made the pneumatic bellows inherently unstable as an expansion actuator for continuous locomotion.

In contrast, the syringe-based hydraulic actuator isolates the expansion mechanism from external disturbances. The rigid cylinder maintains geometric stability, and the pressure transmission depends solely on fluid displacement. The hydraulic expansion mechanism responds to syringe displacement or fluid pressure changes, ensuring stable normal-force generation by compensating for variations in wall contact and torsional loads. The hydraulic system therefore achieves higher reliability, faster response, and continuous traction force. Experiments within a 900 mm duct showed a response delay of about 0.4 s (as shown in Figure 4.14), and a peak track stress of 6 N, significantly higher than the 3.7 N of the bellows system, indicating improved traction capability. The second robot achieved an expanded diameter range of 95-160 mm, compared with 99.6-151.6 mm in the first prototype, representing a 25% increase in adaptability to lumen size variations

Despite these advantages, several limitations remain. The hydraulic transmission introduces viscous damping and time lag due to tubing compliance and small chamber volume, particularly at higher actuation frequencies. The rigid syringes and fittings hinder further miniaturization, as they occupy considerable space and mass. Moreover, the system operates under open-loop control, with no feedback on wall pressure or contact force; variations in temperature, viscosity, or minor leakage can cause pressure drift over time. Finally, using water as the working fluid raises issues of microbubble formation, evaporation, and sealing, all of which affect long-term stability. Future development will require compact, feedback-integrated, and sealed hydraulic modules to support fully autonomous operation.

### 6.2 Structural optimization and stability enhancement

In the original prototype, the internal layout and transmission arrangement resulted in unbalanced torque reactions during motion. The flexible shaft, which transferred power from

the external motor to the internal worm gear, generated a counter-torque around the central axis whenever the robot accelerated or decelerated. Because the structural support around the front section was relatively compliant, this reaction torque caused the robot head to deviate from the intended axis and occasionally produced a shaft oscillations or uncontrolled movements. The effect was particularly pronounced when the tracks encountered uneven contact conditions or friction asymmetry within the duct. This mechanical instability not only reduced propulsion efficiency but also affected sensing accuracy during steering experiments.

The second prototype enhanced structural symmetry and torsional stiffness through the reconfigured internal frame. The transmission shaft was shortened and supported by precision micro-bearings to minimize lateral deflection and vibration. These rolling elements reduced friction and ensured smoother, quieter operation. Tests across three tube diameters demonstrated clear performance gains: the optimized prototype achieved average propulsion force of 3.4 N at 120 mm, 4.2 N at 140 mm (46% higher than 2.8 N), and 3.7 N at 150 mm (23% higher than 3 N), better than previous flexible shaft-worm designs such as [35] (1.4 N) and [27] (approximately 2 N). This confirms that improving track structure and the expansion mechanism significantly enhances adaptability and traction.

Rolling bearings were also integrated between the body and track modules to replace partial sliding interfaces, reducing frictional loss and wear while maintaining alignment during propulsion. Quick-release fixtures further simplified assembly and ensured consistent positioning, improving repeatability across tests. Overall, these modifications improved mechanical stability, reduced energy loss, and ensured reliable motion tracking.

Nevertheless, practical limitations still remain. FDM 3D printing enabled rapid prototyping but introduced dimensional tolerances and layer-based surface roughness that affected assembly accuracy, as shown in Figure 6.1. Small deviations accumulated during assembly, causing misalignment between the worm axis, tracks, and expansion chambers, leading to uneven loading and increased internal friction during operation.

Figure 6.1. Layered surface texture of the 3D-printed (FDM) part.

Another limitation of the earlier design was insufficient overall rigidity. The printed polymer frame and modular joints exhibited elastic deformation when subjected to propulsion and torsional loads. The lack of torsional stiffness also amplified reaction torque transmitted through the flexible shaft, further destabilizing the motion. The connection between modules relied largely on press-fit and adhesive bonding, which provided limited precision and long-term stability. After repeated experiments, local loosening and wear were observed, particularly around the worm housing and track supports. These changes altered the preload conditions of the bearings and contact surfaces, producing variable friction levels and inconsistent propulsion performance across trials.

### 6.3 Discussion on steering performance and force differential steering

The steering experiments demonstrated that force differential control substantially improved the robot's ability to navigate curved ducts. Without active steering, uniform wall contact led to delayed yaw response, intermittent detachment, and strong acceleration oscillations caused by inner-wall sliding and fluctuating traction. With differential actuation, one side of the expansion unit was retracted to reduce wall pressure while the opposite side maintained contact, generating a yaw torque that enabled smooth, continuous turning. IMU yaw data showed monotonic angular change, and the FreeAcc-Y oscillations decreased after the mid-bend, indicating stabilized wall contact.

Mechanically, effective steering requires balancing contact stability and yaw torque. Excessive retraction reduces propulsion efficiency, while insufficient retraction yields weak steering. The results also reveal the transient characteristics of wall-track interaction during steering, involving alternating phases of slip, adhesion, and reattachment influenced by wall curvature

and friction asymmetry. Compared with other size-adaptive robots such as [23], which employed multi-hardness silicone tracks and achieved a propulsion force only 2.2 N, the present TPU-track design reached 6 N under similar conditions. Considering the different geometric dimensions, this improvement can be attributed to the enhanced traction of the TPU materials and the potentially larger effective contact region of the present design. A quantitative analysis of this contact interaction will be addressed in future work to substantiate the observed performance differences. This improvement confirms that TPU provides more consistent friction and better load transfer than multi-layer silicone, enhancing directional stability and preventing sudden skidding during curvature transitions.

Despite these encouraging results, several limitations remain. The current steering actuation is open-loop controlled and relies on manual timing of hydraulic input. Without real-time feedback on contact force or yaw rate, the control accuracy is limited, especially in complex or multi-bend environments. Furthermore, the steering torque is indirectly generated through asymmetric friction, and its magnitude is constrained by the available wall pressure and friction coefficient. Incorporating pressure sensors or IMU-based feedback in future designs would enable closed-loop control, improving precision and adaptability in dynamic environments.

### 6.4 Hydraulic response and limitation

Air is simple to handle but highly compressible, resulting in large delays and weak output stiffness. Water provides much more stable force control but gradually forms microbubbles after several cycles and is prone to small leaks if the seals are imperfect. Other fluids, such as low-viscosity silicone oils, glycerol-water mixtures, or polyethylene-glycol solutions, might combine low compressibility with reduced leakage risk. However, these alternatives have not yet been tested, and their performance remains to be verified in future work.

A further weakness lies in the way the hydraulic lines are connected. Most of the tubing joints are bonded using adhesive. Although this method simplifies assembly, it prevents inspection or rework once the system is sealed. Minor leaks may appear after several test sessions, and they are difficult to locate because the joints are opaque and non-detachable. Such small leaks can gradually alter the pressure, displacement relationship of the system without producing obvious visual signs. In practice, this limitation makes it difficult to maintain consistent experimental conditions and to compare data across trials.

To address these issues, a more serviceable connection scheme is required. Replacing adhesive joints with detachable fittings would make leak detection and maintenance more convenient.

Luer-lock connectors, small barbed fittings with clamps, or miniature push-to-connect couplers could be used depending on tube size and stiffness. Adding a small manifold between the master syringe and the four branch lines would allow pressure measurement, isolation of each channel, and controlled leak testing. The use of transparent tubing and colour coding would make air bubbles and leaks easier to identify, while short straight sections before each track module could serve as visual inspection windows. A simple pressure-decay or bubble-formation test performed before each experiment would provide a quick verification of system integrity.

### 6.5 Discussion on current open-loop control system

At the present stage, the entire actuation system of the robot operates in an open-loop manner. The driving input to the hydraulic system can either be a preset displacement of the master syringe or a manually adjusted stroke determined by the operator during testing. In practice, the experimenter observes the robot's behaviour in real time and modifies the input based on visual judgment of expansion or contact conditions. This approach allows flexible testing and quick manual intervention, but it also means that the control relies heavily on the operator's experience rather than quantitative feedback.

Because the actuation is not linked to any sensor measurement, the system does not monitor the actual wall pressure, track deformation, or bending angle. As a result, the effective wall force depends on several uncertain factors, including fluid compressibility, tubing compliance, and small variations in temperature or leakage. Over the course of repeated tests, these factors cause gradual drift between the commanded syringe stroke and the actual output force. Since no pressure or displacement sensors are installed near the expansion chambers, it is impossible to correct this drift automatically, and the same command may generate different wall pressures at different times.

The same limitation applies to steering. The differential actuation between the left and right sides is triggered manually, based on the operator's visual observation of the robot entering a bend. Although this method works for qualitative assessment, it introduces variability in timing and intensity of hydraulic retraction. In some trials, one side of the system responds faster than the other, leading to inconsistent yaw behaviour. The turning motion thus depends not only on the mechanical asymmetry produced by the hydraulic system but also on the human response time and subjective decision of the operator.

This open-loop and observer-dependent control simplifies the hardware design and has been adequate for basic functional verification. However, it inherently limits precision, repeatability, and safety. Without pressure feedback, the system cannot prevent overexpansion or under actuation, and the results between experiments remain operator-dependent. These limitations will become increasingly significant when the robot is required to perform autonomous or long-duration tasks.

### 6.6 Discussion on geometric and experimental constraints

One of the most significant current limitations of the proposed robotic system lies in its overall size. Although the existing prototype successfully demonstrated the fundamental principles of hydraulic expansion, track traction, and differential steering, the robot remains too large to be introduced into a real colon or anatomical model of comparable scale. The prototype measures approximately 80 mm in length, with an expandable outer diameter ranging from 95 to 160 mm. These dimensions exceed the physiological range of the human colon, whose inner diameter typically varies between 26 and 45 mm with the average rate of colon diameter change is about 73% [9][10]. The prototype [23] with the same function of size-adapting can realize the size change from 65 to 110 mm, and the expansion rate is about 69.2 %, which is almost same from the expansion rate of this prototype (68.4 %), but it is still less than the change rate of colon diameter.

Considerable effort has been made to reproduce the main physical properties of the intestinal environment, including the use of curved acrylic or silicone tubes, lubricated inner walls, and varying curvature radii. These setups provide valuable insight into propulsion and steering behaviour under confined conditions, but they cannot fully replicate the deformable, viscoelastic, and moisture-saturated nature of the real colon. In particular, the rigid test ducts used in most trials do not respond to wall pressure or deformation in the same way as living tissue, which limits the biological relevance of the measured forces and contact distributions. Consequently, while the mechanical feasibility of the design has been validated, its physiological reliability and safety still remain to be demonstrated.

The large size of the current prototype is mainly due to the use of externally mounted actuators and transmission components. In addition, the current scale provides mechanical advantages, as both traction force and steering torque increase with system size, with torque scaling quadratically with the characteristic length, ensuring sufficient propulsion and steering capability in the present experiments. It should be noted that while the scaling relationships are primarily governed by the overall robot size, the achievable pressure and thus the actual force

output are constrained by the hydraulic actuation system, including syringe dimensions and fluid transmission characteristics. The scaling relationships can be interpreted as follows. As the system size increases, the contact area between the robot and the surrounding wall increases, leading to higher normal force and thus improved traction capability. At the same time, the steering torque increases more rapidly, as it depends on both the generated force and the lever arm, resulting in significantly enhanced steering performance at larger scales.

In contrast, when the system is miniaturised, both traction force and steering torque decrease, with torque reducing more rapidly. This leads to insufficient propulsion and limited steering authority, which become critical constraints for small-scale implementations. For the hydraulic system, the operating pressure remains approximately unchanged with scaling, while the flow rate increases with system size. As a result, larger systems tend to exhibit slower dynamic response, whereas smaller systems respond faster but may become more sensitive to disturbances and system imperfections.

The external motor, flexible shaft, and syringe assembly were designed to simplify testing and measurement, but they also impose constraints on miniaturization. Reducing the overall diameter will require an integrated design that embeds the power source, valves, and hydraulic channels within the robot body. This transition will inevitably involve redesigning the internal frame, adopting smaller drive mechanisms, and using lightweight materials to maintain structural strength while minimizing bulk. Furthermore, miniaturization will need to consider fabrication precision, sealing reliability, and manufacturing repeatability at smaller scales.

From a clinical perspective, patient discomfort is closely related to excessive wall pressure, localized stress concentration, and the stiffness of components interacting with the intestinal wall. In the current prototype, discomfort is not evaluated directly but can be indirectly inferred from measurable mechanical parameters such as normal contact force and traction force.

The proposed hydraulic expansion system enables controlled regulation of wall pressure, which helps to avoid excessive loading while maintaining sufficient traction. However, relatively stiff components, including the flexible shaft and hydraulic tubing, may introduce localized rigidity that could affect comfort in a real biological environment. In addition, the force-differential steering method generates asymmetric wall interaction, which may result in localized pressure variations during turning.

It should be noted that the present evaluation is limited to benchtop experiments using rigid or semi-compliant ducts, and therefore does not fully represent the viscoelastic properties of real

intestinal tissue. Future work should include more clinically relevant evaluation methods, such as pressure distribution sensing, testing with soft biological phantoms, and ultimately in-vivo validation under controlled conditions.

### 6.7 Chapter summary

Despite the encouraging results obtained from the improved track-based robotic colonoscope, several limitations remain in the current design and validation process.

First, the hydraulic expansion system, although more stable than the pneumatic bellows, still exhibits transmission delay and hysteresis due to the compliance of the tubing and the compressibility of the working fluid. The current setup uses only air and water as actuation media, and other fluids with better damping or sealing properties have not yet been tested. Furthermore, most of the hydraulic connections are bonded with adhesive, which makes it difficult to inspect, repair, or locate small leaks during long-term use.

Second, the structural framework is mainly fabricated by FDM 3D printing. The limited precision of this process leads to cumulative alignment errors between modules, local deformation under load, and reduced rigidity of the overall assembly. These effects contribute to minor but measurable deviations in propulsion direction and force transmission.

Third, the control architecture remains fully open-loop. The actuation input is either preset or manually adjusted by the operator based on visual observation, without any real-time feedback on wall pressure or steering angle. This operator-dependent control introduces variability between tests and prevents consistent quantitative evaluation.

Fourth, the size of the current prototype exceeds the scale of the human colon. Although the artificial ducts used in experiments successfully simulate curvature and frictional characteristics, they cannot reproduce the compliant, viscoelastic, and fluid-rich nature of biological tissue. Consequently, the experimental data provide mechanical validation but limited physiological relevance.

Finally, the steering performance is still constrained by asymmetric pressure response and manual timing of hydraulic retraction. The differential torque generated between the tracks is sufficient for controlled turning, yet the precision and repeatability of steering remain restricted by the system’s open-loop nature and hydraulic delay.

# 7 Conclusion and future work

## 7.1 Conclusion

This dissertation presented the design, fabrication, and experimental evaluation of a track-based robotic colonoscope with an adaptive hydraulic expansion mechanism and differential steering capability. The study was motivated by the limitations of conventional colonoscopy, including restricted manoeuvrability, high patient discomfort, and potential tissue overstretching. The primary objective was to develop a robotic system capable of generating controlled wall pressure and traction forces within a confined environment, while maintaining mechanical stability and adaptability to curvature variations.

The research followed a structured path from concept to validation. In the initial stage, a first-generation prototype employing pneumatic bellows and silicone tracks was constructed to verify the basic feasibility of wall-press-based propulsion. This configuration successfully demonstrated the propulsion principle but also revealed several weaknesses: the pneumatic bellows showed nonuniform deformation and slow response, and the silicone tracks exhibited limited wear resistance and inconsistent traction. These findings underscored the need for both mechanical and material optimization.

To address these issues, a second prototype was developed with significant improvements in structural design and material configuration. The pneumatic system was replaced with a syringe-driven hydraulic expansion mechanism to achieve finer control of wall pressure and faster actuation response. In parallel, the robot's overall structure was re-engineered to improve stiffness, geometric alignment, and ease of maintenance. The introduction of micro-bearings reduced friction between internal moving parts, while modular quick-release joints simplified assembly and ensured repeatable experimental setup. Material selection was also optimized, focusing on components that combined flexibility with sufficient mechanical strength to maintain wall contact without deformation or slippage. These design refinements collectively enhanced propulsion stability, reduced vibration, and improved the durability of the robot under repeated testing.

A comprehensive set of experiments was conducted to characterize the performance of the improved system. Force measurements confirmed that the hydraulic expansion mechanism could generate stable and adjustable normal forces. Dynamic tests revealed the presence of response delay and hysteresis caused by the elasticity of the tubing and compressibility of the working fluid. Steering experiments verified that force differential control produced

measurable yaw torque, enabling smooth navigation in curved ducts. IMU data analysis confirmed that steering performance correlated with the asymmetric wall pressure applied to the tracks, validating the proposed control principle. The optimized structure also effectively suppressed unwanted vibration and head oscillation during propulsion, demonstrating clear improvement over the first-generation model.

Although the robot has demonstrated the feasibility of hydraulic wall-press actuation and controllable steering, several limitations remain. The hydraulic transmission still suffers from pressure lag, limited bandwidth, and susceptibility to air inclusion. The control strategy is fully open-loop, with actuation either preset or manually adjusted by the operator based on observation, which limits consistency and precision. The prototype's size remains larger than physiological dimensions, preventing in-vivo or anatomically scaled testing. Furthermore, the rigid artificial ducts used in experiments cannot replicate the compliant and viscoelastic characteristics of real intestinal tissue, reducing the biological relevance of the results. Finally, the 3D-printed polymer frame, while sufficient for prototyping, provides limited dimensional accuracy and rigidity, leading to small alignment errors between modules.

Despite these constraints, the work has established a clear mechanical and experimental foundation for adaptive wall-press robotic locomotion. The research demonstrates that combining track-based propulsion with controlled hydraulic expansion provides an effective and mechanically simple strategy for navigating complex, curved pathways. The developed platform offers valuable insight into the interplay between structure, actuation, and material performance in confined environments.

### 7.2 Summary of contributions

This dissertation presents the design, modelling, and experimental validation of a track-based robotic colonoscope with adaptive hydraulic expansion and differential steering capability. The main research contributions are summarized as follows.

First, a force-differential steering strategy based on selective track disengagement is proposed. By actively reducing the normal contact force on selected tracks through hydraulic actuation, a traction imbalance is generated, producing a controllable yaw moment. This approach enables steering without relying on differential speed control or distal articulation, and its feasibility has been demonstrated experimentally in curved ducts using IMU-based measurements.

Second, a syringe-driven hydraulic expansion system is developed to provide continuous and controllable regulation of radial contact force. Compared with the initial pneumatic bellows

design, the hydraulic system achieves improved stability, faster response, and more consistent force transmission. This mechanism enables reliable wall-pressure generation and supports anchoring, propulsion, and steering within a unified actuation framework.

Third, a hybrid actuation system is established by integrating motor-driven propulsion with hydraulically controlled contact modulation. This configuration enables independent control of axial locomotion, yaw steering, and radial expansion. By explicitly linking actuator inputs to functional degrees of freedom, the work provides a system-level framework for understanding how coordinated actuation can generate controlled motion in confined and compliant environments.

Finally, a set of quantitative performance metrics is defined to evaluate robotic colonoscope systems, including traction force, propulsion speed, steering capability, and contact stability. These metrics are supported by a comprehensive experimental framework combining force measurement, IMU tracking, and theoretical modelling, enabling consistent evaluation and comparison with future designs.

Overall, this work establishes both theoretical and experimental foundations for force-mediated locomotion and steering in constrained environments, and provides a basis for the future development of adaptive and miniaturized robotic colonoscopy systems.

### 7.3 Future work

Future work will focus on improving controllability, miniaturization, and physiological validation, following the directions outlined below.

(1) Miniaturization and system integration

The current prototype is larger than the human colon, which limits realistic testing. Future designs will focus on reducing the overall diameter and integrating actuation and sensing components into the robot body. This will involve redesigning the internal frame to maintain stiffness while reducing bulk, adopting lightweight composite materials, and embedding micro-hydraulic channels and valves. Compact internal actuators or distributed hydraulic chambers may replace the external motor and flexible shaft to achieve a self-contained architecture suitable for in-vitro and preclinical experiments.

(2) Improvement of the hydraulic transmission system

The syringe-driven hydraulic mechanism, while effective, still exhibits response delay, hysteresis, and limited maintenance accessibility. Future versions should employ detachable

fittings for all non-permanent connections to allow easy inspection and replacement. Incorporating micro-pressure sensors near each expansion unit will enable real-time monitoring and calibration of wall pressure. Moreover, alternative working fluids, such as: low-viscosity silicone oil or glycerol-water mixtures, should be explored to reduce compressibility and air entrainment. Establishing a standardized leak detection and calibration protocol will further improve system repeatability.

(3) Transition from open-loop to closed-loop control

Current experiments rely on manually adjusted open-loop inputs, which limit precision and repeatability. The next stage will involve developing a closed-loop control framework that integrates real-time feedback from pressure sensors, IMU-based yaw tracking, and syringe-position encoders. A proportional or PID controller could be implemented to regulate wall pressure and steering angle automatically. The combination of force feedback and orientation sensing will allow consistent, safe, and semi-autonomous operation during propulsion and turning.

(4) Refinement of theoretical modelling and dynamic analysis

The existing analytical model describes static relationships between wall pressure, traction, and yaw torque. Future modelling work should extend this framework to include dynamic effects, fluid transmission delay, and contact hysteresis. Integrating time-dependent behaviour into the simulation will allow better prediction of system response under fast actuation or continuous motion. Experimental data from pressure and motion sensors can be used to identify parameters and validate the extended model.

(5) Experimental validation in realistic environments

All current experiments have been performed in rigid or semi-rigid artificial ducts. The next step will involve testing in compliant and lubricated colon-like models that mimic the viscoelastic and deformable properties of biological tissue. In-vitro experiments using ex-vivo colon samples will further assess the robot's safety, adaptability, and navigation capability under near-physiological conditions. Such validation will be essential for bridging the gap between mechanical feasibility and clinical applicability.

(6) Toward clinical readiness and safety evaluation

In the long term, the robot's mechanical design and control architecture should be refined for clinical safety. Studies will focus on limiting maximum wall pressure, developing fail-safe

actuation mechanisms, and assessing long-term reliability under repeated operation. Collaborations with medical experts will be necessary to define acceptable force limits and evaluate biocompatibility of materials. These steps will form the foundation for preclinical animal trials and eventual clinical translation.

In summary, future work will aim to transform the current laboratory prototype into a miniaturized, sensor-integrated, and feedback-controlled system capable of navigating compliant biological pathways safely and autonomously. Achieving these goals will mark a substantial step toward practical robotic colonoscopy.

# Reference

[1] Luengo-Fernandez, R., Leal, J., Gray, A., & Sullivan, R. (2013). Economic burden of cancer across the European Union: a population-based cost analysis. *The lancet oncology*, *14*(12), 1165-1174.

[2] Hofmarcher, T., Lindgren, P., Wilking, N., & Jönsson, B. (2020). The cost of cancer in Europe 2018. *European Journal of Cancer*, *129*, 41-49.

[3] Astin, M., Griffin, T., Neal, R. D., Rose, P., & Hamilton, W. (2011). The diagnostic value of symptoms for colorectal cancer in primary care: a systematic review. *The British Journal of General Practice*, *61*(586), e231.

[4] Santucci, N. R., & Velez, A. (2024). Physiology of lower gastrointestinal tract. *Alimentary Pharmacology & Therapeutics*, *60*, S1-S19.

[5] Fisher, D. A., Maple, J. T., Ben-Menachem, T., Cash, B. D., Decker, G. A., Early, D. S., ... & Dominitz, J. A. (2011). Complications of colonoscopy. *Gastrointestinal endoscopy*, *74*(4), 745-752.

[6] Dominitz, J. A., Eisen, G. M., Baron, T. H., Goldstein, J. L., Hirota, W. K., Jacobson, B. C., ... & Standards of Practice Committee. (2003). Complications of colonoscopy. *Gastrointestinal endoscopy*, *57*(4), 441-445.

[7] Santucci, N. R., & Velez, A. (2024). Physiology of lower gastrointestinal tract. *Alimentary Pharmacology & Therapeutics*, *60*, S1-S19.

[8] Ellis, H., & Mahadevan, V. (2014). Anatomy of the caecum, appendix and colon. *Surgery (Oxford)*, *32*(4), 155-158.

[9] Eickhoff, A., et al., Colon anatomy based on CT colonography and fluoroscopy: Impact on looping, straightening and ancillary manoeuvres in colonoscopy. Digestive and Liver Disease, 2010. 42(4): p. 291-296.

[10] Alazmani, A., Hood, A., Jayne, D., Neville, A., & Culmer, P. (2016). Quantitative assessment of colorectal morphology: Implications for robotic colonoscopy. Medical engineering & physics, 38(2), 148-154.

[11] Marchesini, R., et al., Ex-Vivo Optical-Properties of Human Colon Tissue. Lasers in Surgery and Medicine, 1994. 15(4): p. 351-357.

[12] Wang, K.D. and G.Z. Yan, Research on measurement and modelling of the gastro intestine's frictional characteristics. Measurement Science and Technology, 2009. 20(1): p. 015803.

[13] Wang, Z., Emmerich, A., Pillon, N. J., Moore, T., Hemerich, D., Cornelis, M. C., ... & Ameur, A. (2022). Genome-wide association analyses of physical activity and sedentary behavior provide insights into underlying mechanisms and roles in disease prevention. *Nature genetics*, *54*(9), 1332-1344.

[14] Chen, J., Ruan, X., Fu, T., Lu, S., Gill, D., He, Z., ... & Li, X. (2024). Sedentary lifestyle, physical activity, and gastrointestinal diseases: evidence from mendelian randomization analysis. *EBioMedicine*, *103*.

[15] Franco, D. L., Leighton, J. A., & Gurudu, S. R. (2017). Approach to incomplete colonoscopy: new techniques and technologies. *Gastroenterology & hepatology*, *13*(8), 476.

[16] Brahmania, M., Park, J., Svarta, S., Tong, J., Kwok, R., & Enns, R. (2012). Incomplete colonoscopy: maximizing completion rates of gastroenterologists. *Canadian Journal of Gastroenterology and Hepatology*, *26*(9), 589-592.

[17] Manfredi, L. (2021). Endorobots for colonoscopy: Design challenges and available technologies. *Frontiers in Robotics and AI*, *8*, 705454.

[18] Winters, C., Subramanian, V., & Valdastri, P. (2022). Robotic, self-propelled, self-steerable, and disposable colonoscopes: Reality or pipe dream? A state of the art review. *World Journal of Gastroenterology*, *28*(35), 5093.

[19] Latos, W., Aebisher, D., Latos, M., Krupka-Olek, M., Dynarowicz, K., Chodurek, E., ... & Kawczyk-Krupka, A. (2022). Colonoscopy: preparation and potential complications. *Diagnostics*, *12*(3), 747.

[20] Dominitz, J. A., Eisen, G. M., Baron, T. H., Goldstein, J. L., Hirota, W. K., Jacobson, B. C., ... & Standards of Practice Committee. (2003). Complications of colonoscopy. *Gastrointestinal endoscopy*, *57*(4), 441-445.

[21] Dario, P., & Mosse, C. A. (2003, September). Review of locomotion techniques for robotic colonoscopy. In *2003 IEEE International Conference on Robotics and Automation (Cat. No. 03CH37422)* (Vol. 1, pp. 1086-1091). IEEE.

[22] Winters, C., Subramanian, V., & Valdastri, P. (2022). Robotic, self-propelled, self-steerable, and disposable colonoscopes: Reality or pipe dream? A state of the art review. *World Journal of Gastroenterology*, *28*(35), 5093.

[23] Consumi, V., Lindenroth, L., Merlin, J., Stoyanov, D., & Stilli, A. (2023). Design and evaluation of the softscreen capsule for colonoscopy. *IEEE Robotics and Automation Letters*, *8*(3), 1659-1666.

[24] He, S., Zhang, Y., Huang, B., Lin, J., Shi, C., & Hu, C. (2024, May). A Track-based Colon Endoscopic Robot with Depth Perception Stereo Cameras for Haustral Fold Detection during Colonic Navigation. In *2024 IEEE International Conference on Robotics and Automation (ICRA)* (pp. 1276-1282). IEEE.

[25] Lee, D., Joe, S., Choi, J., Lee, B. I., & Kim, B. (2016). An elastic caterpillar-based self-propelled robotic colonoscope with high safety and mobility. *Mechatronics*, *39*, 54-62.

[26] Fukunaga, F., & Nagase, J. Y. (2016, June). Cylindrical elastic crawler mechanism for pipe inspection inspired by amoeba locomotion. In *2016 6th IEEE International Conference on Biomedical Robotics and Biomechatronics (BioRob)* (pp. 424-429). IEEE.

[27] Nagase, J. Y., Fukunaga, F., & Ogawa, K. (2018, August). Development of a funicular flexible crawler for colonoscopy. In *2018 7th IEEE International Conference on Biomedical Robotics and Biomechatronics (Biorob)* (pp. 859-864). IEEE.

[28] Formosa, G. A., Prendergast, J. M., Edmundowicz, S. A., & Rentschler, M. E. (2019). Novel optimization-based design and surgical evaluation of a treaded robotic capsule colonoscope. *IEEE Transactions on Robotics*, *36*(2), 545-552.

[29] Kim, D., Lee, D., Joe, S., Lee, B. I., & Kim, B. (2014). The flexible caterpillar based robotic colonoscope actuated by an external motor through a flexible shaft. *Journal of Mechanical Science and Technology*, *28*(11), 4415-4420.

[30] Sliker, L. J., Kern, M. D., Schoen, J. A., & Rentschler, M. E. (2012). Surgical evaluation of a novel tethered robotic capsule endoscope using micro-patterned treads. *Surgical endoscopy*, *26*(10), 2862-2869.

[31] Norton, J., Hood, A., Neville, A., Jayne, D., Culmer, P., Alazmani, A., & Boyle, J. (2016, June). RollerBall: a mobile robot for intraluminal locomotion. In *2016 6th IEEE international conference on biomedical robotics and biomechatronics (BioRob)* (pp. 254-259). IEEE.

[32] Karargyris, A., & Koulaouzidis, A. (2014). OdoCapsule: next-generation wireless capsule endoscopy with accurate lesion localization and video stabilization capabilities. *IEEE transactions on biomedical engineering*, *62*(1), 352-360.

[33] Kang, M., Joe, S., An, T., Jang, H., & Kim, B. (2021). A novel robotic colonoscopy system integrating feeding and steering mechanisms with self-propelled paddling locomotion: A pilot study. *Mechatronics*, *73*, 102478.

[34] M. Quirini, R. J. Webster, A. Menciassi and P. Dario., "Design of a Pill-Sized 12-legged Endoscopic Capsule Robot," *Proceedings 2007 IEEE International Conference on Robotics and Automation*, Rome, Italy, 2007, pp. 1856-1862, doi: 10.1109/ROBOT.2007.363592.

[35] Osawa, K., Nakadate, R., Arata, J., Nagao, Y., Akahoshi, T., Eto, M., & Hashizume, M. (2020). Self-propelled colonoscopy robot using flexible paddles. *IEEE Robotics and Automation Letters*, *5*(4), 6710-6716.

[36] Park, S., Park, H., Park, S., & Kim, B. (2006). A paddling based locomotive mechanism for capsule endoscopes. *Journal of mechanical science and technology*, *20*(7), 1012-1018.

[37] Shikanai, M., Murai, N., Itoh, K., Ishii, H., Akanishi, A. T., Anoue, K. T., ... & Hasizume, M. (2009, September). Development of a robotic endoscope that locomotes in the colon with fle xible helical fins. In *2009 Annual International Conference of the IEEE Engineering in Medicine and Biology Society* (pp. 5126-5129). IEEE.

[38] Mills, G. H., Liu, J. H., Kaddouh, B. Y., Jackson, A. E., & Richardson, R. C. (2018, November). Miniature magnetic robots for in-pipe locomotion. In *Robotics Transforming the Future: Proceedings of CLAWAR 2018: The 21st International Conference on Climbing and Walking Robots and the Support Technologies for Mobile Machines* (pp. 289-300). CLAWAR Association Ltd.

[39] Valdastri, P., Webster, R. J., Quaglia, C., Quirini, M., Menciassi, A., & Dario, P. (2009). A new mechanism for mesoscale legged locomotion in compliant tubular environments. *IEEE Transactions on Robotics*, *25*(5), 1047-1057.

[40] Wang, K. D., & Yan, G. Z. (2008). Research on measurement and modelling of the gastro intestine's frictional characteristics. *Measurement Science and Technology*, *20*(1), 015803.

[41] Wahed, M. A. A., & Arshad, M. R. (2017, October). Wall-press type pipe inspection robot. In *2017 IEEE 2nd International Conference on Automatic Control and Intelligent Systems (I2CACIS)* (pp. 185-190). IEEE.

[42] Kim, Y. J., Yoon, K. H., & Park, Y. W. (2009, July). Development of the inpipe robot for various sizes. In *2009 IEEE/ASME International Conference on Advanced Intelligent Mechatronics* (pp. 1745-1749). IEEE.

[43] Manfredi, L., Capoccia, E., Ciuti, G., & Cuschieri, A. (2019). As oft p neumatic i nchworm d ouble balloon (spid) for colonoscopy. *Scientific reports*, *9*(1), 11109.

[44] Vucelic, B., Rex, D., Pulanic, R., Pfefer, J., Hrstic, I., Levin, B., ... & Arber, N. (2006). The aer-o-scope: proof of concept of a pneumatic, skill-independent, self-propelling, self-navigating colonoscope. *Gastroenterology*, *130*(3), 672-677.

[45] Huan, Y., Ren, X., Firrincieli, A., Manfredi, L., Cianchetti, M., Arezzo, A., ... & Ciuti, G. (2023). Flexible over-the-tube device for soft-tethered colonoscopy. *IEEE/ASME Transactions on Mechatronics*, *29*(3), 1611-1621.

[46] Sugarbaker, P. H., Penland, W. Z., & Lyddy, J. (1985). Pneumatic device for the automated advancement of the fiberoptic endoscope for total colonoscopy—a preliminary report. *Gastrointestinal Endoscopy*, *31*(3), 210-213.

[47] Takamatsu, T., Endo, Y., Fukushima, R., Yasue, T., Shinmura, K., Ikematsu, H., & Takemura, H. (2023). Robotic endoscope with double-balloon and double-bend tube for colonoscopy. *Scientific reports*, *13*(1), 10494.

[48] Glozman, D., Hassidov, N., Senesh, M., & Shoham, M. (2010). A self-propelled inflatable earthworm-like endoscope actuated by single supply line. *IEEE Transactions on Biomedical Engineering*, *57*(6), 1264-1272.

[49] Manfredi, L. (2021, February). A compact control unit for a pneumatic soft colonoscope. In *ACTUATOR; International Conference and Exhibition on New Actuator Systems and Applications 2021* (pp. 1-4). VDE.

[50] Dehghani, H., Welch, C. R., Pourghodrat, A., Nelson, C. A., Oleynikov, D., Dasgupta, P., & Terry, B. S. (2017). Design and preliminary evaluation of a self-steering, pneumatically driven colonoscopy robot. *Journal of medical engineering & technology*, *41*(3), 223-236.

[51] Nguyen, T. T., & Nguyen, D. Q. (2024). Soft robot employing a series of pneumatic actuators and distributed balloons: Modeling, evaluation, and applications. *IEEE Transactions on Robotics*.

[52] Onoe, H., Suzumori, K., & Wakimoto, S. (2008, July). Optimum design of pneumatic multi-chamber rubber tube actuator generating traveling deformation waves for colonoscope

insertion. In *2008 IEEE/ASME International Conference on Advanced Intelligent Mechatronics* (pp. 31-36). IEEE.

[53] Nakamura, T., Hidaka, Y., Yokojima, M., & Adachi, K. (2012). Development of peristaltic crawling robot with artificial rubber muscles attached to large intestine endoscope. *Advanced Robotics*, *26*(10), 1161-1182.

[54] Liu, J., Li, P., & Zuo, S. (2023). Actuation and design innovations in earthworm-inspired soft robots: A review. *Frontiers in Bioengineering and Biotechnology*, *11*, 1088105.

[55] Chen, J., Yang, J., Qian, F., Lu, Q., Guo, Y., Sun, Z., & Chen, C. (2022). A novel inchworm-inspired soft robotic colonoscope based on a rubber bellows. *Micromachines*, *13*(4), 635.

[56] Kim, B., Jeong, Y., Lim, H. Y., Kim, T. S., Park, J. O., Dario, P., ... & Choi, H. (2002, October). Smart colonoscope system. In *IROS* (pp. 1367-1372).

[57] Li, G., Qiu, W., Wang, M., Zhu, Y., & Liu, F. (2024). Development of an earthworm-based soft robot for colon sampling. *Frontiers in Robotics and AI*, *11*, 1309220.

[58] Saga, N. (2004). A prototype of peristaltic robot using pneumatic artificial muscle. *Intelligent autonomous system*, *8*(1), 85-95.

[59] Yanagida, T., Adachi, K., Yokojima, M., & Nakamura, T. (2012, October). Development of a peristaltic crawling robot attached to a large intestine endoscope using bellows-type artificial rubber muscles. In *2012 IEEE/RSJ International Conference on Intelligent Robots and Systems* (pp. 2935-2940). IEEE.

[60] Liu, J., Li, P., Huang, Z., Liu, H., & Huang, T. (2025). Earthworm-Inspired multimodal pneumatic continuous soft robot enhanced by winding transmission. *Cyborg and Bionic Systems*, *6*, 0204.

[61] Das, R., Babu, S. P. M., Visentin, F., Palagi, S., & Mazzolai, B. (2023). An earthworm-like modular soft robot for locomotion in multi-terrain environments. *Scientific Reports*, *13*(1), 1571.

[62] Wang, K., Ma, J., Wang, F., Wang, Z., Yan, G., & Zhou, Y. (2017). Full-driving soft robotic colonoscope in compliant colon tissue. *Journal of medical engineering & technology*, *41*(8), 662-669.

[63] Hasib, S. A., Gulzar, M. M., Oishy, S. R., Maaruf, M., Habib, S., & Shakoor, A. (2025). An investigation of innovative strategies in underwater soft robotics. *Engineering Science and Technology, an International Journal*, *70*, 102123.

[64] Coleman, S. A., Tapia-Siles, S. C., Pakleppa, M., Vorstius, J. B., Keatch, R. P., Tang, B., & Cuschieri, A. (2016). A hydraulically driven colonoscope. *Surgical Endoscopy*, *30*(10), 4515-4524.

[65] Coleman, S. A., Pakleppa, M., & Cuschieri, A. (2021). Hydro-jet propelled colonoscopy: proof of concept in a phantom colon. *Surgical Endoscopy*, *35*(2), 989-995.

[66] Xia, Y., He, Y., Zhang, F., Liu, Y., & Leng, J. (2021). A review of shape memory polymers and composites: mechanisms, materials, and applications. *Advanced materials*, *33*(6), 2000713.

[67] Perera, O., Liyanapathirana, R., Gargiulo, G., & Gunawardana, U. (2024, December). A review of soft robotic actuators and their applications in bioengineering, with an emphasis on HASEL actuators' future potential. In *Actuators* (Vol. 13, No. 12, p. 524). MDPI.

[68] Kim, B., Park, S., & Park, J. O. (2009, July). Microrobots for a capsule endoscope. In *2009 IEEE/ASME International Conference on Advanced Intelligent Mechatronics* (pp. 729-734). IEEE.

[69] Peirs, J., Reynaerts, D., & Van Brussel, H. (1998). Design of a shape memory actuated endoscopic tip. *Sensors and Actuators A: physical*, *70*(1-2), 135-140.

[70] Kadir, M. R. A., Dewi, D. E. O., Jamaludin, M. N., Nafea, M., & Ali, M. S. M. (2019). A multi-segmented shape memory alloy-based actuator system for endoscopic applications. *Sensors and Actuators A: Physical*, *296*, 92-100.

[71] De Sars, V., Haliyo, S., & Szewczyk, J. (2010). A practical approach to the design and control of active endoscopes. *Mechatronics*, *20*(2), 251-264.

[72] Yan, S., Zhang, F., Luo, L., Wang, L., Liu, Y., & Leng, J. (2023). Shape memory polymer composites: 4D printing, smart structures, and applications. *Research*, *6*, 0234.

[73] Heunis, C. M., Wang, Z., de Vente, G., Misra, S., & Venkiteswaran, V. K. (2023). A Magnetic Bio-Inspired Soft Carrier as a Temperature-Controlled Gastrointestinal Drug Delivery System. *Macromolecular bioscience*, *23*(7), 2200559.

[74] Ni, C., Chen, D., Yin, Y., Wen, X., Chen, X., Yang, C., ... & Xie, T. (2023). Shape memory polymer with programmable recovery onset. *Nature*, *622*(7984), 748-753.

[75] Cao, X., Zhang, M., Zhang, Z., Xu, Y., Xiao, Y., & Li, T. (2019). Review of soft linear actuator and the design of a dielectric elastomer linear actuator. *Acta mechanica solida Sinica*, *32*(5), 566-579.

[76] Xu, L., Chen, H. Q., Zou, J., Dong, W. T., Gu, G. Y., Zhu, L. M., & Zhu, X. Y. (2017). Bio-inspired annelid robot: a dielectric elastomer actuated soft robot. *Bioinspiration & biomimetics*, *12*(2), 025003.

[77] Kim, B., Park, S., Jee, C. Y., & Yoon, S. J. (2005, August). An earthworm-like locomotive mechanism for capsule endoscopes. In *2005 IEEE/RSJ international conference on intelligent robots and systems* (pp. 2997-3002). IEEE.

[78] Li, C., Min, R., Lu, C., & Li, C. (2019). Design and verification of a micro piezoelectric motor with energy harvesting characteristic for capsule endoscope. *Journal of Mechanical Science and Technology*, *33*(10), 4577-4582.

[79] Ciuti, G., Caliò, R., Camboni, D., Neri, L., Bianchi, F., Arezzo, A., ... & Dario, P. (2016). Frontiers of robotic endoscopic capsules: a review. *Journal of micro-bio robotics*, *11*(1), 1-18.

[80] Bianchi, F., Masaracchia, A., Shojaei Barjuei, E., Menciassi, A., Arezzo, A., Koulaouzidis, A., ... & Ciuti, G. (2019). Localization strategies for robotic endoscopic capsules: a review. *Expert review of medical devices*, *16*(5), 381-403.

[81] Liu, L., Towfighian, S., & Hila, A. (2015). A review of locomotion systems for capsule endoscopy. *IEEE reviews in biomedical engineering*, *8*, 138-151.

[82] Cao, Q., Deng, R., Pan, Y., Liu, R., Chen, Y., Gong, G., ... & Han, D. (2024). Robotic wireless capsule endoscopy: recent advances and upcoming technologies. *Nature Communications*, *15*(1), 4597.

[83] Ebrahimi, N., Bi, C., Cappelleri, D. J., Ciuti, G., Conn, A. T., Faivre, D., ... & Jafari, A. (2021). Magnetic actuation methods in bio/soft robotics. *Advanced Functional Materials*, *31*(11), 2005137.

[84] Leon-Rodriguez, H., Lee, C., Ko, S. Y., Park, J. O., & Park, S. (2014, August). Conceptual design of micro-hydraulics system for active and biopsy capsule endoscope robot. In *5th IEEE RAS/EMBS International Conference on Biomedical Robotics and Biomechatronics* (pp. 1068-1072). IEEE.

[85] Lee, C., Choi, H., Go, G., Jeong, S., Ko, S. Y., Park, J. O., & Park, S. (2014). Active locomotive intestinal capsule endoscope (ALICE) system: A prospective feasibility study. *IEEE/ASME Transactions on Mechatronics*, *20*(5), 2067-2074.

[86] Wang, K., Yan, G., Jiang, P., & Ye, D. (2008). A wireless robotic endoscope for gastrointestine. *IEEE Transactions on Robotics*, *24*(1), 206-210.

[87] Verra, M., Firrincieli, A., Chiurazzi, M., Mariani, A., Lo Secco, G., Forcignanò, E., ... & Arezzo, A. (2020). Robotic-assisted colonoscopy platform with a magnetically-actuated soft-tethered capsule. *Cancers*, *12*(9), 2485.

[88] Al Harthy, S., Sadati, S. H., Girerd, C., Kim, S., Mondini, A., Wu, Z., ... & Bergeles, C. (2025). Tip-growing robots: Design, theory, application. *IEEE Transactions on Robotics*.

[89] Greer, J. D., Blumenschein, L. H., Okamura, A. M., & Hawkes, E. W. (2018, May). Obstacle-aided navigation of a soft growing robot. In *2018 IEEE International Conference on Robotics and Automation (ICRA)* (pp. 4165-4172). IEEE.

[90] Wu, R., & Mintchev, S. (2024, October). Vine robots that evert through bending. In *2024 IEEE/RSJ International Conference on Intelligent Robots and Systems (IROS)* (pp. 10535-10542). IEEE.

[91] Hawkes, E. W., Blumenschein, L. H., Greer, J. D., & Okamura, A. M. (2017). A soft robot that navigates its environment through growth. *Science Robotics*, *2*(8), eaan3028.

[92] Blumenschein, L. H., Gan, L. T., Fan, J. A., Okamura, A. M., & Hawkes, E. W. (2018). A tip-extending soft robot enables reconfigurable and deployable antennas. *IEEE Robotics and Automation Letters*, *3*(2), 949-956.

[93] Dinkel, J., Weinmann, D., Pott, P. P., & Schäfer, M. B. (2024, December). Pressure modulation improves locomotion of an expanding robot for colonoscopy. In *Current Directions in Biomedical Engineering* (Vol. 10, No. 4, pp. 187-190). De Gruyter.

[94] Del Dottore, E., Mondini, A., Rowe, N., & Mazzolai, B. (2024). A growing soft robot with climbing plant–inspired adaptive behaviors for navigation in unstructured environments. *Science Robotics*, *9*(86), eadi5908.

[95] Quirini, M., Menciassi, A., Scapellato, S., Stefanini, C., & Dario, P. (2008). Design and fabrication of a motor legged capsule for the active exploration of the gastrointestinal tract. *IEEE/ASME transactions on mechatronics*, *13*(2), 169-179.

[96] Marechal, L., Balland, P., Lindenroth, L., Petrou, F., Kontovounisios, C., & Bello, F. (2021). Toward a common framework and database of materials for soft robotics. *Soft robotics*, *8*(3), 284-297.

[97] Suresha, B. (2010). Friction and dry slide wear of short glass fiber reinforced thermoplastic polyurethane composites. *Journal of reinforced plastics and composites*, *29*(7), 1055-1061.

[98] Roh, S. G., & Choi, H. R. (2005). Differential-drive in-pipe robot for moving inside urban gas pipelines. *IEEE transactions on robotics*, *21*(1), 1-17.

[99] Oya, T., & Okada, T. (2005). Development of a steerable, wheel-type, in-pipe robot and its path planning. *Advanced Robotics*, *19*(6), 635-650.

[100] Elankavi, R. S., Dinakaran, D., Chetty, R. K., Ramya, M. M., & Samuel, D. H. (2022). A review on wheeled type in-pipe inspection robot. *International journal of mechanical engineering and robotics research*, *11*(10), 745-754.

[101] Giri, A., Girerd, C., Cervera-Torralba, J., Tolley, M. T., & Morimoto, T. K. (2025). InchIGRAB: An inchworm-inspired guided retraction and bending device for vine robots during colonoscopy. *IEEE/ASME Transactions on Mechatronics*. Verra, M.